Characterization of a Hyaluronidase 1 (*Hyal1*) null mouse and the examination of the role of Hyal1 in tissue hyaluronan turnover.

By:

Dianna C. Martin

A thesis submitted to the Faculty of Graduate Studies in conformity with the requirements for the Degree of

DOCTOR OF PHILOSOPHY

Department of Biochemistry and Medical Genetics

Faculty of Medicine

University of Manitoba

Winnipeg, Manitoba

Canada

THE UNIVERSITY OF MANITOBA

FACULTY OF GRADUATE STUDIES

*****

COPYRIGHT PERMISSION

Characterization of a Hyaluronidase 1 (Hyal1) null mouse and the examination of the role of Hyal1 in tissue hyaluronan turnover.

BY

Dianna C. Martin

A Thesis/Practicum submitted to the Faculty of Graduate Studies of The University of Manitoba in partial fulfillment of the requirement of the degree

Of

Doctor of Philosophy

Thesis abstract

Mucopolysaccharidoses are a group of clinically heterogenous disorders caused by a deficiency of a lysosomal enzyme essential for glycosaminoglycan degradation. As a result, lysosomal accumulation of substrates ultimately leads to cellular disruption and/or death. The newest mucopolysaccharidosis (MPS) disorder, MPS IX, is a mild lysosomal storage disease characterized by joint abnormalities, periarticular masses, elevated serum hyaluronan (HA) and HA storage in the skin. MPS IX is caused by a deficiency of Hyaluronidase 1 (HYAL1), an enzyme that degrades HA, a component of the extracellular matrix of vertebrate cells. Six hyaluronidase-like genes exist in humans, however their contribution to HA degradation is unknown. To understand the role of Hyal1 in HA turnover, this thesis describes the characterization of a mouse model of MPS IX and the investigation of potential compensatory genes.

To generate a mouse model of deficiency, two *Hyal1* constructs were generated for gene targeting. A *Hyal1* +/- embryonic stem cell line was identified, but the resulting chimeric mice showed a restriction of the thoracic cavity resulting death prior to germline transmission. However, a *Hyal1* +/- mouse line was obtained from the Mutant Mouse Resource Centre. The targeted allele in this mouse line contained an insertion of a neomycin resistance cassette that deleted 753 bp of coding sequence resulting in no detectable wild-type *Hyal1* RNA, protein or serum hyaluronidase activity. *Hyal1* -/- mice were viable, fertile and displayed no gross phenotypic abnormalities. A loss of articular cartilage proteoglycans was found in -/-

mice at 3 months that progressed with age. This proteoglycan loss was accompanied by an increased number of epiphyseal and articular chondrocytes with intense pericellular and/or cytoplasmic HA staining. No detectable elevations of serum HA, tissue GAG or skin HA in -/- mice was found. To identify potential compensatory genes, the hyaluronidase and exoglycosidase expression in -/- mice was examined. An elevation of *Hyal3* was identified in MPS IX mice; however an elevation of *HYAL2* and *HYAL3* was identified in human MPS IX fibroblasts. This suggests that HYAL2 and HYAL3 may partially compensate for loss of HYAL1 function in MPS IX.

Dedication

This thesis is dedicated to the strong female influences who have greatly impacted the course of my life,

my mother and two grandmothers.

These amazing women have taught me to never give up on my dreams, to not be limited by what other people believe and to make the most out of what I was given.

I use these lessons daily.

Acknowledgements

First and foremost, I would like to thank all of the collaborators who have contributed to these studies including Dr John Mort, Dr Judith Farley, Dr Sharon Byers, Dr Jim Thilveris, Dr Anna Plaas, Dr Robert Stern and Dr Sabine Hombach-Klonisch. I would also like to extend my deepest appreciation to Dr Geoff Hicks and Dr Andras Nagy for opening their labs to me during my training and all the members of the departments of Biochemistry and Medical Genetics, Physiology and Anatomy who have greatly supported and encouraged me. I also thank all of the people with transgenic or mouse expertise that have taken me under their wing, Nichola Wigle, Xiaoli Wu, Marina Gertsenstein, Ludger Klewes, Yanglong Mou and Paul Peramul.

I am grateful to all of the lab members, both past and present, which have helped me during my training including Tim Salo, Tamara Shuttleworth, Vasantha Atmuri and Rick Hemming. I would also like to thank Rick for the interesting discussions about science and science methodologies. In a small research environment, this has kept replenishing my enthusiam for science and for that I owe you my deepest gratitude. I would also like to thank to my closest family and friends, Heather, Nehal, my mom and dad, who have kept encouraging and supporting me during my graduate work. I wouldn't have accomplished what I have without them.

Last, but certainly not least, I would like to thank my supervisor. Words cannot express my appreciation for all of the moments when she has stepped in to provide me with more than just training, but encouragement as a friend and guidance as a teacher. I am eternally grateful to her for always raising the levels of expectations

during my training, which has continuously developed and challenged me. In addition to the support and guidance she has given me, she has always allowed me ample opportunities to develop techniques, skills or ideas that I felt would be most beneficial. During my training, she has taught me not to compromise the quality of data that I generate and has shown me to go after the most important questions in the field. Due to the example she has set for me as a scientist and teacher, I only hope that one day I can provide the same characteristics to students of my own.

Table of contents:

Preface:

List of tables

List of figures

List of abbreviations

©	copyright
®	registered trademark
γ	gamma
°C	degrees Celsius
bp	base pair
g	relative centrifugal force
hr	hour
kb	kilobases
kDa	kilodaltons
kV	kilovolts
M	molar
mA	milliamps
mg	milligram
ml	milliliter
min	minutes
mM	millimolar
nm	nanometers
s	seconds
V	volts
µF	microfarad
µg	microgram
µl	microliter
β-geo	LacZ-Neo cassette
BPTE	bis-tris PIPES EDTA
CD44	cluster of differentiation 44
CIP	Calf alkaline intestinal phosphatase
CPC	hexadeceylpyridinium chloride
DMEM	Dulbecco's modified eagle medium
DMSO	dimethylsulfoxide
DNA	deoxyribonucleic acid
dNTP	2'- deoxyribonucleotide 5'triphosphate
DTA	diphtheria toxin A
DTT	dithiothreitol
DWE	aspartate tryptophan glutamate
ECM	extracellular matrix
EDTA	ethylenediamine tetraacetic acid
EGF	epidermal growth factor
ER	endoplasmic reticulum
ES	embryonic stem
FACE	fluorescence assisted carbohydrate electrophoresis
FBS	fetal bovine serum
GAG	glycosaminoglycan
GFP	green fluorescent protein

GlcNAc	N-acetyl-glucosamine
Glu	D-glucuronic acid
GPI	Glycosylphospatidylinositol
GPI-HYAL2	GPI-anchored HYAL2
GTE	Glucose Tris EDTA
HA	hyaluronan
HABP	hyaluronic acid binding protein
HARE	hyaluronan receptor for endocytosis
HAS	hyaluronan synthase
HAS1	hyaluronan synthase 1
HAS2	hyaluronan synthase 2
HAS3	hyaluronan synthase 3
HEX	β-hexosaminidase
HMW	high molecular weight
HR	homologous recombinant
HRP	horse radish peroxidase
HYAL1	hyaluronidase 1
HYAL2	hyaluronidase 2
HYAL3	hyaluronidase 3
HYAL4	hyaluronidase 4
IαI	inter-α-inhibitor
IRES	internal ribosome entry site
LB	luria broth
LacZ	β-D-galactosidase
LIF	leukaemia inhibitory factor
LMW	low molecular weight
LYVE-1	Lymphatic Vessel Endothelial Receptor-1
MEF	mouse embryonic fibroblasts
MGEA5	meningioma expressed antigen 5
MOPS	3-(N-morpholino) propane sulfonic acid
MPS	mucopolysaccharidosis
MRI	magnetic resonance imaging
Neo	neomycin resistance cassette
NLS	nuclear localization signal
ODB	Qiagen proprietary buffer
OL1	Qiagen proprietary cell lysis buffer
OMIM	online mendelian inheritance of man
OW1	Qiagen proprietary wash solution
OW2	Qiagen proprietary wash solution
P1	Qiagen proprietary bacterial resuspension buffer
P2	Qiagen proprietary bacterial lysis solution
P3	Qiagen proprietary neutralization solution
pαI	pre-α-inhibitor
PAC	P1 artificial chromosome
PAGE	polyacrylamide gel electrophoresis
pBS	Bluescript SK^+ plasmid

PBS	phosphate buffered saline
PCR	polymerase chain reaction
PGK	phosphoglycerate kinase promoter
PIPES	2-[4-(2-sulfoethyl) piperazin-1-yl]ethanesulfonic acid
PTX3	pentaxin 3
QBT	Qiagen proprietary column equilibration buffer
QC	Qiagen proprietary wash buffer
QF	Qiagen proprietary elution buffer
RNA	ribonucleic acid
RT-PCR	reverse transcription PCR
SA	splice acceptor
SD	standard deviation
SDS	sodium dodecyl sulfate
SDS-PAGE	polyacrylamide gel electrophoresis containing SDS
SEM	standard error mean
SOC	super optimal catabolite repressor medium
SSC	standard saline citrate
TAE	tris acetate EDTA
TBE	tris borate EDTA
TBST	tris buffered saline with Tween-20
TEMED	tetramethylethylenediamine
TK	thymidine kinase
Tris	2-amino-2-hydroxymethyl-1,3-propanediol
TSG-6	tumor necrosis factor stimulated gene-6
UDP	uridine diphosphate
WT	wild-type

Chapter 1: Introduction

1.1 Lysosomal storage disorders

1.1.1 Definition, history and perspective

Lysosomal storage disorders are a group of clinically heterogenous metabolic disorders caused by lysosomal enzyme deficiencies[1]. Numerous nucleases, lipases, glycosidases and proteases are all held within the lysosomal compartment of the cell and a partial or complete deficiency of any one of these enzymes can result in the development of a lysosomal storage disorder. Most of these diseases, with the exception of Hunter, Danon and Fabry disease, are inherited in an autosomal recessive fashion [2]. However, a deficiency of a lysosomal enzyme is not the only mechanism to generate a lysosomal storage disorder. Transferases, metabolite transporters and proteins involved in the targeting, modification or stabilization of lyosomal enzymes can interrupt degradative pathways resulting in disease[3]. In all lysosomal storage disorders, the resulting presenting pathology is due to the progressive nature of the cellular substrate accumulation that ultimately leads to cellular dysfunction and/or death.

Historically, the biochemical, molecular and pathological basis associated with a lysosomal storage disorder has been uncovered very slowly. The first known disorders, Tay-Sachs and Gaucher disease, were described clinically in the 1880's[3]. However, typical of lysosomal storage disorders, it was not until much later that the nature of the accumulating substrate and the specific enzyme deficiency was identified. In Gaucher disease for example, the accumulating

substrate, glucosylceramide, was not identified until the 1930's and the enzymatic deficiency of glucocerebrosidase was not determined until nearly 30 years later[3-5]. A major advance in lysosomal storage disorder research occurred when DeDuve and colleagues isolated the lysosomal compartment of the cell using sub-cellular fractionation[6]. This discovery resulted in the ability to link a specific lysosomal enzyme deficiency with the resulting intracellular substrate accumulation that leads to pathological changes involved in disease progression. Since then, molecular techniques have been used extensively to determine gene mutations associated with disease, as well as the resulting effects on protein structure and function.

Today, there are over 50 known lysosomal storage disorders and the genetic basis for most of these diseases has been determined[1]. Genomic mutational analyses have been used to identify common disease causing mutations and to characterize the prevalence of these mutations within at-risk communities. However, despite considerable knowledge regarding the causes of lysosomal storage disorders, the molecular and pathological mechanisms that ultimately lead to cellular dysfunction and death remain to be elucidated. This makes the continued use of cell systems and animal models of disease of increasing importance to study pathological alterations caused by accumulation.

1.1.2 Clinical heterogeneity

Lysosomal storage disorders are a clinically heterogenous group of genetic diseases that can be loosely categorized based on the type of accumulating

substrates. Several categories have been defined including lipidoses, sphingolipidoses, mucopolysaccharidoses, oligosachharidoses, glycoproteinoses and others[1]. However, this is a loose classification system as a deficiency of an enzyme often leads to the accumulation of more than one type of substrate. For example, β-galactosidase degrades G_{M1} gangliosides, glycosaminoglycans, and oligosaccharides[7]. The cellular accumulation that occurs in lysosomal storage disorders gives rise to clinical symptoms that increase in severity with age. However the rate of progression can vary and is often inversely correlated with the level of residual enzymatic activity[8]. Each lysosomal storage disorder usually displays a broad spectrum of disease symptoms, making it difficult for a non-specialized clinician to diagnose and classify the metabolic deficiency. This spectrum of symptoms can arise due to differing levels of enzyme activity, mutations that affect the degradation of only one type of substrate, individual metabolic variation and differences in downstream pathogenic pathways caused by substrate accumulation[3].

1.2 Mucopolysaccharidoses

1.2.1 Definition, clinical characteristics and pathological features

Mucopolysaccharidoses (MPS) are lysosomal storage disorders caused by a deficiency of a lysosomal enzyme essential in the degradation of glycosaminoglycans (GAGs)[9]. These disorders were originally coined as mucopolysaccharidoses due to the mucus-like structure of the accumulating GAG substrates[9]. No studies on the prevalence of these disorders has been performed in

North America, however a retrospective study in Australia estimates that these diseases are found at a birth prevalence of 1: 22,500 and represents approximately 1/3rd of all lysosomal storage disorders [10]. There are 7 known MPS disorders, outlined in Table 1, that are classified by their enzymatic deficiency[9]. With the exception of MPS II (Hunter disease) that is inherited in a X-linked manner, these disorders display an autosomal recessive mode of inheritance[11, 12]. Currently, there are 13 enzymes known to function in GAG degradation and theoretically a deficiency of any of these enzymes could result in an MPS disorder. However of these 13 enzymes, only 11 have been identified to result in an MPS disorder[9]. With the exception of MPS IIIC that is caused by an acetyl transferase deficiency essential in heparan sulfate degradation, all of these disorders are caused by a deficiency of a hydrolase that cleaves glycosidic bonds[9, 13].

Table 1: Clinical symptoms and overview of mucopolysaccharidoses.

MPS* Disorder	Gene Symbol	Clinical Symptoms	Enzyme	Accumulating GAGs
MPS I				
H (Hurler)	IDUA	Corneal clouding, dystosis multiplex, organomegaly, enlarged tongue, coarse facial features, hearing loss, short stature, heart disease, mental retardation, death in childhood.		dermatan sulfate and heparan sulfate
S (Scheie)	IDUA	Corneal clouding, stiff joints, aortic valve disease, coarse facial features.	α-L-iduronidase	
H/S (Hurler/ Scheie)	IDUA	Severity between MPS I H and MPS I S.		

MPS II (Hunter)	IDS	Dystosis multiplex, coarse facial features, short stature, deafness, organomegaly, mental retardation, death by 15 years. Milder forms display normal intelligence and patients can survive to adulthood.	iduronate sulfatase	dermatan sulfate and heparan sulfate
MPS III (Sanfilippo)				
A	MPS3A	Mental deterioration, hyperactivity, mild hepatosplenomegaly, deafness.	Heparan N-sulfatase	heparan sulfate
B	NAGLU		α-N-acetyl-glucosaminidase	
C	HGSNAT		Acetyl-CoA:α-glucosaminide acetyltransferase	
D	GNS		N-Acetyl-glucosamine-6-sulfatase	
MPS IV (Morquio)				
A	GALNS	Skeletal abnormalities, short stature, corneal clouding, odontoid hypoplasia, hepatomegaly, hearing loss.	N-acetylgalactosamine 6-sulfatase	keratan sulfate
B	GLB1		β-galactosidase	keratan sulfate and chondroitin 6-sulfate
MPS VI (Maroteaux-Lamy)	ARSB	Dystosis multiplex, corneal clouding, survival to teens in more severe forms.	N-acetylgalactosamine 4- sulfatase (arylsulfatase B)	dermatan sulfate
MPS VII (Sly)	GUSB	Dystosis multiplex, hepatosplenomegaly, dysmorphic features, mental retardation, early onset	β-glucuronidase	dermatan sulfate, heparan sulfate, chondroitin 4/6 sulfates
MPS IX	HYAL1	Periarticular soft masses, mild short stature	hyaluronidase 1	hyaluronan

* MPS V and MPS VIII are no longer used to classify disorders; § Modified from[9]. Permission to modify this table was obtained from The McGraw-Hill Companies. Further reproduction of this material is strictly forbidden.

Typical of lysosomal storage disorders, MPS disorders display a spectrum of clinical symptoms and severities of disease. As a result, patients may display severe symptoms leading to death at early ages or attenuated symptoms where patients can lead a relatively normal lifespan (for in-depth review[9]). MPS patients typically present with skeletal dysplasias, developmental delays and/or cranio-facial dysmorphology at the time of diagnosis. Somatic tissue involvement is also a common occurrence and can result in organomegaly. Mental impairment is caused by central nervous system GAG or ganglioside accumulation and has been described in MPS I, MPS II, MPS III, MPS IV and MPS VII[9]. In addition, due to the high GAG concentrations in the eye, corneal clouding is seen in MPS I, MPS IV, MPS VI and occasionally in MPS VII patients[9]. Common problems occurring in MPS disorders include chronic ear, nose and throat infections, hearing and vision loss, respiratory infections, airway obstruction, loss of joint function, cardiomyopathy and atrial or mitral valve deposits[14]. Patients that display symptoms on the severe side of the spectrum typically die due to respiratory or heart complications caused by cardiomyopathy, valve deposits, respiratory infections and/or airway obstructions[14]. The treatment of MPS patients has been focused mainly on alleviating symptoms to improve the patient's quality of life, but recently developed enzyme replacement therapies for MPS I (laronidase), MPS II (idursulfase) and MPS VI (galsulfase) can alleviate some of the symptoms displayed in these disorders[15-17].

The underlying MPS pathology is due to the cellular GAG accumulation identifiable histologically as cells displaying a foamy or ballooned appearance. Urine excretion of accumulating non-degraded or partially degraded saccharides is found in all known MPS disorders, except MPS IX, and identification of these structures may assist in the diagnosis and classification of a disorder[9, 18, 19]. Multiple GAGs may accumulate in a specific MPS disorder due to the overlapping function of the deficient enzyme in more than one degradative pathway. This is seen in dermatan and heparan sulfate degradation, where α-L-iduronidase, iduronate sulfatase and β-glucuronidase function in the degradation of both GAGs[9].

1.2.2 GAG structures, distribution and synthesis

GAGs are polysaccharides that consist of repeating disaccharide units containing either galactosamine or glucosamine sugars and glucuronic or iduronic acid[20]. The sole exception is keratan sulfate that is composed of two sugars, galactose and glucosamine[21]. There are several known GAGs that are found in the extracellular matrix (ECM) of cells including heparan sulfate, keratan sulfate, dermatan sulfate, hyaluronan and chondroitin sulfate[20]. With the exception of hyaluronan, GAGs are sulfated and can be classified based on their sulfation patterns. As an example, chondroitin sulfate has 4 sub-classes designated A, C, D and E based on the sulfation of the N-acetyl-galactosamine (C4 and/or C6) and uronic acid (C2) saccharides[22].

Most GAGs are synthesized as proteoglycans within the endoplasmic reticulum and golgi apparatus of the cell and follow the secretory pathway to the extracellular environment (Table 2) [21, 23]. Proteoglycans and/or GAGs make up the saccharide component in the ECM and can vary in their composition within the ECM of different cells and tissues. The 3 dimensional structures of the ECM can be determined by the proteoglycan composition and sulfation patterns and various GAG binding proteins (Table 2). GAG degradation occurs in the lysosome of a cell, although a large proportion of the GAG degradative process including receptors and uptake mechanisms remain unknown[18].

Table 2: GAG disaccharide composition, properties and synthesis.

GAG	Disaccharide components	Sulfation	Synthesis Location
chondroitin or chondroitin sulfate	N-acetylgalactosamine	sulfated or non- sulfated	endoplasmic reticulum and golgi
	glucuronic acid		
hyaluronan	N-acetyl-D-glucosamine	non-sulfated	cell membrane
	D-glucuronic acid	non-sulfated	
dermatan sulfate	N-acetylgalactosamine	sulfated	endoplasmic reticulum and golgi
	predominantly iduronic acid, also glucuronic acid	sulfated	
heparan sulfate	N-acetylglucosamine	sulfated	endoplasmic reticulum and golgi
	iduronic acid or glucuronic acid	N-acetylated or sulfated	
keratan sulfate	Galactose	sulfated	endoplasmic reticulum and golgi
	N-acetylglucosamine	sulfated	

1.2.3 Mucopolysaccharidosis IX (MPS IX)

The newest MPS disorder, MPS IX, was identified in 1996 and has only one clinically described patient to date[19]. This is a relatively subtle MPS disorder, where the main symptoms affect peripheral tissues and include periarticular masses, mild short stature, a sub-mucosal cleft palate and multiple joint abnormalities. Radiographic analysis of the patient displayed erosions of the acetubula, a nodular synovium and a popliteal cyst. Serum hyaluronan (hyaluronic acid; HA) levels in this patient were elevated 36- to 84-fold compared to normal circulating HA concentrations (25-75 ng/ml). Examination of biopsied periarticular masses by electron microscopy revealed a lysosomal accumulation of flocculent material in skin macrophages and fibroblasts. These vacuoles bound Alcian Blue, suggesting an accumulation of a GAG component. The intensity of the Alcian Blue staining decreased upon pre-treatment of sections with hyaluronidase identifying the accumulating GAG substrate as HA.

In 1999, this disease was determined to be caused by mutations in a hyaluronidase gene, *HYAL1,* inherited in an autosomal recessive manner[24]. The patient is a compound heterozygote that contained a transversion point mutation and a complex insertion/deletion mutation. The c.1412G>A point mutation found in one allele, results in a Lys268Glu amino acid change that has been previously shown in testicular hyaluronidase (PH-20) to result in no detectable hyaluronidase activity[25]. The second mutation identified is a complex c.1361_1398del37ins14

mutation that results in a frameshift of the coding sequence causing premature termination at amino acid 269. The patient contains no detectable serum hyaluronidase activity as a result of these mutations. No additional mutations were detected in hyaluronidase family members, *HYAL2* or *HYAL3,* suggesting a deficiency of multiple hyaluronidases is not required to cause disease.

1.3 Hyaluronan

1.3.1 Saccharide composition and structure

Nearly 20 years after the initial isolation of HA in 1934 by Karl Meyer, the chemical structure of the molecule was identified to contain repeating disaccharide units of (β1-4) D-glucuronic acid (β1-3) N-acetyl-D-glucosamine (Figure 1A) [26, 27]. The size of the polymer typically ranges from 10^5- 10^7 Da depending on its origin[20]. HA is unique among GAGs, since it is not bound to a proteoglycan core protein, is unbranched and non-sulfated. HA exists in a free form or organized into the ECM structure. The chemical composition of HA allows the formation of hydrophobic and hydrophilic faces along the large molecule (Figure 1B). In solution, the axial hydrogen atoms of the saccharides form hydrophobic faces, while the equatorial carboxyl and acetyl side chains form a hydrophilic faces[28]. This results in a secondary structure that resembles a ribbon structure due to the conformational twisting caused by an interaction between the hydrophobic faces. As a result of this structure, HA in solution forms a random coil that expands to fill an enormous volume and gives HA its space filling property that functions as a lubricant in the synovial fluid of the joint[20]. The

A)

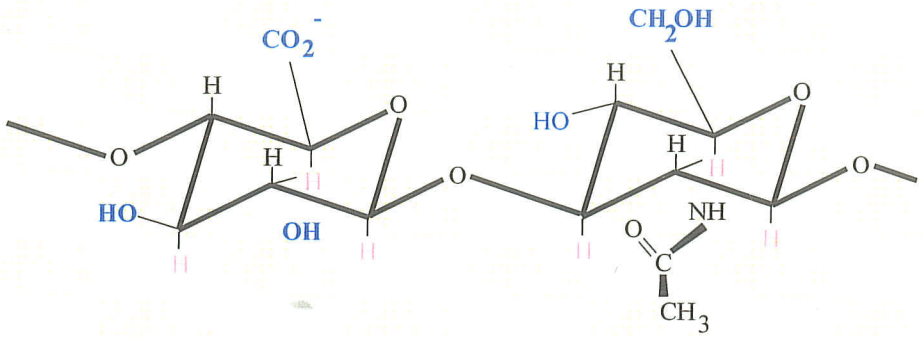

β-D-glucuronic acid (Glu)

β-N-acetyl-D-glucosamine (GlcNAc)

B)

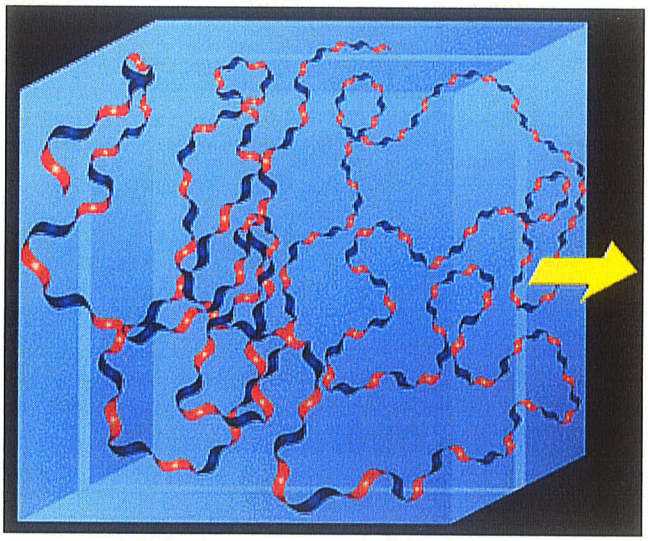

Figure 1: Disaccharide and polymeric structure of HA.
A schematic of the disaccharide structure of that extends to form large HA polymers is shown in A). In B), the hydrophobic faces (dark blue) and hydrophilic faces (red) of the polymer form a ribbon structure due to the interaction between hydrophobic faces. In solution, HA assumes a random coil structure and expands to fill the volume of the containing vessel, which is displayed in B) by the blue box. Permission to reproduce panel B was obtained from the Seigagaku Corporation, who maintain the Glycoforum web site (Glycoforum, www.glycoforum.gr.jp), on March 7, 2008. The original figure can be found at http://www.glycoforum.gr.jp/science/hyaluronan/HA01/HA01E.html. Resale or further copying of this material is strictly prohibited.

carboxyl groups of the glucuronic acid are charged at an extracellular pH, therefore attracting large volumes of water. This provides a cellular barrier of hydration that is proposed to function as a mechanism to evade immune surveillance[20].

1.3.2 Distribution and function

HA is a ubiquitously expressed macromolecule found in the ECM of all vertebrate cells [20]. The highest concentrations of HA are found in loose connective

tissues such as the vitreous humor of the eye (140-338 μg/g), the synovial fluid of joint (1400-3600 μg/g) and the Wharton's Jelly of the umbilical cord (4100 μg/g) [20]. Examination of HA distribution in the rat system shows that the majority of total body HA is found in the skin (50 %) and skeletal structures (25 %)[29].

HA binds to ECM proteins and/or cell surface receptors termed hyaladherins. Several hyaladherins are known including aggrecan, neurocan, brevican, inter-α-inhibitor (IαI) and versican. Most of these contain a Link module (proteoglycan tandem repeat) that is involved in HA binding[30]. The hyaladherins, with GAGs, form large macromolecular complexes in the ECM that can retain HA in the ECM of cells (Figure 2). This structure when enclosed by collagen fibers in the cartilage provides a tensile hydrated structure that can resist large weight bearing loads[30]. Some hyaladherins, such as IαI, contain no link module, but can be covalently linked to HA via an ester bond with the hydroxyl group of N-acetylglucosamine[31, 32]. HA is essential to the ECM formation, since digestion with hyaluronidase

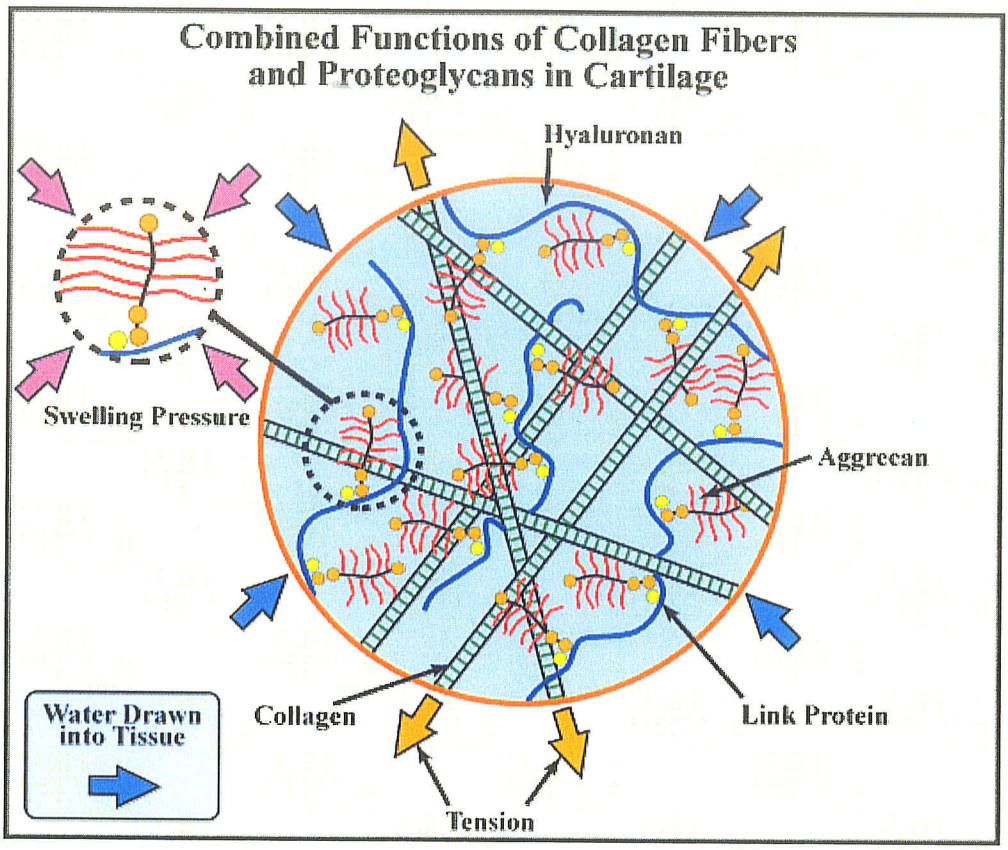

Figure 2: HA in the extracellular matrix structure of cartilage.
Permission to reproduce this figure was obtained from the Seigagaku Corporation, who maintain the Glycoforum web site (Glycoforum, www.glycoforum.gr.jp). The original figure can be found at
http://www.glycoforum.gr.jp/science/hyaluronan/HA05/HA05E.html. Resale or further copying of this material is strictly prohibited.

results in the loss of the pericellular coat that is re-formed by exogenous HA and one of the hyaladherins versican[33].

HA and hyaladherin interactions can provide complicated structures due to interactions between hyaladherin molecules. This is evident in the cumulus oocyte complex where IαI, tumor necrosis factor stimulated gene-6 (TSG-6) and pentraxin 3 (PTX3) bind each other and/or HA to generate a largely expanded structure surrounding the developing oocyte[34]. Furthermore, IαI and pre-α-inhibitor (pαI) are crucial components of a cable-like HA that leukocytes adhere to during chronic inflammatory conditions[35, 36].

1.3.3 Synthesis

Unlike other GAGs that are made in the ER and Golgi apparatus, HA is synthesized using uridine diphosphate (UDP) linked precursors on the cytosolic surface of the plasma membrane through the action of hyaluronan synthases ([37]; for review of synthases[38]). There are two classes of synthases that are divided based on the ability to extend the reducing or non-reducing termini of HA. The majority of HA synthases, including the human synthase genes, fall into Class 1. In this class of enzyme, both the UDP-glucuronic acid and UDP- N-acetyl-glucosamine are added to the reducing termini and are suggested to contain only one active site that catalyzes the addition of the saccharide units[39]. The only known class 2 synthase to date is in *Pasteurella multicoda*, which catalyzes saccharide addition at the non-reducing end of HA using two separate active sites[40, 41].

There are three known mammalian hyaluronan synthase (HAS) isoforms, HAS1, HAS2 and HAS3[42]. These genes display ~ 50% similarity to each other, yet appear to have distinct synthetic properties. *In vitro* overexpression has demonstrated that HAS3 produces HA of lower molecular weight (10^5 to 10^6 Da) than either HAS1 or HAS2 (2×10^5 to 2×10^6)[43]. This has been supported *in vivo* by the absence of low molecular weight (LMW) HA in ventilator induced lung injury in HAS3 deficient mice[44]. The most important hyaluronan synthase appears to be HAS2 since a mouse model of deficiency results in embryonic lethality due to abnormally low HA levels ($\leq 3\%$ normal) that impair cardiac morphogenesis[45]. In contrast, HAS3 null mice display a normal appearance, life span and fertility[44]. The only known defect is a reduced ability to induce inflammation, due to a lack of LMW HA species, in a model of lung injury[44]. HAS1 null mice have not yet been published, but have been reported to be viable and fertile, along with mice deficient in both HAS1 and HAS3[45, 46].

Currently, the mechanism of HA exocytosis by membrane transport has created controversy. The HAS enzymes contain 7 transmembrane domains that span the plasma membrane and are suggested to form a pore-like structure assumed to be involved in HA export[47, 48]. Recently, an alternative mechanism for HA exocytosis has been uncovered in bacterial and mammalian cells, active transport through an ABC class of membrane transporters[49, 50]. These export proteins were first uncovered in *Streptococcus pyogenes*, where it is essential in the formation of a virulent HA capsule[49]. However, an ABC transporter (MRP5) has been identified in human fibroblasts and knockdown or inhibition of this

transporter significantly reduces HA exocytosis[51]. This observation has generated debate in the field about the significance of the HAS proteins in extracellular secretion of HA and enthusiasm in uncovering the molecular mechanisms involved between synthesis and export.

1.3.4 Turnover of HA

GAGs, just like other components of the human body, require renewal. Due to the structural functions of HA in different tissues and the more specialized role in embryonic development and wound healing, HA turnover must occur through both constitutive and regulated turnover. The majority of HA turnover occurs through a constitutive mechanism. Estimates of constitutive HA turnover suggest that ~5 g or 1/3 of total body HA, is turned over daily[52]. The rate of HA turnover varies between different tissues with a half-life ranging from approximately 1 hr to 70 days[53]. Tissue HA turnover occurs mainly by cellular uptake and degradation within the lymph nodes, but also has been shown to occur by local degradation[54-56]. HA evading degradation by these mechanisms, enters the circulation where it has a half-life of 2 ½ to 4 ½ min[57]. Between 85 - 90 % of circulating HA is removed in the liver, 10 % is removed in the kidney and only 1 - 2 % is excreted in urine[58, 59].

1.3.5 Cellular HA uptake and receptors for endocytosis

Several receptors including Cluster of Differentiation 44 (CD44), Hyaluronan Receptor for Endocytosis (HARE; also known as Stabilin-2) and Lymphatic Vessel Endothelial Receptor-1 (LYVE-1) that have been described to function in HA endocytosis[60-62]. CD44 is the most constitutively expressed HA receptor, being expressed on most cell types. It was originally believed to be the main receptor involved in HA endocytosis until a CD44 null mouse showed only minor phenotypic defects[63]. CD44 appears to function by a novel endocytic mechanism independent of caveolae and clathrin dependent pathways[64]. This pathway requires the association of CD44 with lipid rafts in the plasma membrane, as the disruption of palmitoylation of cysteine residues prevents this association and inhibits HA internalization[65]. While CD44 is not essential for daily constitutive turnover, it does play an important role in the regulated HA degradation required for the resolution of inflammation[66]. This has also been supported in different models, as CD44 null mice show aggravated reactions to inflammatory processes in models of bone loss and collagen induced arthritis[67, 68].

The two other receptors that function in HA endocytosis, LYVE-1 and HARE display a more tissue specific expression. LYVE-1 is a transmembrane glycoprotein first identified based on its homology to CD44 and contains a single Link module common to hyaladherins[60]. LYVE-1 expression is found only in lymphatic endothelium, while HARE is expressed in sinusoidal endothelial cells in the liver as well as within medullary sinuses of the spleen and lymph node[60, 62]. An LYVE-1 deficient mouse model has been generated that appears to have a normal phenotype, although controversy exists about the phenotypic effects on

the morphology of lymphatic vessels and interstitial lymphatic flow[69, 70]. Additionally, LYVE-1 null mice have normal HA serum and tissue HA content[69]. It has recently been suggested that the function of LYVE-1 in HA endocytosis, originally based on overexpression studies, was incorrect since HA uptake in primary lymphatic endothelial cells does not change upon down-regulation of LYVE-1[60, 71]. Therefore the role of LYVE-1 in HA uptake is currently controversial.

HARE may be the main receptor for HA endocytosis at the present time. The HARE receptor is expressed in liver sinusoids, medullary sinuses of the lymph node and venous sinusoids in the red pulp of the spleen and functions via the clathrin coated pit pathway[62, 72]. HARE exists in two isoforms (315 kDa, 190 kDa) in humans[73]. Both isoforms contain the characteristic Link module of hyaladherins and display similar specificities to various GAGs[73]. HARE has a binding affinity for HA, chondroitin/chondroitin sulfates and to a lesser extent dermatan sulfate, but displays no affinity to heparan sulfate or keratan sulfate. Despite the inability to bind heparan or keratan sulfate, the affinity of HARE for other GAGs, as well as HA, suggests that this receptor may function as a scavenger for GAG endocytosis. A mouse deficient in HARE will be essential in determining its contribution HA uptake, as well as to the uptake of other GAGs.

In addition to the known receptors for endocytosis, HA uptake has also been observed to occur through alternative routes. HA uptake has been found to occur by macropinocystosis and novel mechanisms of uptake in rat epidermal keratinocytes[64]. Additionally, unknown routes and/or receptors of HA uptake

have been described in primary lymphatic endothelial cell lines[71]. Therefore, it is likely that additional mechanisms and receptors for HA uptake may be uncovered in the future.

1.4 Abnormalities in HA turnover

In addition to MPS IX, the only known congenital abnormality in HA turnover was found in a patient that displayed a generalized thickening and folding of the skin (OMIM#604855). Although the epidermis appeared normal in this patient, serum HA was elevated and the dermis of the skin was thickened with a disorganization of the collagen fibers caused by granular material that was identified as HA[74]. Cultured fibroblasts display an increased HA synthase activity, yet the serum hyaluronidase activities are normal suggesting this was due to alterations in synthase activity[74]. Investigators noted that the phenotype and characteristics of this synthesis disorder are very similar to the well known Char-pei dog that displays a wrinkled appearance due to a generalized thickening of the skin and demonstrated that serum HA levels are also elevated in the Char-pei breed when compared to controls[74].

1.5 HA in health and disease

HA has been hypothesized to play a role in the proliferation, migration and differentiation of cells during embryogenesis and/or morphogenesis[20]. The identification of an HA-rich pericellular matrix on many migratory cells involved

in neural tube formation, brain and limb development, and its removal upon differentiation, suggests its importance in the proliferation and migration of these cells during development[75]. Further, the generation of *Has2* null mice has clearly established the role of HA in migration and differentiation during heart development, where endothelial cell migration and mesenchymal transformation are impaired due to extremely low levels of HA[45]. This appears to be mediated by Ras signaling in these cells, as endothelial migration and mesenchymal transformation can be restored by exogenous HA or Ras expression in explant cultures[45, 76].

The role of HA in health and disease is becoming much broader than originally anticipated, as alterations in HA levels have been detected in cancer, CNS lesions, lung injury, renal injury, stroke and vascular disease ([77] and for review[78-81]). In cancer, elevated HA levels have been found in the stroma of tumors in breast carcinoma, ovarian carcinoma, prostate cancer, and non small-cell lung adenocarcinomas, and either correlate with low survival rates or malignancy[82-86]. Elevated parenchymal HA levels have also been identified in gastric and colorectal cancers and correlate with malignancies[87, 88]. Elevated HA levels found in inflammatory lesions, caused by injury to the lung, kidney or liver appear to function in the inflammatory response and/or in tissue remodeling for repair[79, 89-91].

The effects of HA in injury and repair appears to depend on the size of HA and some of the known functions of HA of various sizes is shown in Figure 3.

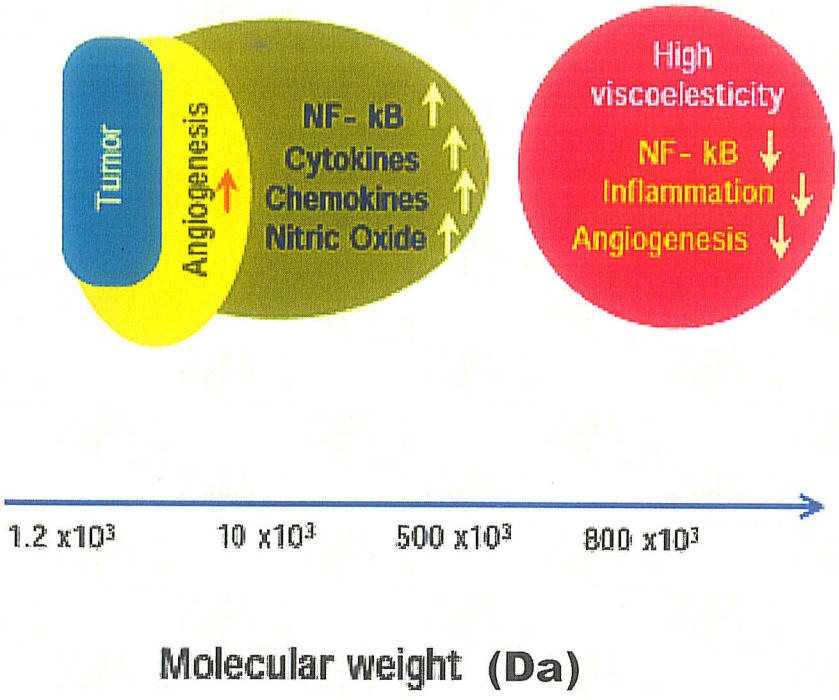

Figure 3: The functions of HA at different sizes.
This figure was modified from the original on-line version found: http://www.glycoforum.gr.jp/science/hyaluronan/HA12a/HA12aE.html. Permission to reproduce this figure was obtained from the Seigagaku Corporation,who maintain the Glycoforum web site (Glycoforum, www.glycoforum.gr.jp). Resale or further copying of this material is strictly prohibited.

LMW HA is important in stimulating inflammation, as CD44 null mice display increased mortality after bleomycin induced lung injury due to impaired clearance of LMW HA that results in persistent inflammation[66]. LMW HA is capable of stimulating angiogenesis and endothelial cell migration necessary during inflammation and its involvement in stimulating inflammatory processes is mediated, at least in part, by signaling via Toll-like receptors that induce the expression of inflammatory chemokines and cytokines[92, 93]. High molecular weight (HMW) HA does not stimulate angiogenesis and has been associated with the formation of scars that can prevent regenerative mechanisms[92, 94]. HMW HA is suggested to inhibit the maturation and migration of regenerative cells required for remyelination and/or nerve formation after spinal cord injury and in models of multiple sclerosis[95].

Yet despite the large body of knowledge indicating that HA functions in inflammation, injury and embryogenesis, we still do not understand how the levels of HA are regulated during normal physiological and pathological disease states. In addition, HA is available in forms for use in many medical applications for example osteoarthritis treatment (Synvisc® HYLAN G-F-20, Genzyme Corporation)[96], cosmetic wrinkle reduction (HYLAFORM®, McGhan Medical)[97], and in cosmetic moisturizers to reduce the effects of aging. However, the turnover mechanisms of HA, as well as its cross-linked forms being used in various medical applications, is still not well understood. Therefore, basic research studying the synthesis and catabolism of HA will greatly advance our knowledge of how the levels and molecular weight of HA are regulated and the

implications for the continued use of cross-linked HA forms in medical applications. This could also guide the development of HA forms to be used for medical and cosmetic purposes.

1.6 HA metabolism

1.6.1 Hyaluronidases

The hyaluronidases were first described in 1930 by Duran-Reynals as the 'spreading factor' that allowed the penetration of vaccines, bacterial toxins and dyes into the skin[98]. These enzymes cleave the β-1,4 linkage between the N-acetylglucosamine and the D-glucuronic acid of HA and are the only known endoglycosidases in GAG degradation. Hyaluronidases are found in numerous organisms ranging from simple bacterial organisms, such as *Streptoccocus pyogenes* to more complex vertebrates including humans.

Humans have six related hyaluronidase-like genes localized in two chromosomal loci, 3p21.3 (*HYAL1*, *HYAL2*, *HYAL3*) and 7q31.3 (*HYAL4*, *SPAM1*, *HYALP1*)[99]. The human hyaluronidase genes contain approximately 40 % amino acid sequence identity to each other. The gene organization, structure and similarity is preserved in the mouse system, where the genes are found on chromosomes 9F1-9F2 and 6A2 respectively (Figure 4A)[100]. In the rodent system, an additional hyaluronidase gene, *Hyal5*, was recently identified downstream of *Spam1*[101]. *Hyal5* has only been identified in the rodent system to date, and has not yet been identified in humans. The evolutionary relationships between the genes are displayed in Figure 4B.

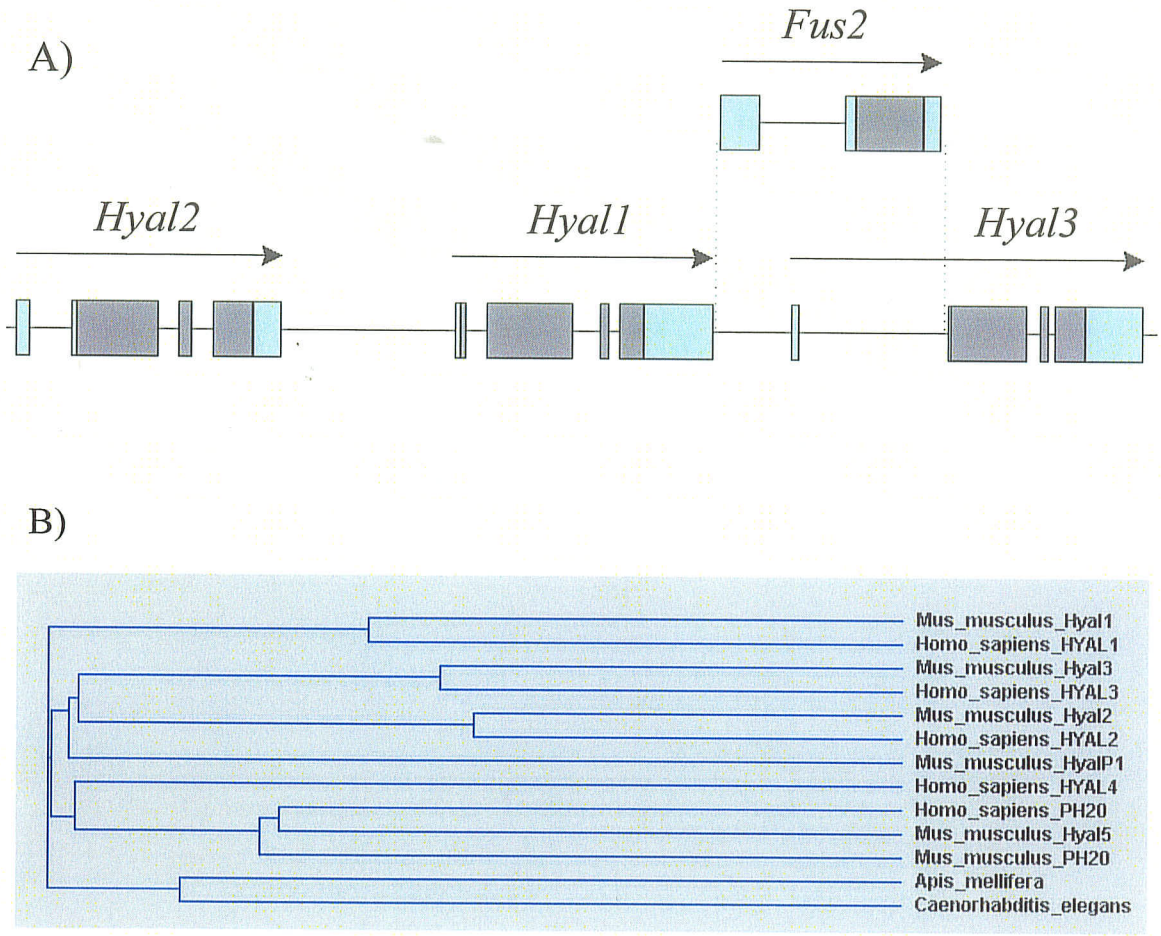

Figure 4: Organization of the mouse *Hyal1*, *Hyal2*, *Hyal3* genes and the evolutionary relationships between the hyaluronidases
In A, a schematic of the mouse gene organization is shown. Exons are displayed as boxes, introns and intergenic regions as lines and the direction of the gene transcription is shown by the arrows. Grey boxes indicate the coding regions of the genes and light blue boxes represent untranslated regions. In B, the evolutionary relationships between the hyaluronidases are shown using a phylogram generated by ClustalW alignment.

1.6.1.1 Hyaluronidase 1

Hyaluronidase 1 (HYAL1), even though it was only purified in 1997, is one of the best characterized hyaluronidases, second only to PH-20 (See section 1.6.1.4). *HYAL1* is expressed highly in tissues important in HA turnover including the liver, kidney and spleen, but has also been detected in most tissues examined including the heart, lung, skin and skeletal muscle (Appendix 1) [99]. HYAL1 was first purified from the blood plasma and displays an acidic pH optimum of 3.8 with little activity at a pH $\geq$ 4.5[102]. Although the subcellular localization of HYAL1 has not been established, it is presumed to be a lysosomal enzyme due to its acidic pH optima and the identification of lysosomal HA accumulation in the MPS IX patient.

The crystal structure of HYAL1 has been recently characterized and displays an open $\alpha\beta$ barrel conformation[103]. This protein displays a similar structure to the bee venom hyaluronidase with the exception of an additional β strand within the barrel structure and a C-terminal domain[103, 104]. The binding cleft contains numerous aromatic residues characteristic of saccharide binding proteins and a catalytic site containing a DWE amino acid sequence predicted to function by an acid-base mechanism[104]. The C-terminal domain of HYAL1 contains three disulfide bonds that display a bonding pattern characteristic of the epidermal growth factor-like (EGF-like) domain (C1-C3, C2-C4, C5-C6)[103]. This EGF-like domain contains 26 % similarity to a heparin-binding domain of an EGF-like growth factor, is found in all mammalian hyaluronidases and is suggested to function as a protein-protein interaction site[103]. However, further investigations

are required to determine the validity of this hypothesis and the significance of this domain.

1.6.1.2 Hyaluronidase 2

Hyaluronidase 2 (*HYAL2*) has the broadest expression profile of all the hyaluronidases, being expressed in all tissues with the exception of the brain[99]. In *Xenopus laevis*, ectopic overexpression of Hyal2 decreases HA and disrupts proper vitelline vessel formation, suggesting the importance of Hyal2 in regulating HA for this process[105]. HYAL2 has two known forms, a soluble lysosomal form and a membrane associated glycosylphosphatidylinositol (GPI) anchored form. The soluble enzyme has an acidic pH optima and degrades HMW HA into 20 kDa fragments[106]. The GPI-anchored form of HYAL2 (GPI-HYAL2) was initially identified due to its involvement in the pathogenesis of a Jaagsiekte Sheep Retrovirus[107]. GPI-HYAL2 is thought to be active extracellularly through the interaction between GPI-HYAL2, CD44 and a Na^+/H^+ exchanger (NHE1) to create a slightly acidic microenvironment[108]. This extracellular activity has been supported in studies using cellular overexpression or cell-free systems where GPI-HYAL2 displays a pH optimum between 6.0 and 7.0[109]. The interaction between GPI-HYAL2 and CD44 appears to be essential for extracellular enzymatic activity in both studies[108, 109]. Whether the activity of GPI-HYAL2 can be produced through interactions with other HA receptors remains to be determined.

1.6.1.3 Hyaluronidase 3

HYAL3 displays a broad, albeit low, expression profile being expressed in most tissues[110]. Human *HYAL3* expression is highest in the brain and the testes, however the mouse also displays high *Hyal3* expression within high turnover tissues such as the liver and kidney[99, 100]. The activity of HYAL3 is currently controversial. It was originally reported to contain acidic activity[111], however recent studies have been unable to verify this[109, 112].

1.6.1.4 Additional hyaluronidase genes HYAL4, HYAL5, SPAM1 and HYALP1

There are several additional genes within the hyaluronidase gene family that have a more restricted expression profile and are less likely to function in constitutive HA degradation. The Sperm Adhesion Molecule 1 (*SPAM1*) gene is the best characterized hyaluronidase gene due to its role in fertilization[113]. *SPAM1* encodes a PH-20 protein that is found in two forms, a soluble acid active form and a neutrally active GPI-anchored form found on the sperm head[114, 115]. PH-20 has three known functions including cumulus cell dispersal, Ca^{2+}-induced signaling and zona pellucida binding[116]. Mice deficient in Ph-20 are fertile despite a reduced capability for sperm to penetrate the oocyte cumulus layer[117]. Unexpectedly, hyaluronidase activity was detected in Ph-20 deficient sperm suggesting other genes may compensate in fertilization[117].

The remaining genes, *HYALP1*, *HYAL4* and *Hyal5* in mice, have little information known about their function and/or activity. *Hyal5* is found

downstream of *Spam1* on chromosome 6A2 and has only been identified in the rodent system to date. Hyal5 displays a broad pH activity range (pH 4.5 and 7.5) and is suggested to compensate for Ph-20 in the fertilization of *Spam1* null mice [101, 118]. *HYALP1* is an expressed pseudogene that contains a 28 bp deletion that causes a frameshift resulting in premature stop codons[99]. This deletion appears to have occurred recently in the evolution of this gene, as the mouse gene contains no mutation and is predicted to encode a 57 kDa protein[119]. The ability of mouse HyalP1 to degrade HA is currently controversial due to opposing *in vivo* and *in vitro* studies[118, 120]. Very little is known about HYAL4, but it has been suggested to be a chondroitinase[99].

1.6.2 Exoglycosidases

There are two exoglycosidases that remove terminal saccharides from the non-reducing end of HA, the β-hexosaminidase (HEX) isoenzymes and β-glucuronidase. The β-hexosaminidase isoenzymes function to remove the terminal N-acetyl glucosamine and N-acetyl galactosamine residues of GAG substrates. There are two major β-hexosaminidase isoenzymes, HEXA and HEXB. HEXB is composed of two β-subunits encoded by the gene *HEXB*, while HEXA is comprised of one α-subunit encoded by gene *HEXA* and one β-subunit. These enzymes may function in GAG degradation, since mice with a HexB deficiency have been reported to contain Alcian blue positive material in the brain and visceral organs, and mice deficient in both HexA and HexB display MPS-like symptoms[121, 122].

The second exoglycosidase, β-glucuronidase, is encoded by the GUSB gene and removes the terminal D-glucuronic acid saccharide. A β-glucuronidase deficiency causes a severe mucopolysaccharidosis, MPS VII, due to its essential function in the degradation of dermatan, heparan and chondroitin sulfates[9]. A mouse model of deficiency has been available since 1989 and displays features typical of MPS VII, including severe short stature, decreased limb length, hepatosplenomegaly and facial and skeletal dysmorphism[123]. While the exoglycosidases are known to remove terminal saccharide structures, their exact contribution to HA degradation remains to be determined. *In vitro* activity assays of the exoglycosidases suggest that the enzymes are capable of degrading high molecular weight HA, albeit at enzymatic rates far lower than the hyaluronidases[124].

1.6.3 Model of constitutive HA degradation

A proposal has emerged that suggests the hyaluronidases function in concert in HA catabolism[99]. Within this model (Figure 5), HYAL2 initiates HA degradation at the cell surface to produce 20 kDa fragments that are endocytosed by known receptors. The endocytic vesicles are directed to the lysosome, where degradation of these fragments continues through the combined actions of HYAL1 and the exoglycosidases. This has been supported by studies that have identified extracellular HA degradation by HYAL2[108, 109]. The role of other hyaluronidases within this model remains to be determined.

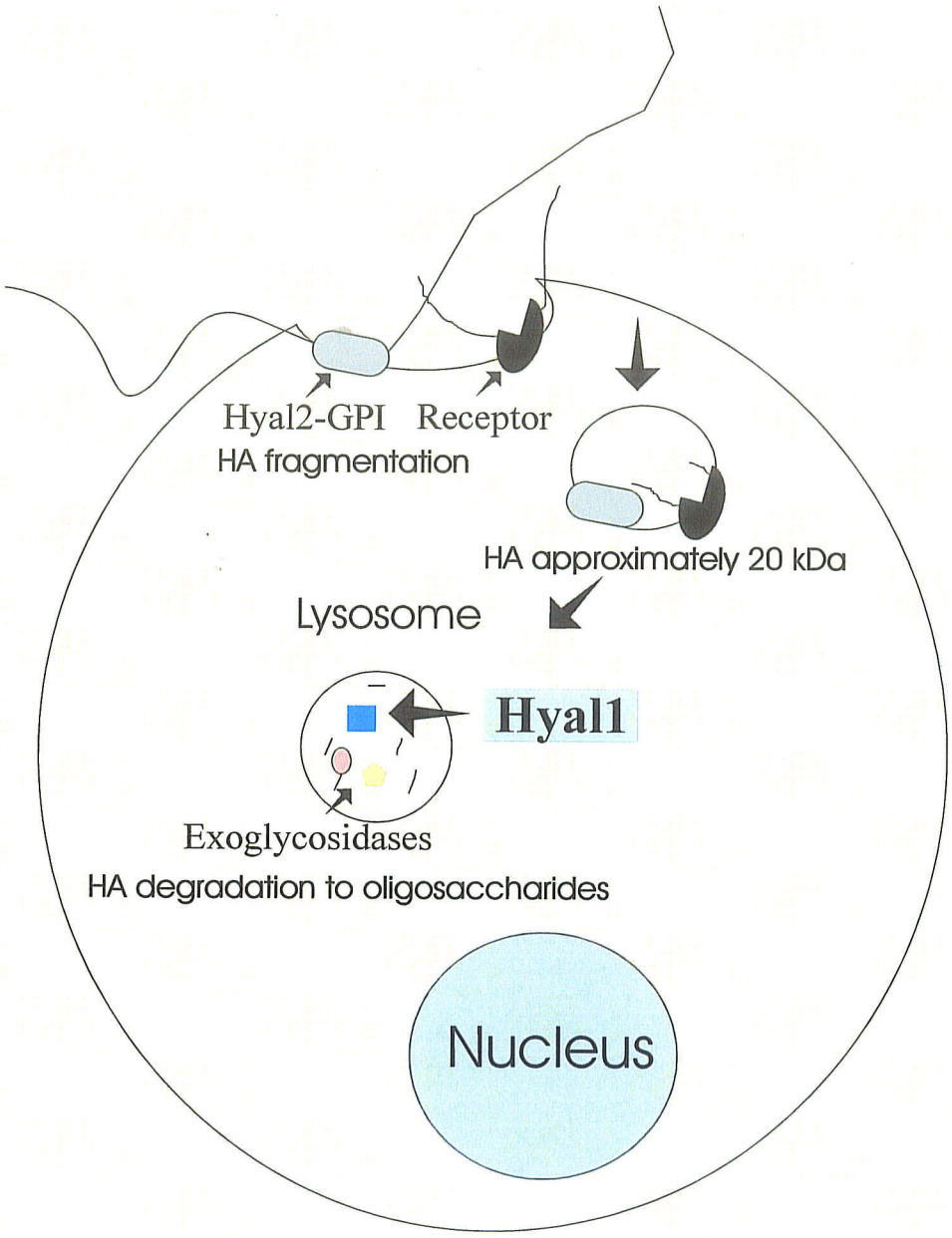

Figure 5: Model of HA degradation.

1.7 HYAL1 in cancer

The hyaluronidases and hyaluronan have been implicated in disease progression in many types of cancer (for review[78]). Elevated levels of HYAL1 have been identified in head and neck tumors, bladder cancer and prostate cancer[125-127]. As a result, hyaluronidase activity can be detected in the urine of patients with G2 or G3 bladder carcinoma and in the saliva of patients with head and neck cancer[126, 128]. This increase in urine hyaluronidase, along with urinary excretion of small HA fragments, is diagnostic for bladder cancer and can be used to determine tumor grade[128, 129]. In addition, levels of tumor HA and HYAL1 can serve as prognostic indictors of recurrence in prostate cancer[86]. Expression of HYAL1 in orthotopic models of prostate and bladder cancer promotes tumor vascularization, tumor lymph node metastasis and/or surrounding tissue invasion[130-132]. However, the mechanism by which HYAL1 and HA promote tumor growth remains controversial, but appears to be dependent on both HA and hyaluronidase levels[132-135]. More work remains to be done to understand the roles of HA and hyaluronidases in cancer.

1.8 Animal models

Animal models of disease are being used with increasing frequency due to their importance in understanding disease progression and identifying treatment options. Within lysosomal storage disorder research, murine models of MPS I have shown that the primary clinical characteristic of patients is skeletal

deformities and that substrate accumulation leading to neurological symptoms may occur over time[136]. Animal models of multiple sulfatase deficiency, MPS IIIA and MPS VI have identified that pathogenic inflammatory reactions contribute to joint dysfunction and/or that impaired autophagy contributes to neuronal death[137, 138]. However, one of the most important uses of murine models has been in determining the effectiveness of enzyme replacement, substrate deprivation and gene therapy as treatment options for lysosomal storage disorders[139-143].

The mouse as a model system has many benefits over other animal models in examining the function of a gene. Large numbers of animals can be generated in a relatively short period of time, since mice are reproductively fertile by approximately 6 weeks of age and the gestational time is between 19-20 days[144]. In addition, mice can be bred to a different genetic background and the typical lifespan of a mouse is much shorter (1.5 - 2.5 years) than larger animals[145]. Therefore, the experimental advantage to the mouse system is that a genetic deficiency can be studied on different genetic backgrounds and over the entire lifespan to determine how gene function is impacted over time and by genetic variation.

Specifically, a mouse model of Hyal1 deficiency could identify key characteristics associated with MPS IX, cells and tissues where HA accumulates and be used to study pathogenic mechanisms of disease. Given that only one MPS IX patient has been described to date, it is likely that patients are being misdiagnosed or missed at clinical presentation. The thorough characterization of

a mouse model may identify the main symptoms associated with disease thus leading to the diagnosis of additional patients. While the role of Hyal1 in tissue HA turnover has not been determined to date, a mouse model of deficiency can identify cells where Hyal1 function is essential to HA turnover and identification of cellular sites of storage can suggest the localization of Hyal1 in the cell. A mouse model of Hyal1 deficiency can be used in the future to determine the effectiveness of therapeutic strategies and given the role of HA turnover essential in various inflammatory processes, can be used to study pathogenic mechanisms of disease or injury where regulation of HA levels is necessary. Thus the creation of a mouse model of Hyal1 deficiency will greatly advance research through the past difficulties in studying the role of Hyal1 in HA turnover, as well as understand and identify the MPS IX disease characteristics and pathogenesis.

1.9 Thesis objectives and hypotheses

The objectives of my PhD thesis research were:

a) to generate, characterize and compare the phenotype of a murine model of MPS IX to the human disease.
b) to identify tissues where Hyal1 is essential to HA degradation.
c) to identify candidate compensatory and redundant genes to *Hyal1* in HA degradation.

My hypotheses were that a Hyal1 deficient mouse would model the human lysosomal storage disorder MPS IX, HA would accumulate in high turnover

tissues and that a deficiency of additional hyaluronidases and/or exoglycosidases was not necessary for disease production.

Chapter 2: Materials and Methods

All chemicals used were from Sigma-Aldrich or Fisher Scientific unless otherwise specified.

2.1 Bacterial media preparation

All bacterial cultures were grown in Miller's Luria Broth (LB), low salt LB (Invitrogen) or on LB agar plates (Invitrogen) that were made according to the manufacturer's instructions. For agar plates containing antibiotic, the media was cooled to approximately 50°C prior to the addition of ampicillin (100 μg/ml) and poured into Petri dishes.

SOC media (8.5 mM NaCl, 2.5 mM KCl, 2% bacto-tryptone [Difco], 0.25% bacto-yeast extract [Difco]) was supplemented with sterile 0.01 M $MgCl_2$ and 0.02 M glucose, aliquoted and stored at -20°C until use.

2.2 Transformation of plasmid DNA

Electroporation of plasmid DNA or ligation mixture was performed using an Electro Cell Manipulator 600 (BTX Inc.) according to the manufacturer's instructions.

2.2.1 Preparation of electrocompetent cells

Glycerol stocks of DH10B (F⁻ *mcr*A Δ(*mrr- hsd*RMS- *mcr*BC) φ80*lacZ*ΔM15 Δ*lacX*74 *rec*A1 *end*A1 *ara*D139 Δ(*ara,leu*) *gal*K λ⁻*rps*L *nup*G), DH5α (F-

φ80*lac*ZΔM15 Δ(*lac*ZYA-*arg*F) U169 *rec*A1 *end*A1 *hsd*R17 (r_k-, m_k+) *pho*A *sup*E44 λ- *thi*-1 *gyr*A96 *rel*A1) or GM2163 (F⁻ *dam-13::*Tn *9 dcm-6 hsdR2 leuB6 his-4 thi-1 ara-14 lacY1 galK2 galT22 xyl-5 mtl-1 rpsL136 tonA31 tsx-78 supE44* McrA⁻ McrB⁻) *E.coli* bacterial cells were streaked on a LB agar plate and incubated overnight at 37°C. A single colony was inoculated into 3 ml of LB and grown overnight at 37°C with shaking. This starter culture was diluted 1/400 and grown in low salt LB broth at 37°C with shaking until it reached an OD_{600} between 0.5 and 1.0 (approximately 1 x 10^{10} cells). Bacterial cells were pelleted at 4000 x g for 15 min at 4°C. To wash the bacterial cells of residual salts, the bacterial cell pellet was resuspended in 1 volume of sterile ice cold double distilled water. Cells were collected again by centrifugation at 4000 x g for 15 min at 4°C. Washing and pelleting of bacterial cells was repeated twice using decreasing volumes of sterile ice cold double distilled water, 0.5 volumes and 0.02 volumes respectively. Bacterial cells were resuspended in 0.002 volumes of cold sterile 10% glycerol, aliquoted, frozen on dry ice and stored at -80°C until use.

2.2.2 Electroporation

An aliquot of electrocompetent DH10B, DH5α or GM2163 *E.coli* cells was thawed on ice prior to use. Plasmid DNA (1 ng) or ligation mix (1 μl) was mixed with the electrocompetent cells and electroporated using a sterile cold 1 mm gap electroporation cuvette (BTX) according to recommended conditions (2.5 kV/Resistance high voltage, 129 ohm resistance, 1.3 kV charging voltage). After electroporation, 960 μl of pre-warmed SOC media was added and cells were allowed

to recover for 1 hr at 37°C. Either 50 µl, 100 µl or 200 µl of culture was plated onto a LB agar plate containing ampicillin (100 µg/ml) and incubated overnight at 37°C.

2.3 Plasmid DNA isolation

2.3.1 Small scale

Isolation of plasmid DNA was performed using a modified alkaline lysis method [146, 147]. Plasmids were grown in DH10B, DH5α or GM2163 *E.coli* cells. Single colonies were inoculated into 3 ml of LB media containing 100 µg/ml of ampicillin and grown for either 8 hrs or overnight at 37°C with shaking. Half of the bacterial culture, 1.5 ml, was pelleted by centrifugation and the supernatant was discarded. Cell pellets were resuspended in 100 µl of GTE solution (50 mM glucose, 25 mM Tris-Cl pH 8.0, 10 mM EDTA, 0.1 µg/ml RNaseA) and incubated for 5 min at room temperature. Resuspended cells were mixed with 200 µl of lysis solution (0.2 N NaOH, 1% SDS) and incubated for 5 min on ice. After lysis, 150 µl of neutralization solution (5 M potassium acetate [pH 4.8]) was added and thoroughly mixed to precipitate genomic DNA, proteins and cell debris. Precipitates were pelleted by centrifugation at room temperature for 3 min and the supernatant was collected. Plasmid DNA was precipitated in 0.8 ml of 95% ethanol for 20 min at -80°C and pelleted by centrifugation for 5 min at room temperature. After the supernatant was discarded, plasmid DNA was washed with 500 µl of 70% ethanol prior to centrifugation for 3 min. The pellet was air-dried and resuspended in 50 µl of sterile double distilled water.

2.3.2 Large scale

For large scale plasmid isolation, bacteria were inoculated from a 50% glycerol stock into 3 ml of LB media and grown for 8 hrs at 37°C with shaking. The starter culture was diluted 1/500 or 1/1000 into 25 ml of LB broth containing ampicillin (100 μg/μl) and incubated overnight at 37°C with shaking. Bacterial cells were pelleted by centrifugation at 5000 x g for 15 min at 4°C and resuspended in 10 ml of P1 buffer (50 mM Tris-Cl pH 8.0, 10 mM EDTA, 100 μg/μl RNase A). To lyse cells, an equal volume of P2 buffer (200 mM NaOH, 1% SDS) was added to the suspension, mixed gently and incubated for 5 min at room temperature. Genomic DNA, proteins and cell debris were precipitated with 10 ml of cold P3 buffer (3.0 M potassium acetate [pH 5.5]). The lysate mixture was poured into a QIAfilter cartridge (Qiagen Inc.), incubated for 10 min and filtered into a Qiagen-tip 100 column pre-equilibrated with 4 ml of QBT buffer (750 mM NaCl, 50 mM MOPS pH 7.0, 15% isopropanol, 0.15% Triton X-100). The column was washed twice with 10 ml of QC buffer (1.0 M NaCl, 50 mM MOPS pH 7.0, 15% isopropanol) and plasmid DNA was eluted with 5 ml of QF buffer (1.25 M NaCl, 50 mM Tris-Cl pH 8.5, 15% isopropanol). Eluted plasmid DNA was precipitated with 3.5 ml of isopropanol and pelleted by centrifugation at 10,000 x g for 30 min at 4°C. The pellet was washed with 70% ethanol, centrifuged at 10,000 x g for 10 min, air-dried and resuspended in sterile double distilled water.

2.3.3 Large Scale plasmid isolation for embryonic stem (ES) cell transfection

For a large scale culture, 100 ml of culture was prepared following the approach described in section 2.3.2. Bacterial cells were pelleted by centrifugation at 5000 x g for 15 min at 4°C and resuspended in 20 ml of P1 buffer. Cell lysis and removal of cell components was performed as described in section 2.3.2 using 20 ml of P1, P2 and P3 buffer. The lysate was poured into a QIAfilter cartridge (Qiagen Inc.), incubated for 10 min at room temperature and filtered into a new 50 ml conical tube. The filtrate was treated with 5 ml of endotoxin removal buffer for 30 min on ice to remove endotoxins and applied to a Qiagen-tip 500 column pre-equilibrated with 4 ml of QBT buffer. The column was washed twice with 30 ml of QC buffer and plasmid DNA was eluted with 15 ml of QF buffer. Plasmid DNA was precipitated with 10.5 ml of isopropanol and pelleted by centrifugation at 10,000 x g for 30 min at 4°C. The supernatant was removed and pellet washed with 70% ethanol prior to centrifugation at 10,000 x g for 10 min. Plasmid DNA was air-dried and resuspended in sterile endotoxin-free water (Invitrogen).

2.4 Quantitation of nucleic acids

DNA and RNA absorbances were determined at 260 nm in a 1 ml cuvette using a Pharmacia BiotechUltraspec 1000 spectrophotometer. DNA and RNA concentrations were determined by the formulae:

[DNA]= Absorbance at 260 nm x 50 μg/ml x dilution factor

[RNA]= Absorbance at 260 nm x 40 μg/ml x dilution factor

RNA purity was assessed by determining the absorbance at 280 nm and calculating the $A_{260/280}$ ratio.

2.5 Ethanol precipitation

DNA was precipitated by adding 0.1 volumes of 3 M sodium acetate (pH 4.8) and 2.5 volumes of 95% ethanol, thoroughly mixing and incubating at -80°C for 30 min. DNA was pelleted by centrifugation and washed with 70% ethanol. The pellet was air-dried and resuspended in buffer or double distilled water.

2.6 Restriction enzyme digestion

Restriction enzyme digests were carried out by adding DNA (0.5 µg for clone screening, 5-10 µg for vector or insert preparation, 40 µg for targeting construct linearization, 2-3 µg for genomic DNA) into 20 or 100 µl of restriction enzyme reaction buffer and incubated with 10-20 units of restriction enzyme at the recommended temperature for 3 hrs. Restriction enzyme digestion times varied when necessary to ensure complete digestion of DNA. Double or triple enzyme digests were performed as described above in a reaction buffer compatible with all enzymes used. A list of enzymes and specific reaction conditions used is given in Table 3.

Table 3: Restriction enzymes and conditions in generating or screening of *Hyal1* targeting constructs, probes and verification of targeting events.

Restriction Enzyme (s)	Cleavage Site (s)	Reaction Buffer	Temperature	BSA Addition
EcoRV	GAT/ATC	NEB3	37°C	Yes
PflFI	GACN/NNGTC	NEB4	37°C	Yes
NsiI	ATGCA/T	NsiI	37°C	No

EcoRI	G/AATTC	EcoRI	37°C	No
XbaI	T/CTAGA	NEB2	37°C	Yes
XhoI	C/TCGAG	NEB3	37°C	Yes
BglII	A/GATCT	NEB3	37°C	Yes
HindIII	A/AGCTT	NEB2	37°C	No
NdeI	CA/TATG	NEB2	37°C	No
PstI	CTGCA/G	NEB3	37°C	Yes
MscI	TTG/CCA	NEB3	37°C	Yes
SalI	G/TCGAC	NEB3	37°C	Yes
NotI	GC/GGCCGC	NEB3	37°C	Yes
ApaI/SbfI	GGGCC/C CCTGCA/GG	NEB4	37°C	Yes
EcoRV/PflFI	GAT/ATC GACN/NNGTC	NEB 4	37°C	Yes
PflFI/HindIII	GACN/NNGTC A/AGCTT	NEB4	37°C	No
Hinc II/SalI	GT(C,T)/(C,T)AC G/TCGAC*	NEB3	37°C	Yes
KpnI/XhoI	GGTAC/C C/TCGAG	NEB1	37°C	Yes
NdeI/XbaI	CA/TATG T/CTAGA	NEB2	37°C	Yes
NotI/SalI	GC/GGCCGC G/TCGAC	NEB3	37°C	Yes
MscI/NaeI	TTG/CCA GCC/GGC	NEB1	37°C	Yes
SfiI/AflIII	GGCCNNNN/NGGCC AC(A,G)/(A,G)GT*	NEB2	37°C	Yes
XbaI/XhoI	T/CTAGA C/TCGAG	NEB2	37°C	Yes
SalI/SspI/EcoRI	G/TCGAC AAT/ATT G/AATTC	NEB3	37°C	Yes

* All possible nucleotides recognized by the restriction endonuclease are given in brackets.

2.7 Preparation of vector and inserts for blunt-end ligation

2.7.1 Filling in 5' overhangs of vector and insert DNA

Vector and insert DNA were ethanol precipitated and resuspended in 1x Buffer 2 (New England Biolabs) supplemented with 33 μM dNTPs. One unit of DNA polymerase I (Klenow; New England Biolabs) was added per μg of DNA and incubated for 15 min at room temperature. Klenow was heat inactivated at 65°C for 20 min and the reaction was stored at -20°C until further use.

2.7.2 Removal of 3' overhangs from vector DNA

After restriction enzyme digestion, vector DNA was ethanol precipitated and resuspended in 1x Thermopol reaction buffer (New England Biolabs). The 3' overhangs were removed by adding 1-2 units of Vent DNA polymerase (New England Biolabs) and incubating at 72°C for 20 min. After removal of the ends, the vector DNA was separated by agarose gel electrophoresis and gel purified as described in sections 2.8 and 2.9.

2.7.3 Dephosphorylation of vector ends

Vector DNA was ethanol precipitated and resuspended in 1x Buffer 3 (New England Biolabs). Varying amounts of calf intestinal alkaline phosphatase (CIP; New England Biolabs) was added to vector DNA to yield a final concentration of 0.5 units/μg of DNA. The mixture was incubated for 1 hr at 37°C. Vector DNA was separated by agarose gel electrophoresis and gel purified as described in sections 2.8 and 2.9.

2.8 Separation of nucleic acids by agarose gel electrophoresis

Agarose gels of 0.8% - 2.0% were used depending on the size of the expected DNA fragments. Electrophoresis grade agarose (Invitrogen) was dissolved in 100 ml of 1X TAE (40 mM Tris-acetate, 1 mM EDTA) or 1X TBE (90 mM Tris-borate, 2 mM EDTA) by heating for 2 min at full power in a microwave oven. After cooling to approximately 50°C, ethidium bromide (0.5 µg/ml) was added to allow visualization of DNA and the mixture was poured into a horizontal gel tray. To size DNA fragments, 0.5 µg of 1 kb ladder (Invitrogen, Fermentas or New England Biolabs) was used as a molecular weight marker. DNA samples or molecular weight markers were mixed with loading dye to give a final concentration of 0.04 % bromophenol blue, 0.04 % xylene cyanol, 5 % glycerol and loaded into agarose gel wells. DNA was separated by size using a horizontal electrophoresis chamber at a constant voltage between 50-115V. Ethidium bromide/DNA complexes were visualized by UV light.

For RNA separation, 0.8% or 1.0% agarose gels were used for all experiments. RNase-free agarose LE (Ambion) was dissolved in 100 ml of 1x BPTE buffer (300 mM Bis-Tris, 100 mM Pipes, 10 mM EDTA) by heating for 2 min at full power in a microwave oven. After allowing the gel mix to cool to 50°C, the gel was poured into a horizontal gel tray. To size RNA samples, a ssRNA ladder (New England Biolabs) was used as a molecular weight marker. Samples or molecular weight markers were mixed with an equal volume of NorthernMax-Gly sample loading dye (Ambion), containing ethidium bromide, and heated at 50°C for 30 min. Samples were loaded into agarose gel wells and electrophoresis was performed at 5

V/cm in a horizontal gel electrophoresis chamber in 1x BPTE. Ethidium bromide/RNA complexes were visualized by UV light.

2.9 Gel isolation of DNA

DNA was isolated from agarose gels using GeneClean III (MP Biomedicals), QIAquick (Qiagen Inc.) or QIAEX II (Qiagen Inc.) kits according to the manufacturer's recommendations. All samples were separated by agarose gel electrophoresis and the desired bands cut from the agarose gel after UV visualization. The gel pieces were weighed and converted to volumes using the approximation 0.1 mg = 0.1 ml. For the GeneClean III kit, 3 volumes of NaI solution was added to the mixture and incubated at 55°C for 5 min to dissolve the agarose gel. To bind DNA, EZ-Glassmilk solution was added and allowed to bind to DNA for 5 min at room temperature. EZ-GlassMilk and DNA complexes were pelleted by centrifugation for 30 s and the supernatant was discarded. The pellet was washed twice in NEWwash solution, centrifuged for 10 s and air-dried. DNA was eluted by resuspending the pellet in water and centrifuging for 30 s. The supernatant was collected and DNA quantitated by comparison to known quantities of size standards (Gibco 1 kb ladder) using ethidium bromide visualization after separation by agarose gel electrophoresis.

A similar procedure was used with the QIAquick kit using a QG agarose dissolution buffer and a 10 min incubation at 50°C. For DNA fragment sizes >4 kb, 1 volume of isopropanol was added to the dissolution buffer to allow DNA binding prior to application of the sample to the QIAquick column. The column was washed once with QG buffer (Qiagen Inc.) and twice with PE buffer (Qiagen Inc.). During

the wash steps, flow through material was discarded after 1 min centrifugations. The column was dried using a final 1 min centrifugation and DNA was eluted from the column with 50 µl of EB buffer (Qiagen Inc.) or double distilled water (pH 8.0).

The QIAEX II kit (Qiagen Inc.) had a similar procedure to those above, but with unique buffers for dissolution and the first wash. The addition of the binding beads, QIAEXII suspension mix, occurred prior to a 10 min incubation at 50°C to allow simultaneous agarose gel dissolution and DNA binding. In addition, 2 volumes of water were added to the dissolution buffer for DNA fragments >4 kb and samples were spun to pellet QIAEXII/DNA complexes. Wash supernatants were discarded and the resulting pellet was air-dried. DNA was eluted by resuspension in 20 µl of 10 mM Tris-Cl (pH 8.5) using recommended incubation temperatures, centrifuged for 30 s and the supernatant was collected into a micro-centrifuge tube.

2.10 Ligation

All ligation reactions were performed using a 1:1 or a 3:1 insert to vector molar ratio with a starting vector DNA concentration of 100 ng. Vector and insert DNA was isolated from agarose gels and DNA was added to 1x T4 DNA ligase buffer (New England Biolabs) with 40 units of T4 DNA ligase (New England Biolabs). The ligation reaction mixture was incubated for 2 hrs or overnight at room temperature.

2.11 Polymerase Chain Reaction (PCR) amplification

DNA was amplified from a PAC (P1 artificial chromosome) clone (452D10) containing the *Hyal1*, *Hyal2* and *Hyal3* gene regions, R1 ES cell genomic DNA or mouse tail genomic DNA. Genomic DNA or PAC 452D10 DNA (100 ng) was added to the PCR reaction mixture (100 ng forward primer, 100 ng reverse primer, 0.2 mM dNTPs, 2.5 units Taq DNA polymerase [Invitrogen], 20 mM Tris-Cl [pH 8.4], 50 mM KCl , 1.5 mM $MgCl_2$) to make the final volume to 50 µl. For TA cloning of PCR products, a high fidelity EasyA Cloning polymerase enzyme (Stratagene) was used in the PCR reaction mixture (100 ng forward, 100 ng reverse primer, 0.2 mM dNTPs, 2.5 units Easy-A High Fidelity cloning enzyme, 1x Easy A PCR buffer containing 2 mM $MgCl_2$).

PCR reaction mixes, and a negative control containing no template, were overlaid with mineral oil and amplified using either a Perkin Elmer Thermal Cycler or a MJ Research Minicycler. PCR cycling conditions were optimized based on the individual primer pairs. Annealing temperatures, elongation times, $MgCl_2$ concentrations and Taq DNA polymerase units were altered as necessary upon optimization.

Table 4: Forward and reverse primers used for PCR amplification.

Forward Primer 5'→3'	**Forward Primer Location**	**Reverse Primer 5'→3'**	**Reverse Primer Location**	**Product Size**
WPG 365 gctactgagtctgcacttgtgc	Region between *Hyal1/ Hyal2*	**WPG 332** ctggacggttctgtgttcatgagg	*Hyal1* exon 1	3.2 kb
WPG 376 ctgacttctcaggactggcagtcattgctggcgcccacggt	*Hyal1* exon 2 mutagenic primer	**WPG 377** ggtgttcagtgtgtgcag	*Hyal1* exon 4	1.5 kb
WPG 379 cgccagcttctaagctg	*Hyal1* exon 2	**WPG378** ttgaaggccaccgtgggcgccaagcaatgactgccagtcctcctgag	*Hyal1* exon 2 mutagenic primer	1.0 kb
WPG 379 cgccagcttctaagctg	*Hyal1* exon 1	**WPG 377** ggtgttcagtgtgtgcag	*Hyal1* exon 4	2.5 kb
WPG 367 agctggcctctggtgcaaggatct	*Hyal2* exon 4	**WPG 368** gcacaagtgcagactcagtagc	Intergenic region between *Hyal1/Hyal2*	340 bp
WPG 342 tggattccacctgtaggccggagct	*Fus2* exon 2	**WPG 343** caggcagcttgggaactgggagctc	*Fus2* exon2	440 bp
WPG 379 cgccagcttctaagctg	*Hyal1* exon 1	**WPG 617** atcgccttctatcgcctt	Neo coding region	1.0 kb
WPG 618 gtcatagccgaatagcctct	Neo coding region	**WPG 198** agctgcactggtcacgttctc	*Hyal1* exon 4	1.3 kb
WPG 610 cttggtggagagaggctattc	Neo coding region	**WPG 611** aggtgagatgacaggagatc	Neo coding region	270 bp
WPG 612 ctgggacagcaaggacattt	*Hyal1* exon 2	**WPG 613** cagtgctgcaggcaaataaa	*Hyal1* exon 2	340 bp
WPG 182 tttccaaggctctaacatgac	*Hyal1* exon 2	**WPG 198** agctgcactggtcacgttctc	*Hyal1* exon 4	900 bp
WPG 199 ctggagcacgcctgggggag	*Hyal1* exon 3	**WPG 198** agctgcactggtcacgttctc	*Hyal1* exon 4	160 bp
WPG 190 tgccctacgtccagatcttc	*Hyal1* exon 2	**WPG 198** agctgcactggtcacgttctc	*Hyal1* exon 4	200 bp

2.12 TA cloning of PCR amplification products

PCR products were TA cloned into a pCR2.1 vector using the Original TA Cloning kit (Invitrogen) according to the manufacturer's instructions. PCR products were purified from agarose gels and quantitated by ethidium bromide intensity in comparison with known amounts of size standards from the Gibco 1 kb ladder. Vector DNA (50 ng) was ligated at a 1:1 (insert: vector) ratio overnight at 14°C. The ligation mix was transformed into INVαF' (F'*end*A1*rec*A1*hsd*R17(r_k^-,m_k^-)*sup*E44*thi*-1*gyr*A96*rel*A1□80*lacZ*ΔM15Δ(*lacZ*YA-*arg*I)U169λ' chemically competent *E.coli* bacterial cells.

2.13 Sequencing

Automated sequencing using the Sanger method was performed at The Centre of Applied Genomics (Toronto, ON) using an ABI 3730XL instrument.

2.14 Phenol : chloroform purification of Hyal1 targeting constructs

Linearized *Hyal1* targeting constructs were thoroughly mixed with an equal volume of phenol: chloroform: isoamyl alcohol (25:24:1) and centrifuged at room temperature for 3 min. Avoiding the interface, the aqueous phase was removed and mixed with an equal volume of chloroform: isoamyl alcohol (24:1). Organic phases were back extracted with either 100 or 200 µl of TE buffer and the aqueous phase was pooled. Linearized DNA was ethanol precipitated and resuspended in endotoxin free water (Invitrogen) to a final concentration of 1 µg/µl.

2.15 Mouse ES cell transfection

All cell culture reagents were from Invitrogen unless indicated otherwise.

2.15.1 ES cell lines used for targeting

A R1 ES cell line[145] was used for the targeting of the p*Hyal1* Neo/TK construct. The R1 ES cell line was derived from the inner cell mass of blastocyst embryos of a chinchilla C129/Sv x agouti C129/Sv-CP mouse mating.

A D3H ES cell line was used for the p*Hyal1* β-geo targeting construct. The D3H ES cell line was sub-cloned from the original D3 ES cell line (129S2/SvPas)[148] and was a kind gift from Dr. Geoff Hicks (University of Manitoba).

2.15.2 Mitotically inactivated mouse embryonic fibroblast (MEF) cells

Mitomycin C treated Neo resistant MEF cells were supplied by the Samuel Lunenfeld Institute for use in culturing the R1 ES cell line. Neomycin resistant primary MEF cells used for irradiation were a kind gift of Dr. Geoff Hicks (University of Manitoba). Primary neomycin resistant MEF cells were grown in Dulbecco's Modified Eagle Medium (DMEM) containing 10% fetal bovine serum (FBS), 1 mM sodium pyravate, 2 mM Glutamax, 50U/ml penicillin and 50 U/ml streptomycin in a 150 mm tissue culture dish. Upon attaining confluence, cells were dissociated with 0.05% trypsin and divided into 5 additional 150 mm tissue culture dishes. At confluence, MEF cells were collected by trypsinization with 0.05 % trypsin and neutralization with 1 volume of DMEM, pelleted by centrifugation and

resuspended in DMEM. Cells were counted prior to irradiation with 3000 rads of γ irradiation for 11.6 min (Cancercare Manitoba). After irradiation, MEF cells were collected by centrifugation and frozen at a concentration $2x10^6$ cells/ml in freezing media (50% FBS, 12% dimethylsulfoxide (DMSO) in supplemented DMEM).

2.15.3 Culturing conditions

ES cell lines were grown in DMEM (4.5 g/L high glucose) containing 0.1 mM non-essential amino acids , 1 mM sodium pyravate, 0.1 mM β-mercaptoethanol, 2 mM L-glutamine, 50U/ml penicillin and 50 U/ml streptomycin, 15% ES cell quality fetal bovine serum (FBS) (Hyclone, Cansera) and 1000 U/ml leukemia inhibitory factor (LIF) at 37°C with 5% CO_2. ES cells were maintained on MEF cells that had been mitotically inactivated using γ irradiation or mitomycin C treatment. The R1 ES cell lines were grown on 0.1% gelatin during drug selection. For selection, ES cell media was supplemented with Geneticin (G418) at 150 μg/ml – 250 μg/ml. A 2 mM concentration of gangcyclovir was used for negative selection in the p*Hyal1* Neo/TK targeting. G418 concentrations of 2.0 mg/ml were used for selection of putative *Hyal1* -/- ES cell lines.

2.15.4 Transfection

ES cells were harvested 2 days after the last passage at approximately 80% confluence using 0.25% trypsin. Cells were pelleted by centrifugation and resuspended in ES cell electroporation buffer (Specialty Media) at a concentration of

7 x 10^6cells/ml. DNA (20-40 μg) was mixed with 0.8 ml of ES cells in a pre-cooled 4 mm gap electroporation cuvette and electroporated using 250 V and 500 μF. Approximately 2.8 x 10^6 cells were plated per 100 mm tissue culture dish and ES cells were allowed 1-2 days to recover prior to the addition of selective media.

2.15.5 Cell freezing

ES cells were harvested with 0.25% trypsin, centrifuged, washed with phosphate buffered saline (PBS) without Ca^{2+} or Mg^{2+} and resuspended at 5 x 10^6 cells/ml in 10% FBS, 10% dimethyl sulfoxide (DMSO), 80% DMEM containing all supplements. Cryovials were placed at -80°C and frozen slowly with an approximate temperature change of 1°C/min. Additionally, 96 well plates containing putatively positive ES cell lines were frozen by trypsinization, resuspension and neutralization with DMEM and addition of an equal volume of ES cell freezing media (20% FBS, 20% DMSO, 60% DMEM containing all supplements). A thin layer of sterile mineral oil was overlaid in the wells and plates were wrapped in an insulating pad to allow slow cooling. The 96 well plates were stored at -80°C until putatively positive ES cell lines were thawed.

2.15.6 ES cell thawing and expansion

Plates containing positive ES cell lines were thawed quickly in a 37°C tissue culture incubator. The contents of positive wells were mixed with 0.1 ml of warm DMEM, by placing it under the mineral oil, and cells were transferred into a 15 mm

MEF cell-covered tissue culture dish. Fresh DMEM containing all supplements was added the following day. ES cells were split at approximately 80% confluency into new tissue culture dishes with incremental size increases at each passage until culturing on a 60 mm dish. Three cryovials were frozen from a 60 mm dish and stored in liquid N_2 until use.

2.16 ES cell genomic DNA isolation

For screening of putatively positive ES cell clones, duplicate 96 well plates were created and ES cell lines were allowed to grow to confluence. Genomic DNA was isolated directly within the 96 well plate following previously published protocols[149]. Lysis buffer (50 μ per well; 10 mM Tris-Cl pH 7.5, 10 mM EDTA, 10 mM NaCl, 0.5% sarcosyl, 1 mg/ml Proteinase K) was added, wells were sealed with parafilm and the 96 well plate was incubated in a humid chamber at 55°C overnight. The following day, 100 μl of precipitation solution (0.075 NaCl in cold 100 % ethanol) was added and incubated for 1 hr at RT. The supernatant was discarded and the pellet was washed 3 times with 70 % ethanol. The genomic DNA was air-dried and resuspended in 40 μl of restriction enzyme digestion mix along with the addition of 100 μg/ml RNaseA and 1 mM spermidine.

2.17 Southern blot analysis

2.17.1 Transfer

Genomic DNA was separated by agarose gel electrophoresis and the gel was trimmed to remove unnecessary portions of agarose. The gel was incubated in denaturation solution (1.5 M NaCl, 0.5 N NaOH) for 45 min and neutralization solution (1 M Tris [pH 7.4], 1.5 M NaCl) for 30 min at room temperature. After equilibration for 10 min in 20x SSC (3.0 M NaCl, 0.3 M sodium citrate [pH 7.0]), genomic DNA was transferred to a Hybond N^+ (GE Healthcare) or Immobilon Ny^+ (Millipore) nylon membrane by upward capillary transfer overnight in 20x SSC. The membrane was washed briefly in 6x SSC (0.9 M NaCl, 0.09 M sodium citrate [pH 7.0]) and UV cross-linked according to the manufacturer's instructions from the membrane.

2.17.2 Preparation of DNA probes

The 5' external probe was generated by PCR amplification using primers WPG 367 and WPG 368 to generate a 340 bp DNA probe. The 3'external probe was generated by PCR amplification using primers WPG 342 and WPG 343 to produce a 440 bp probe. The internal Neo probe was generated by a restriction enzyme digest of the pGT-N28 plasmid (New England Biolabs) with MscI and NaeI to produce a 420 bp DNA fragment as a probe. All probes were separated by agarose gel electrophoresis, purified by gel extraction and quantitated. Probes were radioactively labeled by random priming through the incorporation of ^{32}P-dCTP using a Rediprime II (GE Healthcare) reaction assay. Free nucleotides were removed by chromatography using a ProbeQuant G-50 Micro column (GE Healthcare).

2.17.3 Hybridization

Non-specific binding of the probe was blocked by incubating the blot in hybridization buffer (0.1% Ficoll, 0.1% polyvinylpyrrolidone, 0.1% bovine serum albumin [Pentax fraction V], 0.75 M NaCl, 0.075 M sodium citrate [pH 7.4] , 0.2% SDS) with 100 μg/ml of heat denatured salmon sperm DNA or Expresshyb (Clontech) at 60°C. The blot was incubated in fresh hybridization solution containing half of the heat denatured ^{32}P- labeled mix and incubated for 4 hrs or overnight at 60-65°C. Non-specific binding was removed by washing with wash buffer 1 (0.3M NaCl, 0.03 M sodium citrate [pH 7.4], 0.05% SDS) for 30 min at room temperature, followed by a second wash in wash buffer 2 (15 mM NaCl, 1.5 mM sodium citrate [pH 7.4], 0.1% SDS) at increasing temperatures until a clean signal was visualized by autoradiography using X-OMAT MS film (Kodak).

2.18 Blastocyst injection and aggregation of ES cells

Blastocyst injections and aggregation were performed by the Transgenic Core Facility at the University of Manitoba in collaboration with Dr. G. Hicks and Dr. H. Ding. All procedures were performed according to previously published protocols[144]. ES cells were expanded and injected into C57Bl/6 blastocysts or aggregated with CD1 diploid embryos (0.5 days post coitus). Blastocysts that had been successfully injected or aggregated with R1 ES cells were transferred into the uteri of pseudo-pregnant female CD1 mice.

2.19 Protein extraction and quantification

2.19.1 Cell or tissue lysis

ES cells were sonicated in PBS (137 mM NaCl, 2.7 mM KCl, 10 mM Na_2HPO_4, 2 mM KH_2PO_4 [pH 7.4]). Approximately 30 mg of liver tissue was homogenized using a polytron in 1 ml of lysis buffer (10 mM imidazole, 0.25 M sucrose) and centrifuged to remove cell debris. Supernatant was collected, aliquoted and stored at -80°C until use.

2.19.2 Determination of protein concentrations

Protein concentrations were determined by the Bradford method [150] using a BioRad assay (BioRad) according to the manufacturer's instructions. Protein samples were made up to 800 µl in water, mixed with 200 µl of BioRad reagent and incubated for 5 min at room temperature. A control sample containing water, BioRad reagent and an equivalent amount of lysis buffer was used to calibrate absorbance readings to zero. The absorbance of controls, samples, and standards were determined at 595 nm using a Pharmacia BiotechUltraspec 1000 spectrophotometer and protein concentrations were determined by comparison with a gamma globulin standard curve.

2.20 Polyacrylamide gel electrophoresis containing SDS (SDS-PAGE)

Separation of proteins (30 µg liver lysate, 56 µg ES cell lysate) was performed using 7.5% or 10% 1.5 mm acrylamide gels. Polyacrylamide gels were made using

7.5 ml of resolving gel mix (40 mM Tris-Cl [pH 8.8], 0.1% SDS, 7.5 or 10 % acrylamide (29: 1 acrylamide:bisacrylamide). After adding 50 µl of 10% ammonium persulfate and 10 µl of TEMED, gels were cast in a Mini Protean II (BioRad) vertical gel casting apparatus and allowed to polymerize for 1 hr at room temperature. Stacking gels were poured using 2.5 ml of stacking gel mix (60 mM Tris-Cl [pH 6.8], 4% acrylamide and 0.1% SDS, 0.1 % APS, 0.01% µl TEMED) and allowed to polymerize for 20 min at room temperature. Samples and protein standards were prepared by mixing with 4x Laemmli sample buffer (8% SDS, 0.25 M Tris-Cl [pH 6.8], 25% glycerol, 100 mM dithiotreitol [DTT], 0.01% bromophenol blue) and water to get a final concentration of 1x Laemmli buffer. Samples were boiled for 5 min, loaded onto the polyacrylamide gel and separated by electrophoresis in running buffer (25 mM Tris base, 192 mM glycine, 0.1 % SDS) at room temperature using 150 V of constant voltage.

2.21 Immunoblot analysis

2.21.1 Transfer

After separation of proteins by SDS-PAGE, proteins were transferred to nitrocellulose using a modified method[151]. The gel and nitrocellulose membrane was sandwiched between pre-cut Whatman paper and transfer sponges. All cut Whatmann, nitrocellulose and sponges used were wet with transfer buffer (25 mM Tris base, 192 mM glycine, 20% methanol) prior to assembly. The transfer assembly was placed into a transfer clamp holder and placed in a Mini Trans-Blot Cell apparatus (BioRad) with the nitrocellulose membrane closest to the positive

electrode. The transfer chamber was filled with ice cold transfer buffer and proteins were transferred to nitrocellulose at 100V for 1 ½ hrs at 4°C. After transfer, the blot was rinsed with water and used for the blotting procedure.

2.21.2 Protein detection

To ensure proper quantitation and transfer of proteins, the blot was stained in Ponceau S (0.2% Ponceau S, 1% acetic acid) and rinsed with water to visualize protein bands. Ponceau S stain was removed by incubation in TBST (10 mM Tris-Cl [pH 7.4], 150 mM NaCl, 0.1 % Tween-20) until no remaining stain was visualized. Blots were blocked for 1 hr in blocking solution (5 % skim milk powder/TBST), then incubated overnight in primary anti-Hyal1 antibody (1D10; 0.5 µg/ml in 1 % skim milk/TBST) [100]. Non-specific binding was removed by washing the blot in TBST for 15 min three times. The blot was incubated for 1 hr with a goat anti-mouse secondary antibody conjugated to horse radish peroxidise (HRP) (Jackson) at 1: 7500 or a Trueblot ULTRA anti-mouse conjugated to HRP (eBioscience) secondary antibody (1:1000) at room temperature. Dependent on the secondary antibody used, the blots were either washed four times (10 min) or ten times (6 min) in TBST. Proteins were detected using chemiluminescent detection reagents, Immobilon (Millipore) or ECL Plus (GE Healthcare), according to manufacturer's instructions. Blots were exposed to BioMax Light film (BioMax) or CL-X Posure film (Pierce) until bands could be visualized after development.

2.22 Native Zymography

Separation of protein samples (30-50 μg), as well as human (1 μl) and mouse (5 μl) serum, was performed on 7% polyacrylamide gels with a 0.75 mm thickness. All solutions, Laemmli buffer and running buffers contained no SDS or DTT. Gels were prepared as described in 2.19, but contained 0.18 mg/ml umbilical cord HA. Protein samples were loaded onto polyacrylamide gels without boiling and separated by electrophoresis at 4°C using a constant current of 20 mA.

The gel was equilibrated with activity assay buffer (0.1M formate, 0.15 M NaCl [pH 3.8]) and incubated overnight with mild rotation at 37°C. After washing in water, gels were equilibrated in 20 mM Tris-Cl [pH 8.0] and incubated in 20 mM Tris-Cl [pH 8.0] containing 0.01 mg/ml Protease for 4-5 hrs. Gels were rinsed with water and equilibrated in de-stain solution (30% methanol, 7% acetic acid) for 20 min. Gels were stained for HA overnight with Alcian Blue (0.5% Alcian Blue in de-stain solution), then incubated in de-stain solution until clearings were evident. Gels were counterstained with Coomassie Blue (0.1% in de-stain solution) for 45 min to visualize any remaining protein. Zymograms were incubated in de-stain solution until clearings were evident.

2.23 Animals

Hyal1 +/- B6.129X1- *Hyal1*^{tm1Stn}/ Mmcd mice (N=7 generations of backcrossing on C57Bl/6J background) were purchased from the Mutant Mouse Regional Resource Centers (MMRRC: 000086-UCD, Davis, CA, USA) and mated to

establish a colony. All procedures were approved by the University of Manitoba Animal Protocol Management and Review Committee, in accordance with the Canadian Council on Animal Care guidelines for the care and use of animals.

2.24 Necropsy

Animals were euthanized at 3, 6, 12, or 20 months of age using CO_2 asphyxiation. Animals were weighed and examined for visual signs of abnormalities as well as joint masses. Upon necropsy, major organs and tissues including heart, liver, lungs, kidneys, fat, skeletal muscle, brain, testes, ovaries, seminal vesicles, uterus and skin were removed, weighed and distributed to fixatives and/or frozen in liquid N_2.

2.25 RNA purification

2.25.1 Total RNA

Tissues were crushed using a mortar and pestle on dry ice and added to 4 ml lysis solution (4M guanidinium thiocyanate, 25 mM sodium citrate, 0.1M β-mercaptoethanol, 0.5% sarkosyl). Tissues were completely homogenized using a Potter-elvehjem homogenizer. After homogenization, 400 µl of 2 M sodium acetate [pH 4.0], 4 ml of water saturated phenol and 0.8 ml of chloroform: isoamyl alcohol (49:1) was added and the mixture was incubated on ice for 15 min. Samples were centrifuged and the aqueous layer collected. One volume of isopropanol was added and RNA was precipitated at -20°C for 1 hr. The RNA pellet was collected by

centrifugation at 10,000 x g, resuspended in 1.2 ml of lysis buffer and precipitated using 2 volumes of ethanol for 1 hr at -20°C. RNA was washed three times with 70% ethanol and resuspended in 200-500 µl of H_20 depending on the pellet size.

For lung total RNA, tissues were crushed as described above and isolated using a GenElute Mammalian Total RNA isolation kit (Sigma-Aldrich). Briefly, lung tissue was homogenized in 500 µl of lysis solution (Sigma-Aldrich) containing β-mercaptoethanol (Sigma-Aldrich) and completely homogenized using a Potter-elvehjem homogenizer. The tissue lysates were transferred to a filtration column, centrifuged for 2 min and the lysate was collected. An equal volume of 70 % ethanol was added, samples were mixed and applied to a binding column prior to centrifugation for 15 s. After the flow through was discarded, 500 µl of wash solution 1 (Sigma-Aldrich) was added to the column and the column was centrifuged for 15 s. The column was transferred to a new tube, 500 µl of wash solution 2 was added and the column was centrifuged for 15s. After washing a second time with 500 µl of wash solution 2, the column was centrifuged for 2 min to dry any remaining ethanol. The total RNA was eluted with 50 µl of elution buffer (Sigma-Aldrich) and centrifuged for 1 min. The purity and quantity of lung total RNA was assessed as described in section 2.4.

2.25.2 mRNA

Liver, testes and kidney mRNA was isolated from total RNA using the Oligotex suspension mix (Qiagen Inc.) using a modified protocol according to the manufacturer's instructions. Depending on tissue origin, starting quantities of total

RNA ranged from 175 – 1000 µg. RNA was mixed with ODB buffer (Qiagen Inc.), OL1 buffer (Qiagen Inc.) and Oligotex (Qiagen Inc.) at varying amounts dependent on the starting RNA concentration and amount of total RNA used. RNA was incubated at 70°C for 3 min to denature RNA structures and was incubated with Oligotex beads for 10 min at room temperature. The RNA/Oligotex complexes were applied to a filter column and washed with OW1 and OW2 buffers (Qiagen Inc.). RNA was eluted from Oligotex beads using 50 µl of OEB buffer (Qiagen Inc.) pre-warmed at 70°C and quantitated as described in section 2.4.

2.26 Northern blotting

2.26.1 Transfer

RNA samples were transferred to a BrightStar®-Plus positively charged nylon membrane (Ambion Inc.) by an alkaline downward transfer method[152] according to the manufacturer's instructions. The membrane and gel were sandwiched between both wet and dry Whatmann paper, including a bridge of Whatmann paper pre-wet with transfer buffer (10 mM NaCl, 1M NaOH) that connected the transfer set-up and transfer buffer reservoir. RNA transfer was allowed to proceed for 4 hrs at room temperature. The blot was rinsed briefly in RNase-free water and UV cross-linked according to manufacturer's recommendations. The RNA blot was stained with methylene blue stain (0.0025% methylene blue, 1mM Tris-acetate [pH 7.4], 0.1 M EDTA) and RNA bands were visualized by rinsing with water.

2.26.2 Preparation of DNA probes

The *Hyal1* probe was produced by digestion of a *Hyal1* mouse EST clone (NIA H4011E09) with KpnI and XhoI to generate a 1.1 kb DNA fragment. The *Hyal2* probe was produced by digestion of a *Hyal2* mouse EST clone (IMAGE: 3411330) with EcoRV and PflFI to produce a 1.4 kb DNA fragment. The mouse *Fus2* probe was generated by digestion of pHLS1 with HincII and SalI to generate a 624 bp DNA fragment. The Gapdh probe was generated by restriction digestion of a *Gapdh* mouse EST clone (IMAGE: 3044486) with SfiI and AflIIII to generate an 850 bp DNA fragment. All DNA probes were separated by gel electrophoresis, purified by gel extraction and quantitated. Random primer labeling was performed as described in section 2.17.2 and free nucleotides were removed using NICK Columns (Pharmacia Biotech).

2.26.3 Hybridization

Blots were pre-hybridized overnight in Expresshyb (BD Biosciences) at 68°C to block non-specific binding of DNA probes. The blots were incubated in fresh hybridization solution containing heat denatured ^{32}P-labelled DNA probe (2 x 10^6 cpm/ml) and incubated overnight at 68°C. RNA blots were then washed as described in section 2.17.3

2.27 Real-time PCR

A starting quantity of 500 ng of mRNA or 1-2 μg of total RNA was reverse transcribed using a random hexamer primer extension with Superscript III reverse transcriptase (Invitrogen). Taqman Gene Expression Assays (Applied Biosystems, Foster, CA, USA) for mouse *Hyal1* (Mm00476206_m1), *Hyal2* (Mm00477731_m1), *Hyal3* (Mm00662097_m1), *Hyal4* (Mm 01165340_m1), *Hyal5* (Mm01165333_m1), *Spam1* (Mm00486329_m1), *HexB* (Mm00599880_m1) and a *HyalP1* custom assay (Primers: forward [gggaacccttctgtgttttggaaa], reverse [cccactggataaacatggattgct]; Probe[cctttgagcacacttcc]) or human *HYAL2* (Hs00186841_m1) and *HYAL3* (Hs00185910_m1) were performed in triplicate using 10, 25, 50 or 100 ng of cDNA. A mouse *Gapdh* (4352339E), mouse *mHprt* (Mm00446968_m1) or human *GAPDH* (4326317E) Taqman Gene Expression Assay (Applied Biosystems) was included in experiments to normalize for cDNA loading. All assays were performed using an Applied Biosystems 7300 Real-Time PCR system with standard cycling conditions (Initial denaturing steps: 50.0°C for 2 min; 95.0°C for 10 min; Cycling conditions (40x): 95°C for 15 s; 60.0°C for 1 min). The mRNA of +/+ animals or of a unaffected human control was used as a calibrator for relative quantitation[153]. Statistically significant results were determined using a Relative Expression Software Tool-384 program (REST-384) based on a pair-wise fixed random reallocation test[154].

2.28 Tissue fixation, processing, embedding and microtomy

2.28.1 Joints

The joints of animals were excised above the knee and fixed in periodate lysine paraformaldehyde fixative (0.1 M phosphate buffer, 4 % paraformaldehyde,

0.2 % sodium metaperiodate, 1.2 % lysine [pH 7.4]) for 1 hr at room temperature, then at 4°C overnight. Joints were washed three times with PBS and stored in 70 % ethanol until decalcification. Joints were decalcified overnight in Immunocal (American Mastertech) at 4°C or for 3 weeks at room temperature in 12 % EDTA/PBS with shaking. After processing and embedding, serial sections of 5 μm in thickness were cut using a microtome and stained with stained with 0.1 % Safranin O and 0.2 % Fast Green. Cells and nuclei were visualized by counterstaining with Gill's hematoxylin. Some sections were also stained with 0.1 % Toluidine blue and 1 % sodium chloride at pH 2.3. Toluidine blue and Safranin O staining were performed in the laboratory of Dr. John S. Mort (Shriner's Hospital for Children, Montreal QC)

2.28.2 Tissues

Tissues were collected, trimmed and fixed in 4 % paraformaldehyde in PBS overnight at 4°C. Skin samples for HA analysis were collected, trimmed and fixed for 2 days at room temperature in 4 % paraformaldehyde containing 0.5 % hexadecylpyridinium chloride monohydrate (CPC). Tissues were washed with PBS and stored in 70 % ethanol until processing. Processing was performed using 50 % ethanol, 70 % ethanol, 95 % ethanol, 4 changes of 100 % ethanol and 3 changes of xylene prior to paraffin wax infiltration. Cross sections of tissues were cut at 5 or 6 μm using a Leica RM2245 microtome.

2.28.3 Electron Microscopy (EM)

Tissues were collected, trimmed to 1-2 mm and placed in fixative (2 % glutaraldehyde, 2 % paraformaldehyde, 10 mM calcium chloride, 100 mM sodium cacodylate, 0.15 % Ruthenium Red, [pH 7.2]) at 4°C until processing within a week. Tissues were washed in EM wash buffer (10 mM calcium chloride, 100 mM sodium cacodylate, 0.7 % sucrose [pH 7.2]) and incubated in a post-fix solution (1% osmium tetroxide, 0.8 % potassium ferricyanide) for 1 hr. Tissues were washed with water, stained overnight in non-buffered 2 % uranyl acetate, dehydrated in acetone and embedded in Epon. Slow hardening of the Epon mixture was performed by 1 day incubations at room temperature, 45°C and 60°C. Thick sections of 0.5 μm and straw gold sections were cut by the University of Manitoba Histology Core Facility. Thick EM sections were stained with toluidine blue to determine histological appearance and architecture prior to EM analysis.

2.29 GAG quantitation

2.29.1 Serum HA

Blood was collected by cardiac puncture and allowed to clot at room temperature. Serum was separated by centrifugation for 15 min at room temperature, collected and stored at -80°C until use. Serum HA levels were quantitated by assaying 5 μl of serum, in duplicate, using a sandwich ELISA HA Test plate (Corgenix Inc.) according to the manufacturer's protocol. Serum HA concentrations were estimated by comparison to an HA standard curve generated using a four parameter linear regression.

2.29.2 Tissue GAG and/or HA content

Tissues were crushed on dry ice and lyophilized using a ThermoSavant Supermodulyo Freeze Dryer until completely dry. GAG analysis was performed in collaboration with Dr. S. Byers (Women's and Children's Hospital, North Adelaide, Australia). GAGs were extracted using 6 M urea, 0.05 M sodium acetate, 0.1 M EDTA, 0.1 M aminocaproic acid (pH 6.5) for 2 days at 4°C. After centrifugation, extracts were applied to a Q-Sepharose column equilibrated with 50 mM sodium acetate, 10 M formamide (pH 6.0) and GAGs were eluted using 50 mM sodium acetate, 10 M formamide (pH 6.0) and 4 M sodium chloride. Fractions were assayed for uronic acid content using a modified uronic acid assay[155]. Calculated GAG content was normalized to tissue wet weight.

For skin GAG quantitation, dorsal and knee skin was collected from each animal for fluorescence assisted carbohydrate electrophoresis (FACE). The purification of GAGs, 2-aminoacridone labeling and quantitation using known disaccharide standards were performed as previously described[156]. Briefly, approximately 10 mg of tissue was digested overnight in ammonium acetate (100 mM; pH 7.3) containing 50 μg/mg dry tissue of Proteinase K at 60°C. The proteinase K was inactivated by heating samples at 100°C for 5 min and undigested material was removed by centrifugation at 10,000 x g for 15 min. GAGs were purified by applying the samples to MicroCon YM3 cartridges, centrifugation at 11,000 x g for 75 min and elution into water. Approximately 0.6 μg of GAGs were used and diluted with 100 mM of ammonium acetate (pH 7.3) to obtain a final concentration of 88 mM ammonium acetate. GAGs were digested overnight with 0.5 mU/ml *Streptococcus*

dysgalactiae hyaluronidase (Associates of Cape Cod Inc., East Falmouth, MS, USA) overnight at 37°C. Proteins and non-digested GAGs were precipitated with ice-cold ethanol for 3 hrs at -20°C and separated from disaccharides by centrifugation at 10,000 x g for 20 min at 4°C. The supernatant containing disaccharides was removed, dried using a Savant SpeedVac Plus vacuum concentrator and resuspended in 5µl 0.1 M 2-aminoacridone (Invitrogen Inc.; resuspended in dimethylsulfoxide: acetic acid [85:1]; Company) for fluorescent derivitization at room temperature for 15 min. After the incubation, 5 µl of 0.1 M sodium cyanoborohydride solution was added to the labeled disaccharides and incubated overnight at 37°C. Disaccharide standards (Associates of Cape Cod Inc.) were also derivitized as described above. Samples were mixed with 30 µl of 25 % glycerol and separated by gel electrophoresis.

Labelled disaccharides were run according to previous procedures[157], except the stacking gel contained 0.36 M Tris-HCl (pH 6.8). Samples were separated on 25 % resolving gels (25 % acrylamide, 3.75 % bisacrylamide, 0.375 M Tris-HCl [pH8.8]). The resolving gels were cast and poured as described in section 2.20. Stacking gels (5 % acrylamide, 1.5 % bisacrylamide, 0.36 M Tris-HCl [pH 6.8]) were allowed to polymerize for 20 min prior to electrophoresis. Samples were loaded on the polyacrylamide gel and separated by electrophoresis in running buffer (0.1 M boric acid, 0.1 M glycine, 0.l25 M Tris [pH 8.3]) at 4°C with 400V. Fluorescent signals were quantitated using a cooled CCD camera attached to a Fluor S-Max imager with Quantity One software.

2.30 Staining

2.30.1 Haematoxylin and eosin

Slides containing tissue sections were deparaffinised by incubation for 5 min in 2 changes of xylene. Rehydration of tissue sections was performed by 5 min incubations in two changes of 100 % ethanol and 95 % ethanol, followed by sequential 3 min incubations in 70 % ethanol and water. Tissue sections were stained in Mayer's Haematoxylin solution for 5 min and were washed in running tap water for 15 min or until nuclei turned blue in color. Slides were transferred to 80 % ethanol for 1 min prior to counterstaining in Eosin Y for 30 sec. The Eosin Y stain was cleared from tissue sections using a 3 min incubation in 70 % ethanol. Dehydration of tissue sections was performed by sequential incubations for 5 min in two changes of 95 % ethanol, 100 % ethanol and xylene prior to mounting the coverslip with Permount.

2.30.2 Hyaluronic acid binding protein (HABP) staining

Joint sections were rehydrated to H_20 and treated with 0.25 % trypsin-EDTA for 15 min at 37°C (Invitrogen). After washing twice for 5 min in PBS, sections were quenched for endogenous peroxidases in 3 % hydrogen peroxide in PBS (pH 7.4) at room temperature for 30 min with shaking. After washing three times for 5 min in PBS, sections were blocked in 10 % fetal calf serum in TBST (pH 7.4) for 30 min at room temperature. Endogenous biotin binding sites were blocked using an Avidin-Biotin blocking kit (Vector Laboratories, Burlingame, CA) according to the manufacturer's protocol. Joint sections were incubated overnight in biotinylated

HABP (3.3 µg/ml) prepared in TBST containing 10 % fetal calf serum (Associates of Cape Cod Inc.). After washing sections three times for 5 min in TBST, sections were incubated for 1 hr with avidin, biotin and horse radish peroxidase enzyme complexes at room temperature according to the instructions of the Vectastain ABC detection system (Vector Laboratories). Sections were washed twice in TBST for 5 min at room temperature and incubated with DAB substrate (Vector Laboratories) for 10 min at room temperature. After washing sections for 5 min in H_2O at room temperature, sections were stained with 0.1% Nuclear Fast Red in 5 % aluminum sulfate for 3 ½ min, dehydrated and mounted. Control sections were incubated overnight in 50 U/ml of hyaluronate lyase from *Streptomyces hyalurolyticus* (Sigma-Aldrich) prior to quenching. Skin HA staining was performed as described above with a few modifications. The trypsin treatment and biotin blocking were not performed on the skin samples. Instead upon rehydration, slides were incubated for 3 hours in 1.3 M potassium chloride to compete for CPC binding prior to proceeding with the HABP staining.

2.31 Hexosaminidase activity

Tissue extracts were prepared in PBS containing 0.1 % Triton X-100 with protease inhibitors. Protein concentrations were determined as described in section 2.19.2. Samples were diluted in 0.01M phosphate-citrate buffer (10 mM Na_2HPO_4, 6 mM citrate, [pH 4.4]) containing 0.6% bovine serum albumin until reaching a pH of 4.4. A substrate stock solution containing 2.5 mM 4-methylumbelliferyl-*N*-acetyl-β-D-glucosaminide in 0.01M phosphate-citrate buffer was made. A 1:1 ratio (10 µl

each) of diluted tissue lysates and substrate stock solution was incubated for 30 min at 37°C in duplicate. Enzymatic reactions were stopped using 1.0 ml of glycine-carbonate buffer (0.17 M glycine, 0.17 M Na_2CO_3, [pH 9.8]). Fluorescence readings were obtained at an excitation wavelength of 360 nm and emission wavelength of 415 nm. Lysate buffer diluted in the same proportion as samples was included as a negative control to blank fluorometric readings. The nmol of fluorescent product was determined in comparison to a standard curve consisting of 20, 50, 100, 200 and 400 nM methylumbelliferone (7-hydroxy-4-methylcoumarin). Total activity was determined by the formula:

Total activity (nmol/hr/mg) = [(activity x dilution factor)/protein concentration] x 2

2.32 Statistical analysis

The *Hyal1* genotype distribution was compared to expected Mendelian ratios by Chi-Square analysis using GraphPad QuickCalcs and all other statistical analyses were performed using NCSS software. Body weights were compared by one-way analysis of variance, whereas serum HA concentrations and tissue GAG content were compared by multiple analysis of variance (2 or 3-way analysis of variance). Organ weights were compared between gender and genotypes by analysis of covariance (3-way analysis of variance) with body weight defined as the covariant. Total hexosaminidase activity of liver lysates from mice was compared between gender and genotypes by multiple analysis of variance (2-way analysis of variance). Organ weights of 20 month male mice were analyzed by analysis of variance with body weight defined as a covariant. Statistical significance was defined as a level of

probability less than 0.05 ($P<0.05$). Any results determined to be statistically significant by analysis of covariance or multiple analysis of variance was examined using a Tukey's post-hoc analysis.

Chapter 3: Generation and characterization of *Hyal1* +/- and -/- mouse embryonic stem cell lines

Acknowledgements:

The mouse PAC clone 452D10 was obtained from the MRC Genome Resource Facility (Toronto, ON). Brandy Wicklow and Tim Salo generated the pHLS1 and pHL3 sub-clones respectively. Tamara Dyck aided in the design of the p*Hyal1* Neo/TK targeting construct and screening strategy. Niki Boyko aided in the generation of the *Hyal1* -/- ES cell line. Tim Salo performed western blot analysis of embryonic stem cell lysates and Rick Hemming performed the zymographic analysis of the embryonic stem cell lysates and media. Special thanks to Marina Gertsenstein and Andras Nagy (Samuel Lunenfeld Research Institute, Toronto, ON) and Yanglong Mou, Ludger Klewes and Geoff Hicks (Cancercare Manitoba, Winnipeg, MB) for demonstration and direction in embryonic stem cell culturing and knockout methodologies.

3.1 Introduction

Murine models have been used to uncover key clinical characteristics of disease, identify the physiological role of a protein and understand pathogenic mechanisms of disease progression. Murine models have served as tools for testing therapeutic interventions for MPS II, MPS IIIA, MPS IIIB and many others[143, 158-160]. Since only one MPS IX patient has been described to date, it is likely that patients are either being misdiagnosed or missed in clinics. Therefore, characterization of a mouse model can provide information on likely presenting symptoms, as well as be used to test possible therapeutic interventions. A mouse model of Hyal1 deficiency could also be used to determine cellular sites of Hyal1 function by the identification of HA accumulation.

As a starting point to generate a mouse model of MPS IX, examination and comparison of the human and mouse *HYAL1/Hyal1* gene structure, sequence and expression was necessary to determine if the mouse was a suitable system to study Hyal1 function. These studies have been performed previously and showed that the human and mouse *HYAL1/Hyal1* display 73% amino acid identity, as well as a similar chromosomal organization, gene structure and expression[100, 119]. However, multiple co-transcripts of *Hyal1* with downstream genes, *Fus2* and *Hyal3* are found only in the mouse system[100]. Although the biological significance of these co-transcripts is unknown, *in vitro* transcription and translation analysis suggested that only Hyal1 was produced from these transcripts[100]. Thus it is likely that any alterations in these transcripts produced by gene targeting will only affect the function of Hyal1. The similarities in tissue expression, gene structure and sequence between

mouse and human *HYAL1/Hyal1* suggested that the mouse may be a suitable system to examine the physiological functions of Hyal1.

It was at this point that I entered the lab and chose a project that required the generation and characterization of a Hyal1 deficient mouse model. Methods to generate a targeted disruption in a gene of interest, commonly referred to as gene targeting, have been used since 1981 and are now well established[161, 162]. Gene targeting relies on the genetic principal of homologous recombination between two sequences with high similarity to generate an ES cell line containing an insertion designed to disrupt gene function. To accomplish this, an exogenous targeting construct containing homologous sequence to an endogenous locus, in our case *Hyal1*, is transfected into ES cells. Homologous recombination occurs between the targeting construct and endogenous sequence, resulting in the integration of the targeting construct sequence into the desired locus. While the frequency of homologous recombination between the targeting construct and an endogenous locus is low in mammalian cells (1 in 10^4 cells), the proper design of a targeting construct can facilitate the identification of correctly targeted recombination events[163]. Sequence homologous to the endogenous locus is incorporated into the targeting construct design and the length of this sequence is directly proportional to the frequency of recombination[164, 165]. The use of positive and negative selection markers can reduce the number of ES cell colonies screened, as well as disrupt gene function[163]. Additional markers to identify cell-specific or time-specific gene expression, such as β-D-galactosidase (LacZ) or green fluorescent protein (GFP), can be incorporated into the targeting constructs to allow for subsequent ease in the

examination of gene expression[166-168]. To generate a correctly targeted ES cell line, and utilize these tools for analysis, requires careful design of a targeting construct. ES cell lines carrying alleles with the desired mutation must be selected and the correct integration event confirmed prior to using the line for the production of mouse chimeras. Creating a targeted *Hyal1* cell line can be accomplished by generating a *Hyal1* targeting construct to be used and identifying ES cell lines that contain the desired incorporation that will ultimately disrupt enzyme function.

This chapter describes the design, construction and targeting efficiencies of two *Hyal1* targeting constructs, as well as the generation of a *Hyal1* -/- ES cell line that could be used for future studies. Using the p*Hyal1* Neo/TK constrcut, only one *Hyal1* +/- R1 ES cell line was identified in the screening of 260 ES cell lines. Therefore, we sought to improve the efficiency of *Hyal1* targeting by the design and construction of the p*Hyal1* β-geo construct. At the same time, we chose to generate *Hyal1* -/- ES cell lines to determine the effects of the construct integration on *Hyal1* RNA to provide useful information for future experimental studies. I will conclude the chapter with a short discussion of the difficulties in targeting the *Hyal1* locus and discuss considerations and/or alternative designs that could be developed to improve the targeting efficiency.

3.2 Results

3.2.1 Targeting construct design and generation

3.2.1.1 p*Hyal1* Neo/TK

As a starting point, a p*Hyal1* Neo/TK targeting construct was designed to interrupt the coding sequence of *Hyal1* with a positive selection marker. Upon integration, this construct should replace exon 2 of *Hyal1* (nucleotides 6485268 - 6486546, NT_039477.7, Mm9_3951737), along with the splice acceptor and donor sites, with a neomycin resistance cassette (Neo) driven by the constitutive phosphoglycerate kinase (PGK) promoter. This strategy was designed to promote skipping of the Neo cassette by the splicing complex to ensure that co-transcripts between *Hyal1* and downstream *Fus2* and *Hyal3* genes would remain intact. However since exon 2 would be replaced in the process, more than half of the coding region of Hyal1 would be deleted, including the aspartate tryptophan glutamate (DWE) that is the predicted active site of the enzyme[104]. The p*Hyal1* Neo/TK construct contained 3.8 kb and 3.4 kb of homology on the 5' and 3' arms respectively, along with a negative selection marker, thymidine kinase (TK), driven by a PGK promoter. Both positive and negative selection markers were incorporated into p*Hyal1* Neo/TK to enrich for ES cell lines that had undergone homologous recombination on both the 5' and 3' arms of the construct. A schematic of the p*Hyal1* Neo/TK targeting construct is displayed in Figure 6.

A screening strategy, also shown in Figure 6, was designed using EcoRV and PflFI restriction enzyme digests of genomic DNA and Southern analysis to identify positive ES cell clones that had undergone homologous recombination with the *Hyal1* locus. Two DNA probes (Figure 6, labeled a and c), external to the homologous arms of the targeting construct, were used to detect bands that displayed a shift in size due

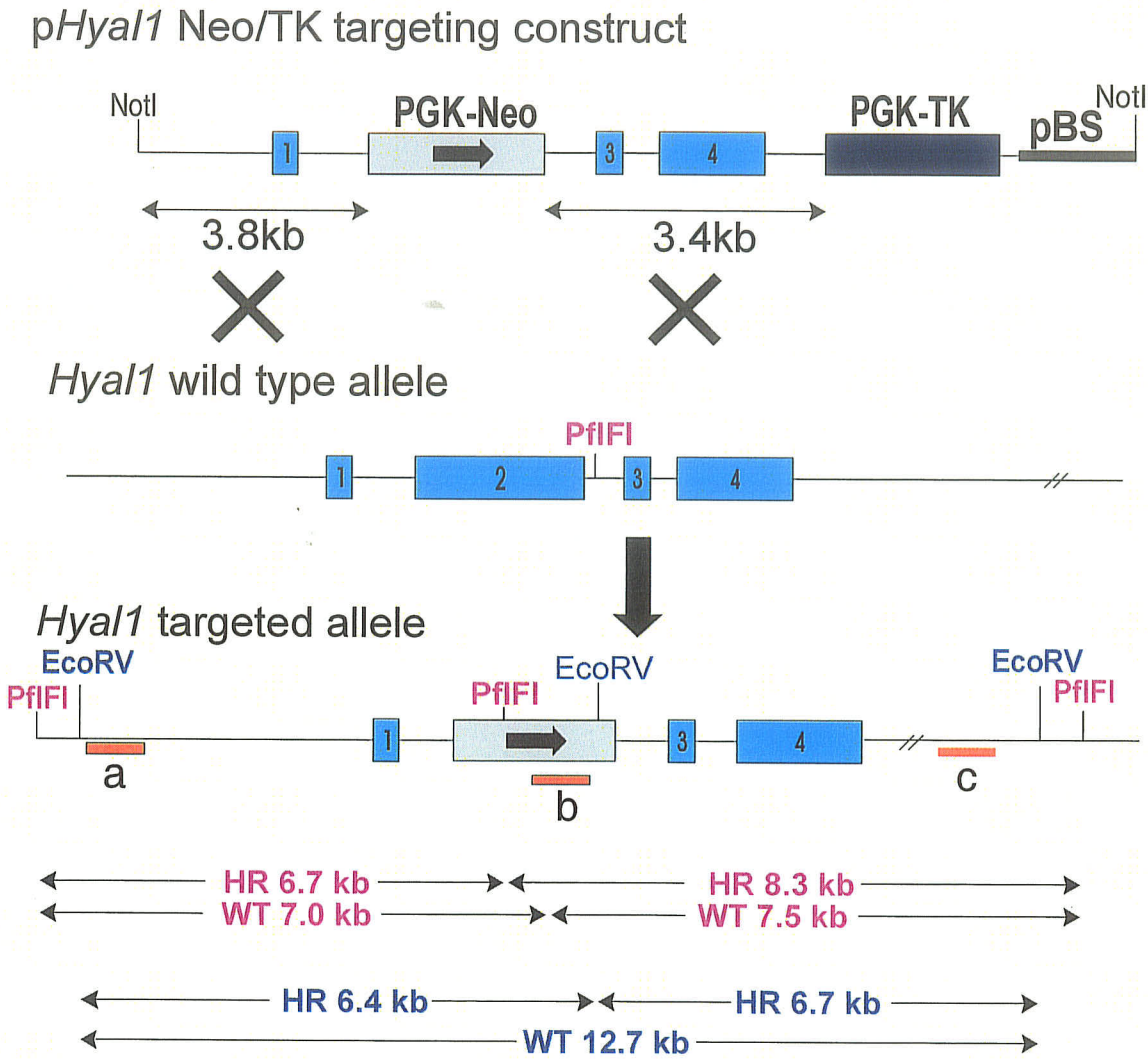

Figure 6: Schematic diagram of the p*Hyal1* Neo/TK targeting construct design and screening strategy.

Exons and resistance cassettes are denoted by squares, introns and intergenic sequences are represented by lines and the arrow inside of the grey box indicates the direction of transcription of the resistance cassette. The EcoRV and PflFI restriction enzymes were used with Southern analysis to detect the homologous recombinant (HR) or wild-type (WT) allele in G418 resistant ES cell lines using a 5' external (a), 3' external (c) or internal (b) probe. The integration of the Neo cassette is predicted to cause a shift of the detected band sizes due to the introduction of PflFI or EcoRV restriction sites. pBS indicates the pBluescript SK^+ plasmid vector backbone of the targeting construct. Neo denotes the neomycin resistance cassette, TK denotes the thymidine kinase cassette and PGK indicates the presence of the phosphoglycerate kinase promoter.

to the Neo integration. An internal Neo probe (Figure 6, labeled b) was also designed to identify ES cell clones containing a single incorporation of the resistance cassette into the mouse genome. The predicted size of the homologous recombinant (HR) and wild-type (WT) alleles, detected using both the EcoRV and PflFI restriction digests, is outlined in Figure 6.

Briefly, using an EcoRV restriction enzyme digestion, both the 5' external and 3' external probes should detect a 12.7 kb band representing the WT allele. Upon integration of the Neo cassette containing an EcoRV site, the 5' external probe should detect a 6.4 kb band and the 3' external probe should detect a 6.7 kb band from the HR allele. Using a PflFI screening enzyme, the 5' external probe would detect a 7.0 kb band with the WT allele; however a 6.7 kb band would be detected with the HR allele. Similarly the 3' external probe would also detect different sized DNA bands upon Neo integration. A 7.5 kb WT band and a 8.3 kb HR band would be detected with this probe. The internal Neo probe would detect the 6.7 kb band using the EcoRV restriction digest and an 8.3 kb band using the PflFI digest representing the HR allele, but no additional bands should be identified.

A 5 step cloning procedure, as outlined in Figure 7, was used to generate the p*Hyal1* Neo/TK targeting construct. Briefly, a *Hyal1* sub-clone, pHLS1 was restriction enzymes, NsiI and EcoRI, and blunt ends were generated to yield a 7.7 kb linearized plasmid vector that was re-ligated to form a pHLS1 modified plasmid. This step modified the plasmid to remove a HindIII site that interfered with the next cloning step. A 6.5 kb vector DNA fragment was produced by PflFI and HindIII

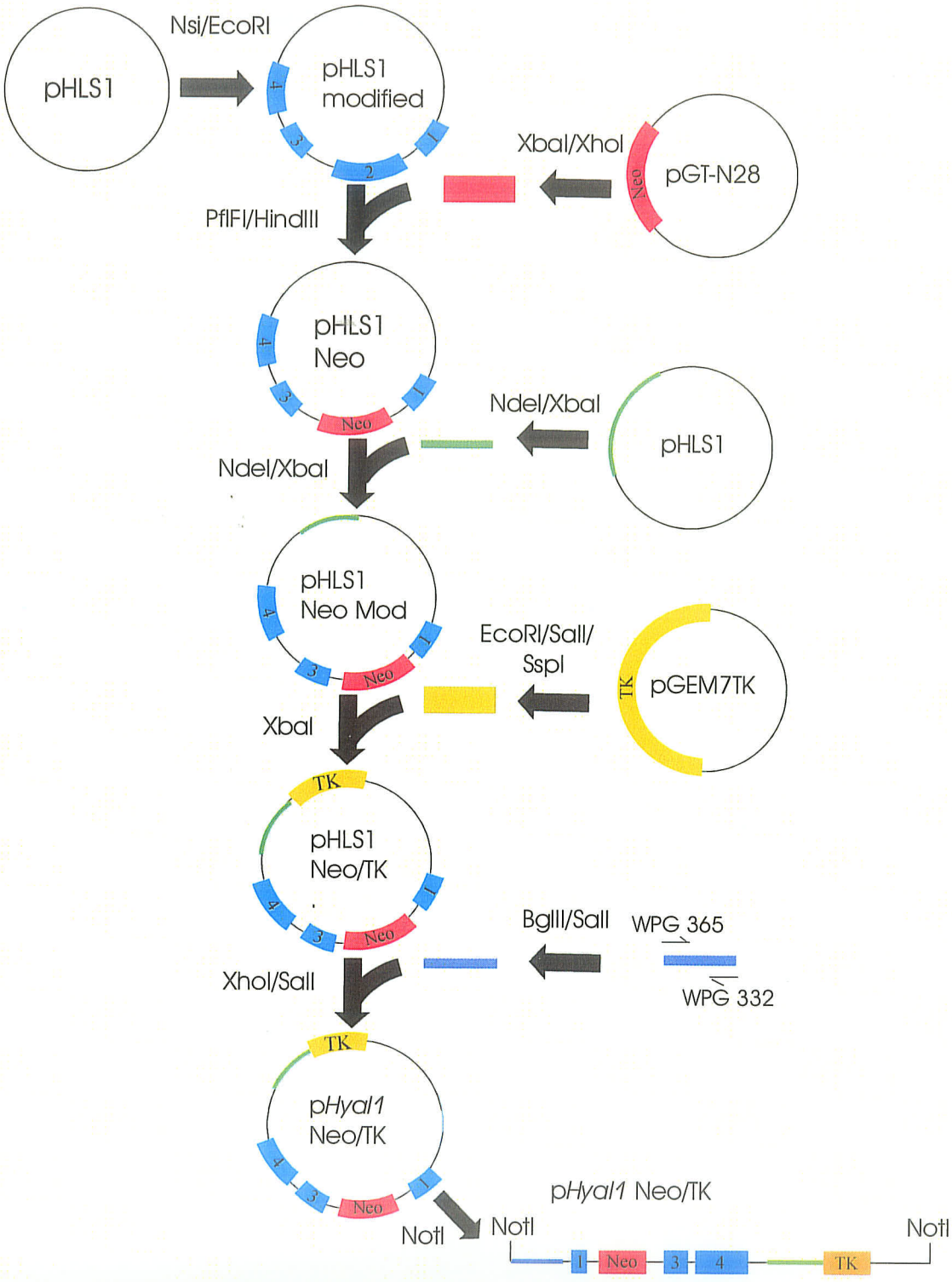

Figure 7: Schematic diagram of the p*Hyal1* Neo/TK cloning strategy.
Blue, red or yellow colored boxes denote exons or resistance cassettes. The green and dark blue lines denote extended 3' and 5' regions of homology respectively. Restriction enzymes used in generating insert or vector fragments are indicated above solid black arrows that represents either a restriction digest or restriction digest and ligation. Neo indicates the neomycin resistance cassette and TK denotes the thymidine kinase cassette.

restriction enzyme digestion of the pHLS1 modified plasmid. This vector fragment was blunt-end ligated to a 2.0 kb insert fragment containing the Neo coding region produced by XbaI and XhoI restriction enzyme digestion of a pGT-N28 plasmid. During this step, *Hyal1* exon 2 was removed from the pHLS1 modified plasmid and Neo was inserted to generate a pHLS1 Neo plasmid. A clone containing the Neo insert in the forward direction was selected for the 3rd cloning step.

The homology on the 3' end of the Hyal1 gene was extended by restriction enzyme digestion of the pHLS1 Neo and pHLS1 plasmid with NdeI and XbaI to generate 8.0 kb and 2.4 kb vector and insert DNA fragments respectively. Vector and insert DNA were ligated to produce a modified pHLS1 Neo (pHLS1 Neo Mod) plasmid. An insert DNA fragment containing a 3.0 kb PGK-TK negative selection marker was removed from a pGEM7TK plasmid using the enzymes EcoRI, SalI and SspI. The insert was blunt-end ligated to a 10.4 kb modified pHLS1 Neo (pHLS1 Neo Mod) vector produced by restriction enzyme digestion with XbaI. A clone, pHLS1 Neo/TK, containing the PGK-TK cassette in the forward orientation was selected and used for the final cloning step. PCR amplification was performed using forward and reverse primers (WPG 365; WPG 332) from a 452D10 PAC clone to increase the length of the 5' homologous arm of the targeting construct by 1.9 kb. The PCR product was TA cloned into a pCR2.1 vector, cut with BglII, the 5' overhang was filled-in and the DNA subsequently digested with SalI to remove the 1.9 kb insert containing the additional region of 5' homology. A 13.4 kb vector DNA fragment was produced by digestion of pHLS1 Neo/TK with XhoI. The 5' overhang was filled in and the plasmid DNA was subsequently digested with SalI for a blunt-sticky end

ligation with the insert described above. The resulting 15.3 kb plasmid, p*Hyal1* Neo/TK, was linearized with NotI and purified for use in *Hyal1* ES cell targeting.

3.2.1.2 p*Hyal1* β-geo targeting construct

The p*Hyal1* β-geo targeting construct was designed to be a modified knock-in targeting construct that contained two separate mutations. A 9 bp deletion at nucleotides 537-546 (NM_008317) was included in the construct to delete the coding region for a DWE amino acid sequence starting at amino acid 157 (NP_032343). The DWE amino acid sequence is the predicted active site of the hyaluronidase enzymes and *in vitro* mutagenesis of the coding sequence for D or E has been shown to result in severely reduced or undetectable PH-20 activity[25, 104]. A LacZ-Neo fusion cassette (β-geo), with an internal ribosome entry site, was used to enrich for correctly targeted cell lines by allowing expression of the resistance gene only under endogenously active promoters. The β-geo cassette would only be expressed when incorporated into a gene that was being actively transcribed in ES cells, thereby reducing the number of Neo resistant cell lines to screen. This β-geo cassette was situated downstream of the *Hyal1* stop codon to be incorporated into the altered splice variants of the *Hyal1* gene. A negative selection marker, diphtheria toxin A (DTA), was included in the design to identify cell lines that have undergone homologous recombination events on both arms of the targeting construct. A schematic of the design of the p*Hyal1* β-geo targeting construct is displayed in Figure 8.

A screening strategy was designed to identify correctly targeted ES cell lines using Southern analysis of EcoRV and SpeI digested genomic DNA (Figure 8). Two DNA probes (Figure 8, labeled a and c), external to the homologous arms of the

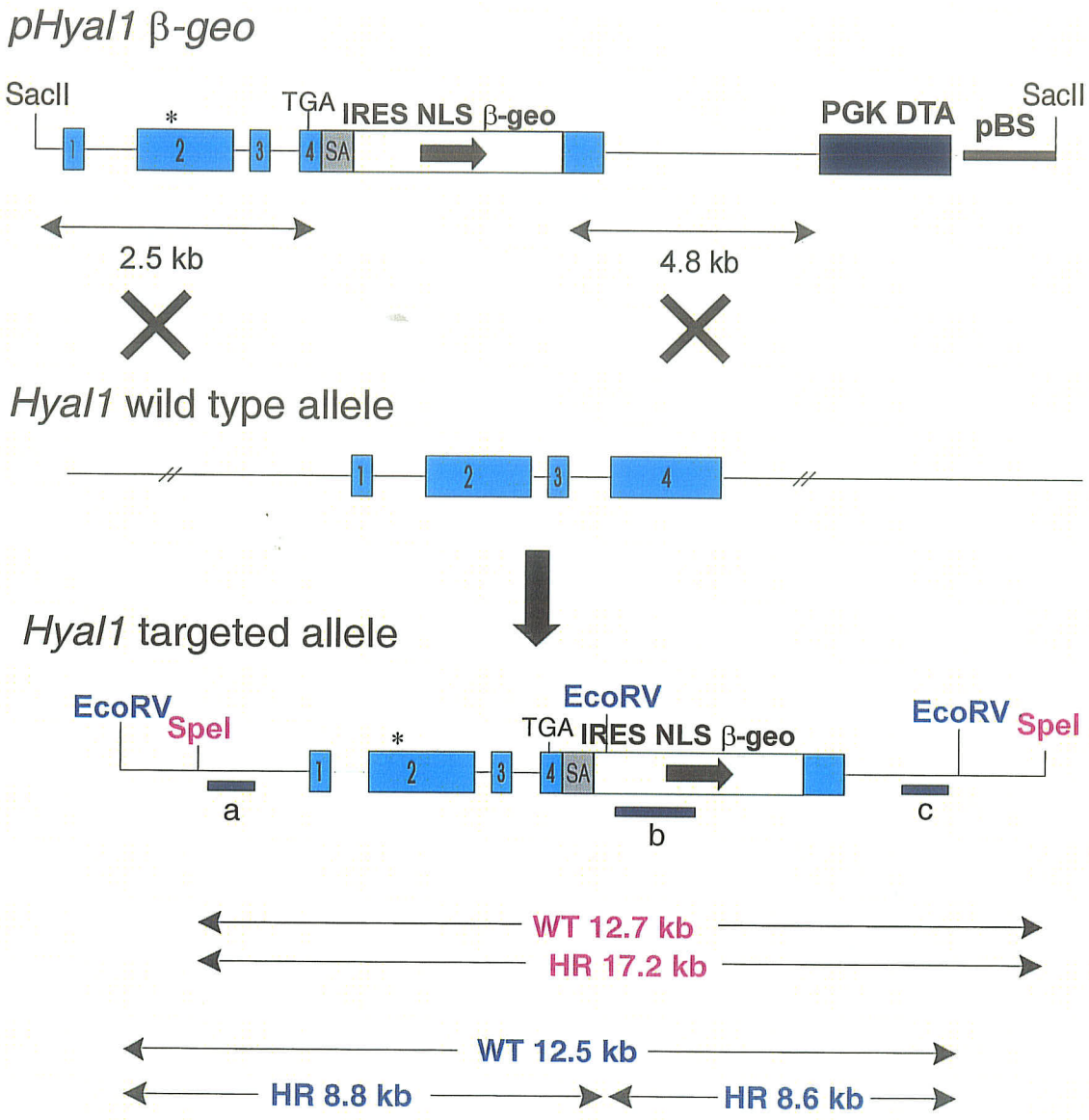

Figure 8: Schematic diagram of the p*Hyal1* β-geo targeting construct and screening strategy.

Exons and resistance cassettes are denoted as boxes, introns and intergenic regions are represented by lines and the arrow inside of the resistance cassette indicates the direction of transcription. The EcoRV and SpeI restriction enzymes were used with Southern analysis to detect homologous recombinant (HR) and wild-type (WT) alleles of G418 resistant clones using a 5' external (a), 3' external (c) and internal (b) probe. SA indicates the splice acceptor site, IRES indicates the internal ribosome entry site and NLS indicates the nuclear localization signal on the β-geo cassette. The * denotes a 9 bp deletion of a DWE amino acid sequence essential for Hyal1 function. pBS indicates the pBluescript SK^+ plasmid vector of the targeting construct.

targeting construct, and an internal LacZ probe (Figure 8, labeled b) were designed to detect genomic DNA fragments that would display a size shift by Neo integration into the *Hyal1* locus. Using an EcoRV genomic digest, the integration of an EcoRV site along with the β-geo cassette would detect a decrease from the expected 12.5 kb band of the WT allele to 8.8 kb and 8.6 kb bands of the HR allele using the 5' and 3' external probes respectively. However, Southern analysis on SpeI digested genomic DNA with the 5' external, 3' external and LacZ probe would detect a shift from the 12.7 kb band of the WT allele to 17.2 kb upon Neo integration with the HR allele. An overview of the screening strategy and the expected band sizes is shown in Figure 8.

The p*Hyal1* β-geo targeting construct was produced in a series of cloning steps shown in Figure 9. The first step added a nuclear localization signal (NLS) and an internal ribosome entry site (IRES) element to the β-geo plasmid. To accomplish this, the pSA β-geo plasmid was digested with HindIII, the ends were filled-in and the resulting fragment was digested with NdeI to produce a 4.3 kb vector DNA fragment containing a splice acceptor (SA) site, the terminal part of LacZ and a Neo resistance gene. The pNTR LacZ plasmid was digested with PstI, the ends were filled in and the fragment was digested with NdeI to produce a 3.5 kb insert fragment containing the IRES, NLS and part of the LacZ sequence. Vector and insert DNA fragments were ligated (labeled as (a), Figure 9) to generate a pSA IRES NLS β-geo plasmid containing a SA, IRES and NLS sequence directly upstream of the β-geo cassette. The LacZ junction formed by ligation was sequenced to ensure that the reading frame and coding region of the β-geo cassette were not altered during the cloning process. To incorporate a negative selection marker (DTA), the pPGKneolox2DTA plasmid

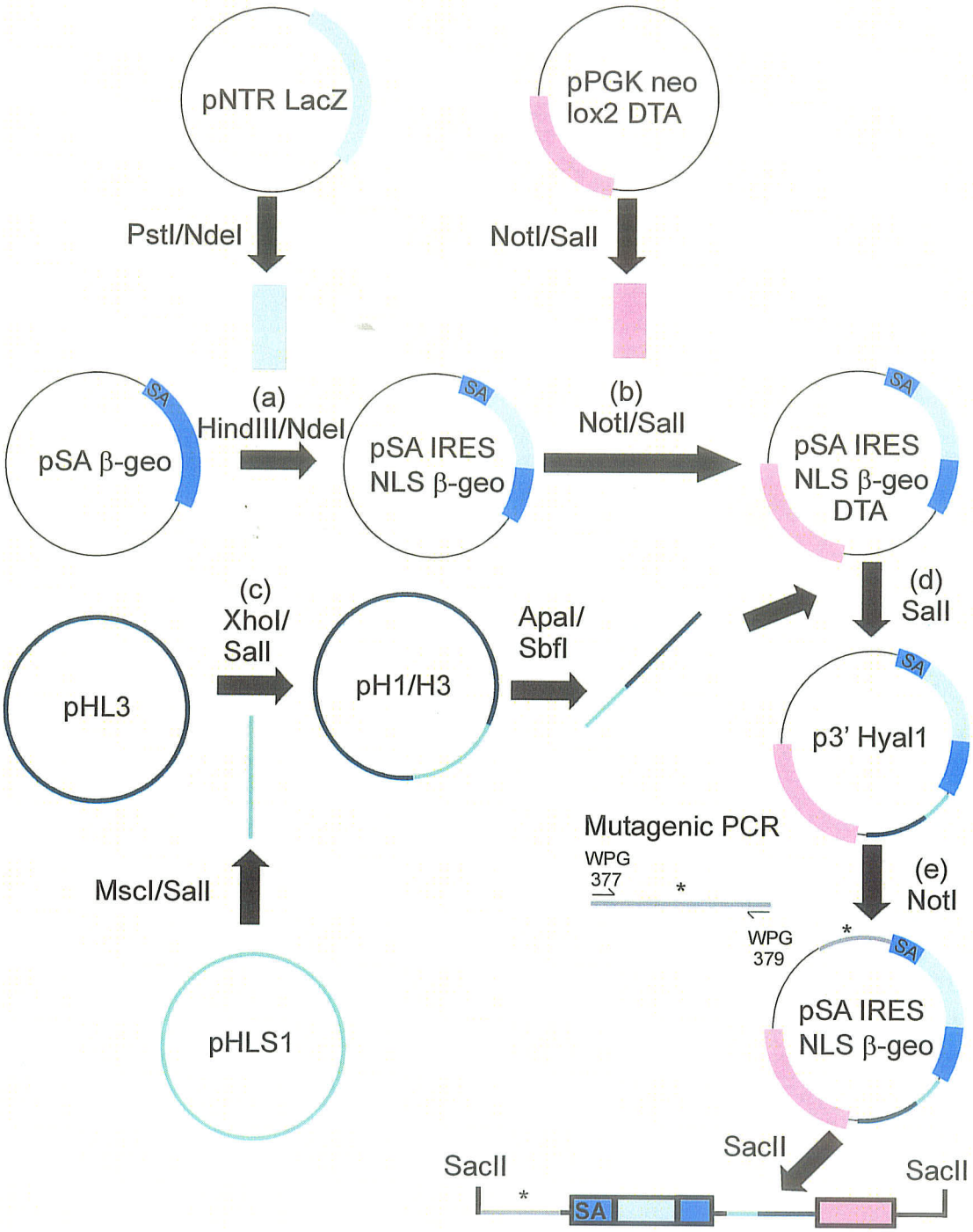

Figure 9: Schematic diagram of the p*Hyal1* β-geo cloning strategy.
Pink, light or dark purple boxes represent resistance cassettes in the constructs. The green line represents a 3' region of homology that was incorporated into the construct. Restriction enzymes used to prepare insert or vector fragments are denoted above the solid black arrows representing the restriction enzyme digest or restriction enzyme digest and ligation. The * denotes a 9 bp deletion incorporated into the final construct. SA indicates the splice acceptor site, IRES indicates the internal ribosome entry site and NLS indicates the nuclear localization signal on the β-geo cassette. The * denotes a 9 bp deletion of a DWE amino acid sequence essential for Hyal1 function.

was digested with NotI and SalI to generate a 4.5 kb insert DNA fragment. The insert was ligated (labeled as (b); Figure 9) to the 4.5 kb vector DNA fragment produced by restriction enzyme digestion of pSA IRES NLS β-geo plasmid with NotI and SalI. The resulting pSA IRES NLS β-geo DTA was used in subsequent cloning steps.

To extend the sequence homology to be used for the 3' arm of the targeting construct, the insert DNA sequence corresponding to 3.7 kb of downstream sequence from *Hyal1* was removed from the pHLS1 plasmid by MscI and SalI digestion. A pHL3 sub-clone was digested with XhoI, the 5' overhang was filled-in and subsequently digested with SalI to remove the 8.75 kb vector DNA fragment. This fragment was ligated (labeled as (c); Figure 9) to the insert described above to generate a pH1/H3 plasmid. A 5.3 kb insert sequence was removed from the pH1/H3 plasmid by restriction enzyme digestion with ApaI/SbfI and blunt-end ligated (labeled as (d); Figure 9) to a 9.0 kb pSA NLS IRES β-geo DTA vector DNA fragment generated by SalI. The resulting p3'Hyal1 plasmid, containing the insert in the forward orientation, was restriction enzyme digested with NotI to produce the vector fragment to be used in the final cloning step (labeled as (e); Figure 9).

To generate the 5' homologous arm containing the 9 bp deletion, a mutagenic overlap extension PCR[169] was performed using the 452D10 PAC clone as template. Complementary mutagenic primers (WPG 376, WPG378) were designed over the 9 bp deletion site with approximately 14 bp following the deletion. WPG 377 and WPG 379 primers were used in combination with the mutagenic primers to PCR amplify the homologous sequence as two overlapping DNA fragments representing the 5' and 3' ends of the 5' homologous arm respectively. The two overlapping fragments were

purified and used as the template for a second PCR reaction using the external primers, WPG 377 and WPG 379, to generate one full length PCR product of 2.5 kb from the two smaller PCR products. The PCR product was TA cloned into a pCR2.1 vector and sequenced to ensure the deletion of the 9 bp. The resulting TA clone was digested with EcoRI to remove the insert containing the 5' homologous DNA sequence, which was blunt-end ligated (labeled as (e); Figure 9) to the NotI linearized p3'Hyal1 vector. The resulting 16.3 kb p*Hyal1* β-geo clone was selected in the forward orientation, linearized with SacII and purified for use in *Hyal1* ES cell targeting.

3.2.2 ES cell targeting and confirmation

The *Hyal1* targeting constructs, p*Hyal1* Neo/TK and p*Hyal1* β-geo, were introduced through electroporation into an R1 or D3H ES cell line. After positive and negative selection, drug resistant colonies were picked and expanded for screening. In total, 672 and 58 resistant colonies were isolated after electroporation of the p*Hyal1* Neo/TK and p*Hyal1* β-geo targeting constructs respectively (Table 5). Using an EcoRV restriction digest of genomic DNA from potential *Hyal1* targeted ES cells, along with Southern analysis using either the 5' or 3' external DNA probes, a total of 299 drug resistant colonies were screened. From these resistant colonies, only 1 cell line that had undergone correct homologous recombination events between the p*Hyal1* Neo/TK construct and the endogenous *Hyal1* locus was identified.

Table 5: Number of G418 resistant, screened and *Hyal1* targeted ES cell lines.

Targeting construct	Experiment (#)	G418 Resistant Colonies isolated	Number of Colonies Screened	Number of *Hyal1* targeted cell lines
p*Hyal1* Neo/TK	1	288	93	1
	2 and 3	384	167	0
p*Hyal1* β-geo	1	58	39	0
Total	4	730	299	1

To ensure the Neo resistance cassette was correctly incorporated and that no additional alterations of the *Hyal1* gene occurred in the identified ES cell line, Southern analysis of genomic DNA digested with EcoRV or PflFI was performed with a Neo (internal), 5' external and 3' external probe (Figure 10A-D). Southern analysis of genomic DNA digested with EcoRV using a 5' external probe (Figure 10B), detected a 12.7 kb band representing the WT allele and a 6.4 kb band expected from the HR allele. The 3'external probe (Figure 10C) also detected the 12.7 kb band from the WT allele and a 6.7 kb band from the HR allele suggesting that Neo had successfully integrated into the *Hyal1* gene.

As a secondary confirmation, Southern blot analysis was performed as described above using PflFI digested genomic DNA. Southern hybridization using the 5' external probe (Figure 10B) detected a 7.0 kb band from the WT allele and a 6.7 kb band from the HR allele. Southern hybridization was also performed using a 3' external probe (Figure 10C) which detected a 7.5 kb band from the WT allele and an

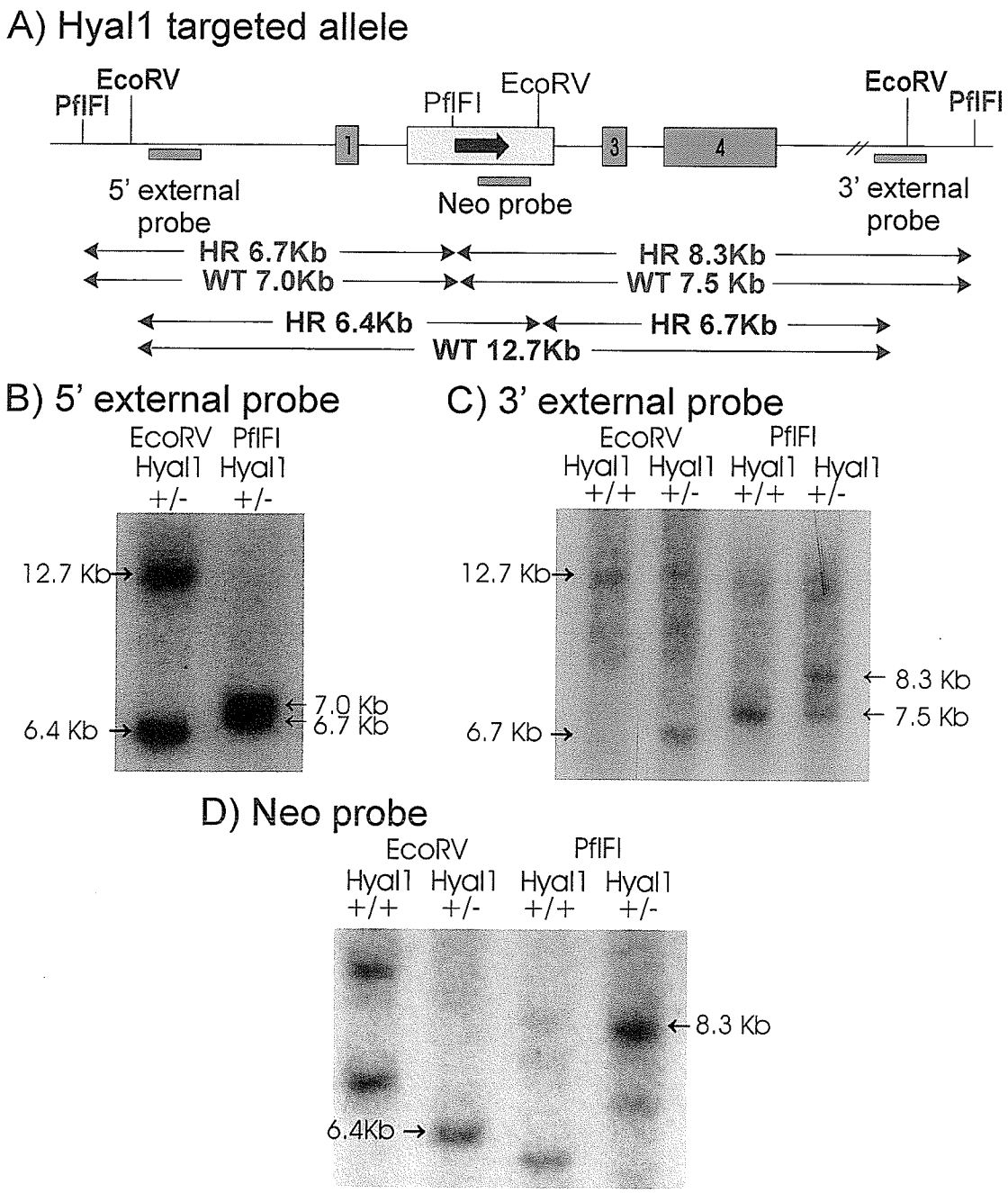

Figure 10: Southern analysis of a *Hyal1* +/- ES cell line.
A diagrammatic representation of the screening enzymes and expected sizes of the homologous recombinant (HR) and wild-type (WT) alleles are displayed in A). Exons are shown as blue boxes, while the Neo resistance cassette is indicated by the grey box. Introns and intergenic regions are represented as lines and the arrow inside the Neo resistance cassette indicates the direction of transcription. Southern analysis of a putative *Hyal1* +/- ES cell line using a 5' external (B), 3' external (C) or internal Neo (D) probe detected the expected band sizes for both the HR and WT alleles with EcoRV and PflFI digests confirmed the correct integration of Neo into *Hyal1*. The *Hyal1* +/+ ES cell line, shown in (C) and (D), was another putatively positive ES cell line identified from the initial screening and was later determined to be incorrectly targeted.

8.3 kb band from the HR allele. An internal Neo probe was used in Southern analysis of EcoRV and PflFI digested genomic DNA from the *Hyal1* +/- ES cell line, along with another G418 resistant colony, to ensure that Neo was only integrated into *Hyal1* (Figure 10D). This analysis detected the expected 6.4 kb and 8.3 kb bands from the HR allele by EcoRV and PflFI digestion respectively. This indicated that the only Neo integration present in the cell line was within *Hyal1*.

3.2.3 Generation of *Hyal1* -/- ES cell line

Hyal1, although not highly expressed, is found in most tissues and commonly used cell lines. Therefore, we chose to generate a *Hyal1* targeted (-/-) ES cell line to be used as a tool to investigate the function of other hyaluronidases. In addition, characterizing the -/- ES cell line would give us an indication of the level of deficiency that would be produced in a mouse model due to the Neo incorporation. After selection of the *Hyal1* +/- ES cell line in high G418 concentrations, resistant colonies were picked and expanded. Genomic DNA was isolated from 18 of these cell lines were screened by Southern blot analysis using an EcoRV restriction enzyme digest and the 3' external DNA probe (Figure 11A, 11B). Nine *Hyal1* -/- ES cell lines were identified based on the presence of only the 6.7 kb band from the HR allele (Figure 11B). To ensure no additional alterations in the *Hyal1* gene region occurred, six of these cell lines were analyzed by Southern blotting using the 5' external DNA probe (Figure 11C). The analysis confirmed the presence of only the 6.4 kb band corresponding to the HR allele in 5 ES cell lines, while the sixth colony appeared to

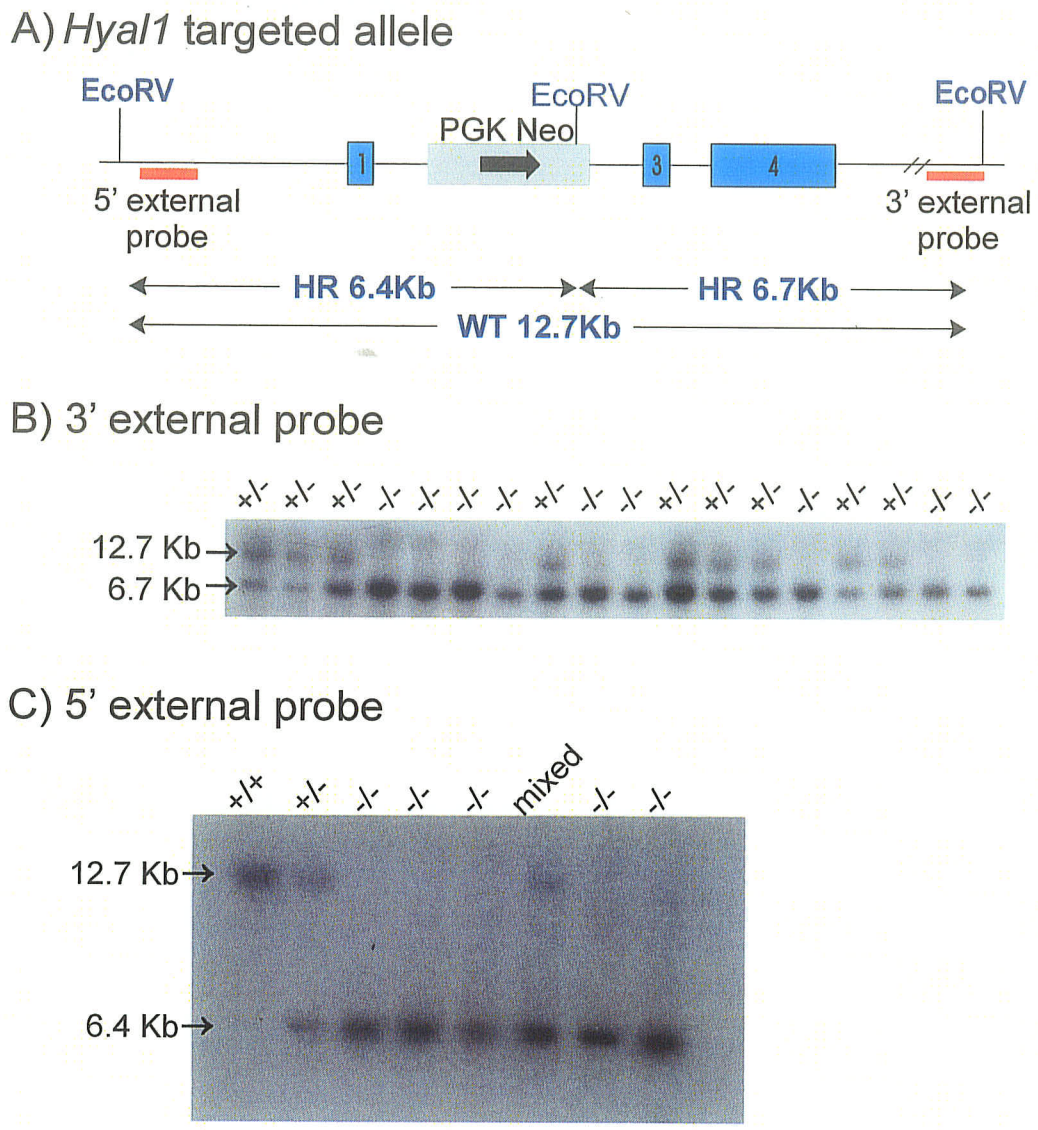

Figure 11: Southern analysis of *Hyal1* -/- ES cell lines.
A diagrammatic representation of the screening strategy and expected band sizes used for confirming the genotype of *Hyal1* -/- ES cell lines is shown in A). The boxes denote *Hyal1* exons or the Neo resistance cassette, the lines represent introns or intergenic sequence and the arrow inside of Neo indicates the direction of transcription. The EcoRV digested genomic DNA was screened using Southern analysis with 5'and 3' external probes to detect the homologous recombinant (HR) and wild-type (WT) alleles. Southern analysis using the 3' external probe displayed in B) detected ES cell lines containing either both the HR (6.7 kb) and WT (12.7 kb) alleles or containing only the band representing the HR allele. Southern analysis using the 5' external probe displayed in C) detected ES cell lines containing either WT (12.7 kb), HR (6.4 kb) or both HR and WT alleles. Nine -/- ES cell lines were identified in B) and 5 of these were verified using the 5' external probe in C).

be mixed (Figure 11C). Since 5 -/- ES cell lines were enough for our purposes, we did not screen the remaining 3 putatively positive ES cell lines.

3.2.4 Characterization of a *Hyal1* -/- ES cell line

To characterize the effects of the mutation on the *Hyal1* RNA transcripts, RT-PCR analysis of total RNA isolated from the *Hyal1* +/- and *Hyal1* -/- ES cell lines was used with two separate sets of primers. A primer set crossing the exon 3/exon 4 boundary (WPG 198/199) detected a residual transcript of the predicted 160 bp size in *Hyal1* -/- ES cells (Figure 12A). Interestingly, an additional product of 300 bp was also identified in +/+, +/- and -/- ES cells lines despite numerous attempts to increase PCR stringency. The transcript size did not correspond to the previously characterized alternative transcripts[100], and was found in all cell lines examined. This 360 bp PCR product was also found in mouse liver RNA (Figure 12A), thus the identified RNA species may represent an additional uncharacterized alternatively spliced transcript. The expected 900 bp PCR product was detected in cDNA from the *Hyal1* +/+ and *Hyal1* +/- ES cell lines, but not from the *Hyal1* -/- cell line (Figure 12B) using a forward primer to the segment of exon 2 that was replaced by the Neo cassette and a reverse exon 4 primer (WPG 182/198).

RT-PCR analysis suggested that Hyal1 transcripts were still present from the exon 2 replacement. However, transcripts either skip exon 2 or contain the Neomycin resistance cassette and are therefore unlikely to be functional. To show this, western blot analysis of lysates from *Hyal1* +/+ and *Hyal1* -/- ES cell lines was performed. A 55 kDa protein band corresponding to mouse Hyal1 was identified in the +/+ ES cell

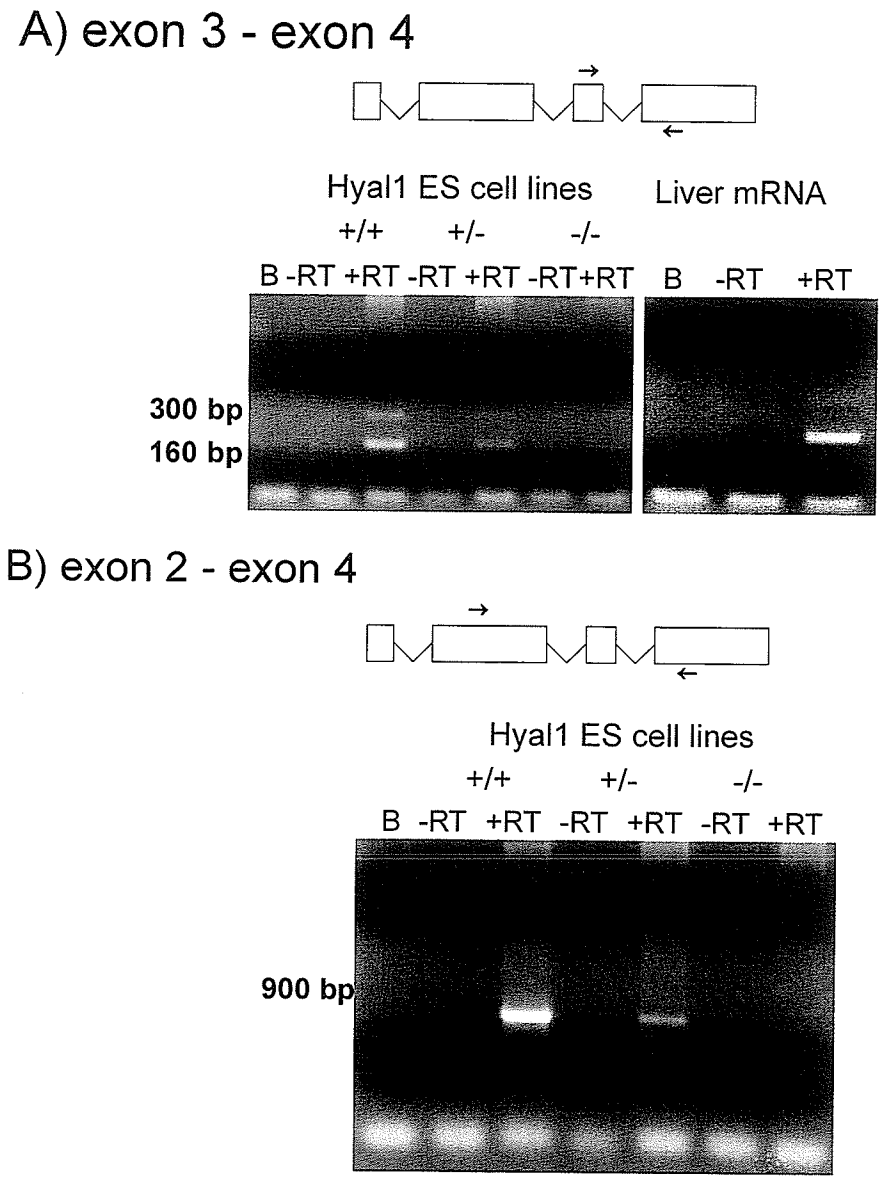

Figure 12: RT-PCR analysis of *Hyal1* mRNA in +/+, +/- and -/- ES cell lines. Primers used for PCR are denoted by arrows on the schematic representation of the *Hyal1* mRNA shown in both A) and B). Within the mRNA schematic, untranslated region and exons are diagrammed as boxes and removed intronic sequence is shown as lines. In A), primers spanning exon 3 and exon 4 detected two bands of 160 and 300 bp from in mRNA from liver, +/+, +/- and -/- ES cell lines. However, primers spanning exon 2 to exon 4, with the forward primer within the deleted exon 2, detected the expected 900 bp amplification product only in +/+ and +/- ES cell lines indicating that the remaining *Hyal1* transcripts are not wild-type.

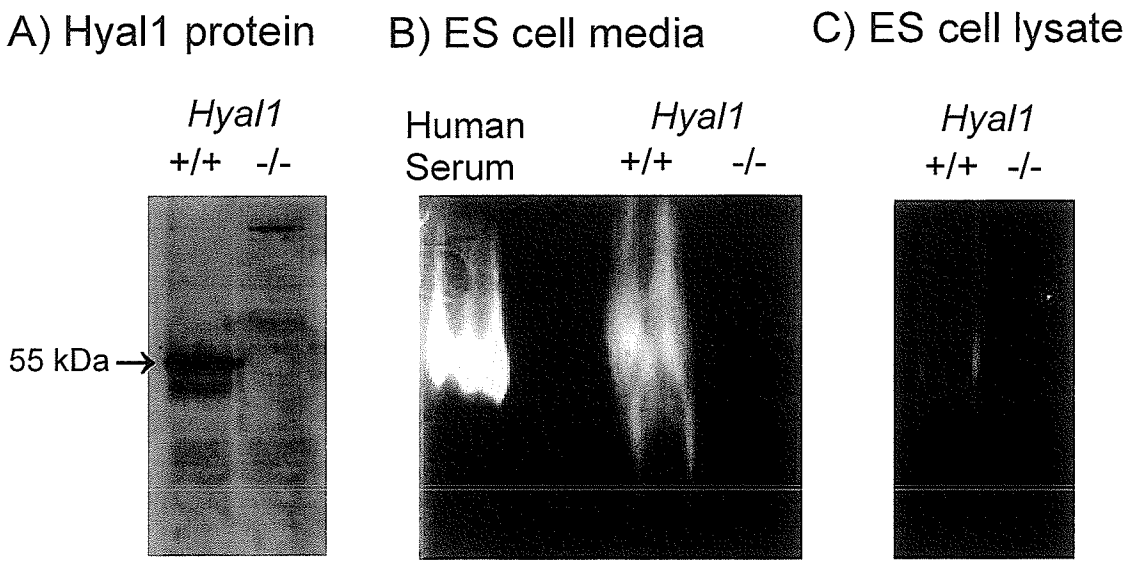

Figure 13: Analysis of Hyal1 protein and enzymatic activity in *Hyal1* +/+ and -/- ES cell lines.
Immunoblot analysis of ES cell lines using an anti-Hyal1 (1D10) monoclonal antibody in A) detected a 55 kDa protein corresponding to Hyal1 in a *Hyal1* +/+ ES cell line that was not found in the *Hyal1* -/- cell line. Zymography of ES cell media (20 µl of 10 fold concentrated media / lane) in B), and cell lysate (56 µg / lane) in C), detected areas of clearing representing hyaluronidase activity in a *Hyal1* +/+ ES cell line. No activity was detected in a *Hyal1* -/- ES cell line. Since samples were separated by electrophoresis under non-denaturing conditions, the molecular weight of proteins in the activity bands could not be determined.

line, but was undetectable in the -/- ES cell line (Figure 13A). Zymography of concentrated media and cell lysates from the *Hyal1* -/- ES cell line displayed no residual activity confirming that the Neo integration resulted in a null allele (Figure 13B, 13C).

3.3 Discussion

The expression and homology of the mouse and human *Hyal1/HYAL1* genes was previously characterized and compared[100]. Therefore, I undertook the next step in generating a mouse model of disease through the construction of a correctly targeted mouse *Hyal1* +/- ES cell line. Two targeting constructs were designed and generated in this process. The first construct, p*Hyal1* Neo/TK, was a simplified design, constructed to completely replace exon 2 of the *Hyal1* gene upon correct homologous recombination events with the *Hyal1* loci. The second construct, p*Hyal1* β-geo, was a more complicated design, made with the objective of reducing the number of colonies to be screened to identify correctly targeted clones. To accomplish this, a positive selection marker β-geo containing an upstream IRES element was incorporated into the construct to allow expression from the endogenous promoter. This reduces the number of colonies to be screened because the chance of a random recombination event occurring near an active promoter is low. In addition, the p*Hyal1* β-geo construct upon correct incorporation can allow detection of *Hyal1* expressing cells *in vivo* by staining for LacZ that would be expressed from the β-geo cassette. This would serve as a tool to identify cell types likely to require Hyal1 function.

Both targeting constructs were successfully generated through complicated cloning strategies using a variety of previously constructed cloning vectors. Upon ES cell transfection and screening of G418 resistant cell lines, I found that the targeting efficiencies of these constructs were low. Only 1 targeted ES cell line, generated from the p*Hyal1* Neo/TK targeting construct, was identified from 299 putatively positive ES cell lines that were screened. This resulted in a targeting frequency of 0.3% for the p*Hyal1* Neo/TK construct. Additionally, the p*Hyal1* β-geo construct resulted in significantly less G418 resistant colonies to be screened, 39 in total; however no correct integration was identified.

For the purpose of increasing the chance of correct recombination events, the p*Hyal1* Neo/TK construct was designed to contain a minimum of 3.4 kb of homologous sequence in each arm and contained 7.2 kb total. In retrospect, the homology contained on the 5' arm of the targeting construct included an intergenic region that carried a substantial amount of repetitive sequence. This is likely to have resulted in incorrect or random recombination events within the ES cell genome. In addition, a large number of G418 resistant colonies did not survive selection after picking or yielded DNA concentrations too low for Southern screening. Therefore to increase the chance of correct targeting events, a targeting construct designed to either extend further within the 5' region of *Hyal1* to include sequence from *Hyal2,* an upstream gene, or removal of the repetitive sequence from the p*Hyal1* Neo/TK construct would be beneficial in attempting to generate additional *Hyal1* targeted ES cell lines. Additionally, the use of a shorter region of homology would facilitate PCR based screening of G418 resistant ES cell lines. This would allow screening of larger

numbers of G418 resistant colonies and detect recombination events even in cell lines with lower DNA yields.

The p*Hyal1* β-geo construct was originally designed with the objective of reducing the number of G418 resistant colonies to be screened while also attempting to maintain alternative transcripts between *Hyal1* and downstream genes, *Fus2* and *Hyal3*. To perform both of these tasks, the β-geo cassette was incorporated into exon 4 of the *Hyal1* gene under an IRES element to allow expression while being downstream of the alternative splice sites. Additionally, a 9 bp deletion was incorporated into the 5' homologous arm to produce a functionally null allele in normal and alternative transcripts. While this attempt was amicable, the design of a knock-in that ignores the effects of the integration on the alternative transcripts may aid in generating targeted ES cell lines due to uninterrupted regions of homology on the 5' end of the construct. Such design would involve the flanking of exon 2 with loxP sites as well as the incorporation of the β-geo cassette into intron 2 of the *Hyal1* gene or directly integrating β-geo into exon 1 where transcription is initiated. The drawback to such a design would be that a researcher must consider the effects on alternative transcripts and whether they are of biological relevance. Future studies would need to delineate effects due to those alterations.

While the generation of *Hyal1* +/- ES cell lines is dependent on the rate of homologous recombination between an exogenous and endogenous sequence, the production of *Hyal1* -/- ES cell lines must be mediated by different genetic events. In our hands, the production of the *Hyal1* -/- ES cell line from the correctly targeted *Hyal1* +/- ES cell line occurred at a surprisingly high frequency. Eighteen of the

colonies resistant to high G418 concentrations were screened and 9 were found to be putatively positive *Hyal1* -/- ES cell lines. Six of these *Hyal1* -/- ES cell lines were screened for correct integration using the additional 5' probe, identifying 5 *Hyal1* -/- ES cell lines. Taking into account, that all 9 putatively positive ES cell lines were not screened, this resulted in an efficiency rate within the range of 27 – 44 % presumably resulting from mitotic recombination or chromosome loss and duplication[170]. While this ES cell line has not been used for biochemical studies to date, it could be a valuable resource in the future. The Neo incorporation into *Hyal1* resulted in an absence of detectable Hyal1 wild-type RNA, protein and/or activity. This suggests that the Neo integration resulted in a functionally null allele and therefore mice generated from the *Hyal1* +/- ES cell line would carry a null allele.

Chapter 4: Generation of chimeric mice and molecular characterization of the effects of the *Hyal1* targeted (-) allele

Acknowledgements:

The *Hyal1* +/- R1 ES cell line was blastocyst injected by Nichola Wigle from the laboratory of Dr. Geoff Hicks (CancerCare Manitoba, Winnipeg, MB) and aggregated by Xioali Wu from the laboratory of Dr. H. Ding (University of Manitoba, Winnipeg, MB). X-rays of chimeric mice were reviewed by Dr. Martin Reed (Health Sciences Center Children's Hospital, Winnipeg, MB). A portion of the research results presented in this Chapter is in a manuscript accepted by the journal of Human Molecular Genetics and is currently in press.

4.1 Introduction

In Chapter 3, I described the identification of a *Hyal1* +/- ES cell line that could be used for generating a mouse model of Hyal1 deficiency. The generation of a Hyal1 deficient mouse model first requires the use of this *Hyal1* +/- ES cell line to produce mouse chimeras. This can be performed by using aggregation and/or blastocyst injection, two techniques that have been used as early as 1968[171]. Resulting chimeras are bred to allow transmission of the mutant allele, as long as it is carried in a significant number of germ cells. Subsequent, *Hyal1* +/- mice can be interbred to establish a colony of +/+, +/- and -/- mice to use in the analysis of phenotype.

The molecular and biochemical effects of the targeted *Hyal1* Neo integration must be determined to establish the validity of comparing the phenotype of this mouse model to human MPS IX. Characterization of the murine *Hyal1* locus shows that it is a complex region with *Hyal2*, *Hyal1*, *Fus2* and *Hyal3* all localized within 19 kb on chromosome 9F[100]. Tightly linked loci containing gene families, can have unexpected phenotypes due to differences in the expression of closely linked genes. As an example, three separate phenotypes has been reported in *Mrf4* targeted mice, a myogenic regulatory factor gene[172]. However, the gene targeting designs used to generate the *Mrf4* deficient mice, differ only by their respective position in the gene and the orientation of the selection cassette[172]. Two of these phenotypes show unexpected skeletal defects that appear to be due to alterations in the expression of the closely linked gene, *Myf5*, another myogenic regulatory factor gene. The skeletal

defects of one of these *Mrf4* targeted mouse lines display skeletal defects similar to *Myf5* -/- mice, suggesting that the *Mrf4* -/- skeletal phenotype may be due to differences in the expression of *Myf5* [173]. In addition, *Myf5* +/- *Mrf4*+/- mice display a skeletal phenotype that also resembles *Myf5* -/- mice, further suggesting the skeletal phenotype of *Mrf4* -/- mice is due to a *Myf5* down-regulation[174]. Down-regulation of expression is also found in the targeted β-globin locus due to the integration of a Neo cassette in the locus region[175]. This Neo integration suppresses β-globin expression and the effects are due to the cassette itself, as expression is restored upon removal of Neo[175]. Given the close proximity of *Hyal1* with neighboring *Hyal2, Fus2* and *Hyal3* genes, an alteration in the expression of these genes could result in a severe phenotypic aberration not truly associated with a Hyal1 deficiency.

Changes in gene expression are not the only effects described that can be caused by gene targeting. Aberrant splicing or exon skipping has also been demonstrated to occur in gene targeted mice in a mouse model of cystic fibrosis. Exon skipping and aberrant splicing of *Cftr* mRNA in these mice results in transcripts containing residual function[176]. Although the phenotype of these mice display ion transport defects common to cystic fibrosis, this model does not contain the intestinal obstruction described in the other mouse models[176-178].

In LSDs, the severity of disease is inversely proportional to the level of residual activity. Milder forms of lysosomal storage disorders, including Tay-Sachs disease, Sandhoff disease, Niemann Pick disease, MPS I and many others, have been described due to residual enzymatic activity as low as 0.13 %[7, 178, 179]. Therefore, given the mild human phenotype of MPS IX, even a small amount of residual Hyal1

activity could result in the complete absence of the disease symptoms. Therefore, a complete characterization of the effects of *Hyal1* gene targeting is essential to establish the use of this mouse model in phenotype analyses.

This chapter describes our attempts at generating a mouse line from the *Hyal1* +/- ES cell line generated and identified in Chapter 3. While we were unable to generate a *Hyal1* +/- mouse line of our own due to complications in the targeted ES cell line, a *Hyal1* +/- (B6.129X1- *Hyal1*^{tm1Stn}/ Mmcd ; MMRRC: 000086-UCD) mouse line became available from the Mutant Mouse Regional Resource Centers (MMRRC; The Jackson Laboratory). This *Hyal1* +/- mouse line was obtained from the MMRRC and since this line was not yet described, we characterized the molecular effects in this line to validate its use for phenotypic analyses. No information was available on the integration site of Neo in the *Hyal1* +/- mouse line from the MMRRC and the effects of the mutation were not known. Therefore, we established the position of Neo integration in *Hyal1*, examined the expression of closely linked *Hyal2*/*Fus2* genes and established the complete deficiency of Hyal1. Thus we determined that the *Hyal1* +/- mouse line available from the MMRRC could be used for further phenotypic studies.

4.2 Results

4.2.1 Chimeric mice generated from the *Hyal1* +/- R1 ES cell line

The *Hyal1* +/- R1 ES cell line described in Chapter 3 was expanded and approximately 4-12 ES cells were injected into blastocyst-stage embryos. In total, 80

C57Bl/6J blastocysts were injected. Although several offspring were generated, only 2 live chimeras were born. Both of these chimeras displayed gross phenotypic abnormalities (to be described below) during the first days of life and died by post-natal day 5. Two additional attempts were made to generate chimeras by aggregation of the *Hyal1* +/- ES cell line with CD-1 embryos. Five additional weak chimeras were obtained. More severely affected mice, with a higher degree of chimerism as suggested from the higher percentage of coat color from the R1 ES cell line used, were considerably smaller compared to littermates. This is shown in Figure 14A that displays an affected male chimera and normal C57Bl/6J littermates. Severely affected chimeras also displayed a restricted thoracic cavity and an extended abdominal cavity (Figure 14B). Malformations in the hands and tails of the chimeras were evident from birth. The paw abnormalities of chimeric mice included swollen digits, as well as an abnormal curvature to the fingers and joints of the paws (Figure 14C, 14D and 14E). The tail was abnormally long and contained several identifiable kinks or twists (Figure 14F).

One of the more severely affected female chimeras, shown in Figure 14B, was euthanized at post-natal day 10.5 for X-ray analysis. X-rays showed that the upper 4 ribs of this severely affected female chimeric mouse were small, particularly on the left side, and that tail vertebrae were asymmetric (Figure 15). The curvature associated with the left wrist and the kink in the tail of the chimeric mouse displayed increased space between bone structures representing potential cartilage increases or failed patterning in caudal vertebrae development. The remaining 2 male and 2 female chimeras generated by aggregation showed no visible abnormalities and were

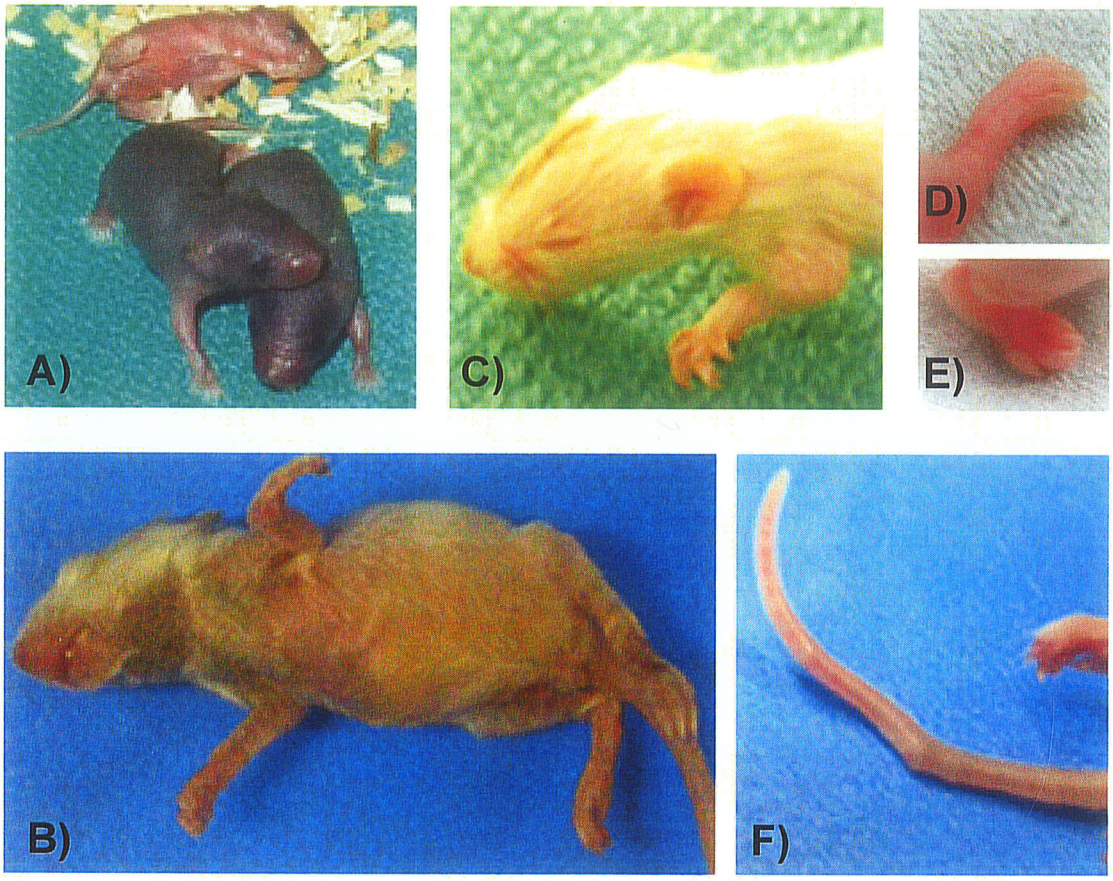

Figure 14: Gross phenotype of affected chimeras.
Affected chimeras were smaller than normal littermates, as shown in A). The thoracic cavity was restricted (B), the abdomen was severely distended, B), and the fore paws showed an abnormal curvature of the wrist, C) and D) in affected chimeras. Digits of the affected chimeras were swollen, E) and the tails displayed multiple kinks and/or twists , F).

Figure 15: X-ray of a female affected chimera (P 10.5).
The upper 4 ribs of a moderately affected chimera were small, especially on the left side, and tail vertebrae were asymmetric. An increased amount of joint space was also evident in the rotated left wrist and between tail vertebrae.

crossed with CD-1 mice. However, the chimeras were unable to transmit the *Hyal1* targeted allele.

4.2.2 *Hyal1* targeted mice from the Mutant Mouse Regional Resource Centers (MMRRC)

4.2.2.1 Characterization of the targeted *Hyal1* mutation and genotyping of mice

During the attempts to generate Hyal1 deficient mice of our own, a *Hyal1* +/- mouse line became available from the MMRRC. Therefore, we obtained two sets of *Hyal1* +/- male and female mice (N=7 generations of backcrossing to the C57Bl/6J background) and interbred them to establish a colony. The MMRRC's genotyping strategy was based solely on detecting the presence of Neo and was unable to provide an allele specific genotyping strategy or details regarding the targeting event in these mice. Therefore, we characterized the site of the Neo integration. Since the site of Neo integration was unknown, digestion with a BsrGI restriction enzyme that has sites flanking the *Hyal1* gene, and a DNA probe to a 3' external region, was chosen for Southern analysis (Figure 16A). Southern analysis was performed on BsrGI digested genomic DNA from *Hyal1* +/+, +/- and -/- mouse liver. A 9.7 kb band, corresponding to the expected size of the wild-type (+) *Hyal1* DNA fragment was detected in *Hyal1* +/+ and *Hyal1* +/- mice (Figure 16A, lanes 1 and 2). A 10.7 kb band, presumably due to a Neo integration and representative of the targeted (-) allele, was detected in *Hyal1* +/- and *Hyal1* -/- mice (Figure 16A, lanes 2 and 3).

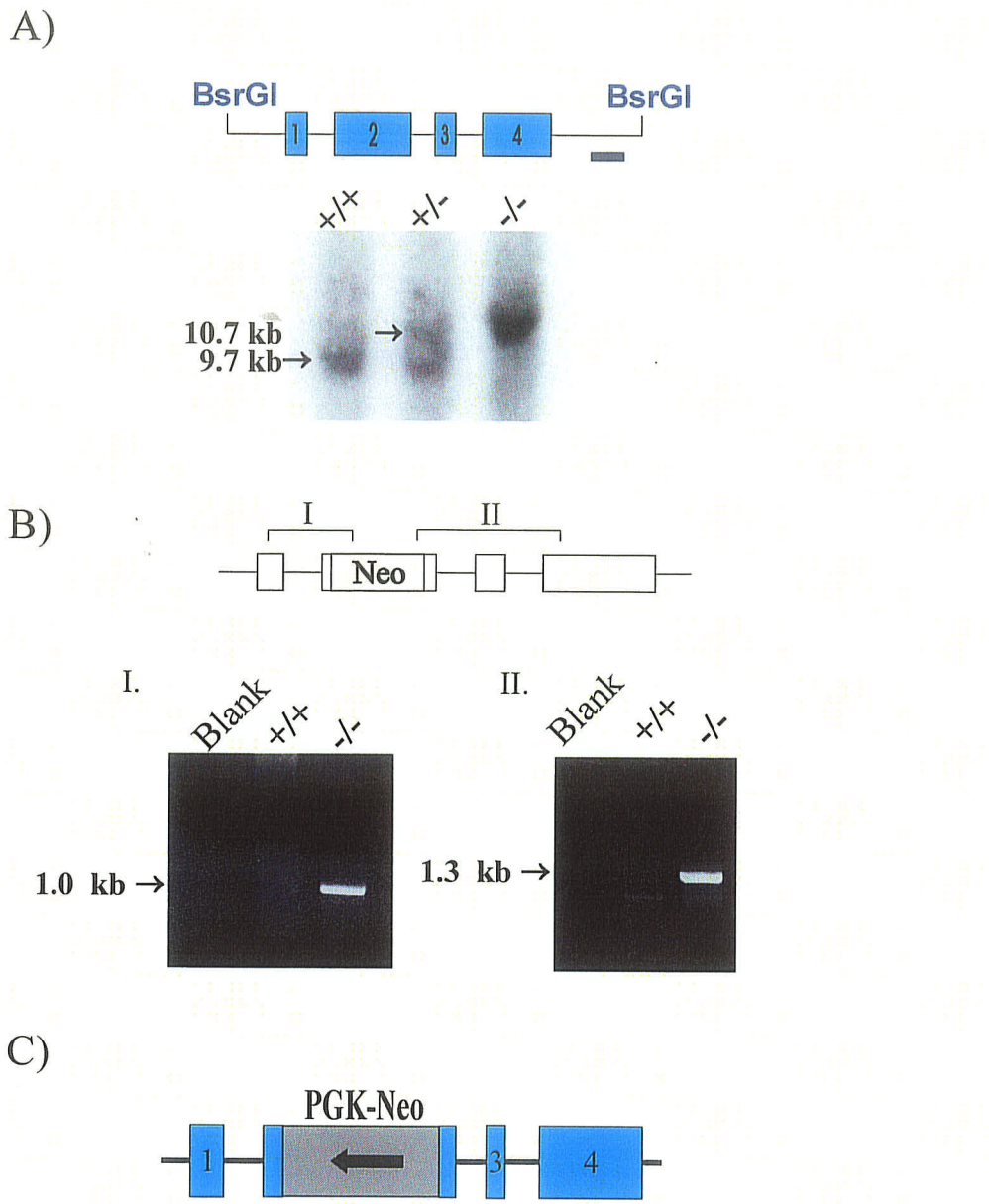

Figure 16: Southern analysis of the *Hyal1* gene region and the characterization of the targeted mutation.

Southern analysis of the *Hyal1* gene region detected the expected 9.7 kb wild-type band and a 10.7 kb band representing the targeted allele (A). PCR amplification of the junctions between *Hyal1* and the Neo cassette of genomic DNA from -/- mice resulted in 1.0 and 1.3 kb PCR products. The blank lane represents a no template control reaction included in the amplification. The PCR products were subsequently sequenced to determine the site of Neo integration and the results are shown diagrammatically (C). Sequencing determined that the Neo cassette was inserted into exon 2 and deleted half of the coding region including the predicted active site of the enzyme. Exons and the Neo resistance cassette are displayed as boxes, intronic and intergenic regions are shown as lines and the arrow in the resistance cassette indicate s the direction of transcription.

Having confirmed the presence of Neo in the *Hyal1* locus, the 5' and 3' junctions between *Hyal1* and the Neo resistance cassette were PCR amplified. The 5' junction was PCR amplified using a forward primer in exon 1 and a reverse primer within Neo (WPG 379, WPG 617), whereas the 3' junction was PCR amplified using a forward primer in Neo and a reverse primer in exon 4 (WPG 618, WPG 198)(Figure 16B). The resulting PCR products of 1.0 kb (Figure 16B, panel I) and 1.3 kb (Figure 16B, panel II) were cloned for sequencing (data not shown). The Neo resistance cassette was integrated into exon 2, which resulted in the deletion of 753 bp (NT_039477.6; nucleotides 6487518-6488270) of sequence encoding nearly half of the protein (Figure 16C). A DWE amino acid sequence essential for the activity of PH-20 [25] and the predicted active site of the hyaluronidase enzymes [104] was removed by the integration of Neo.

For routine genotyping of mice, PCR based strategies were developed. A 340 bp DNA sequence, deleted in exon 2 by the integration of Neo, was PCR amplified (WPG 612, WPG 613) to detect the wild-type allele in *Hyal1* +/+ and +/- mice (Figure 17A). The targeted (-) allele was detected by PCR amplification (WPG 610, WPG 611) of a 270 bp segment of the Neo coding region (Figure 17B) in *Hyal1* +/- and -/- mice. Therefore, *Hyal1* +/+ mice have only the 340 bp wild-type PCR-amplified fragment (Figure 17A), *Hyal1* +/- mice have both the 340 bp wild-type fragment and the 270 bp Neo-targeted fragment (Figure 17A and 17B) and *Hyal1* -/- mice had only the 270 bp Neo-targeted PCR-amplified fragment (Figure 17B). All further analyses used this PCR based genotyping strategy to identify +/+, +/- and -/- mice.

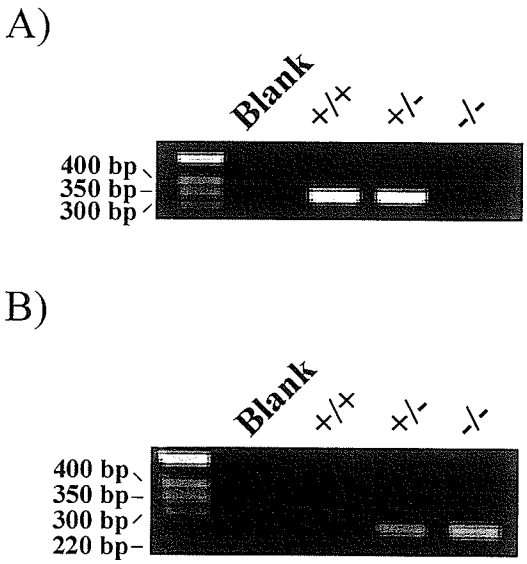

Figure 17: Genotyping of tail genomic DNA from *Hyal1* mice.
A PCR specific for the wild-type (+) allele was performed using primers specific to the deleted region of exon 2 (A). A 340 bp product was identified in +/+ and +/- mice, but was absent in -/- mice. A PCR amplification designed for the targeted (-) allele was performed using primers to the Neo coding region (B). A 270 bp product amplified in +/- and -/- mice, but not from +/+ mice. The blank lanes represents a no template control reaction included as a negative control with the PCR reactions.

4.2.2.2 Analysis of *Hyal1* and surrounding gene transcripts in *Hyal1* -/- mice

Northern analysis was used to examine the effect of the *Hyal1* targeting event on *Hyal1* gene expression. Using a nearly full-length cDNA probe, the two most abundant *Hyal1/Fus2* co-transcripts, of 6.2 kb and 4.5 kb in size, were detected in liver mRNA of *Hyal1* +/+ mice (Figure 18A, lane 1). These transcripts were not detected in the liver mRNA of *Hyal1* -/- mice (Figure 18A, lane 2). Since only the most abundant *Hyal1* co-transcripts were detected, the abundance of the *Hyal1* trancript was analyzed by quantitative PCR in +/+ and -/- mice. The primers used in these quantitative analyses amplified the boundary between exon 1 and exon 2, detecting all normal and variant *Hyal1* transcripts previously described[100]. In comparison to liver *Hyal1* expression in +/+ mice, the *Hyal1* transcript levels in the livers of 3 -/- male mice ranged from 1-2% of normal levels (Figure 18B). This resulted in a statistically significant reduction of the majority of the *Hyal1* transcript (P=0.001).

The presence of residual *Hyal1* transcript was verified by RT-PCR analysis using primers that span the exon 2 - exon 4 boundary (WPG 190, WPG 198). A 200 bp PCR product was amplified from liver cDNA of *Hyal1* +/+ and -/- mice (Figure 18C, lanes 2 and 4). However, to ensure the remaining *Hyal1* transcripts were not wild-type, RT-PCR was performed with a primer specific to the deleted portion of exon 2 and a reverse primer specific to exon 4 (WPG 182, WPG 198). A 900 bp PCR product was amplified from cDNA in *Hyal1* +/+ mice, but was not amplified in *Hyal1*

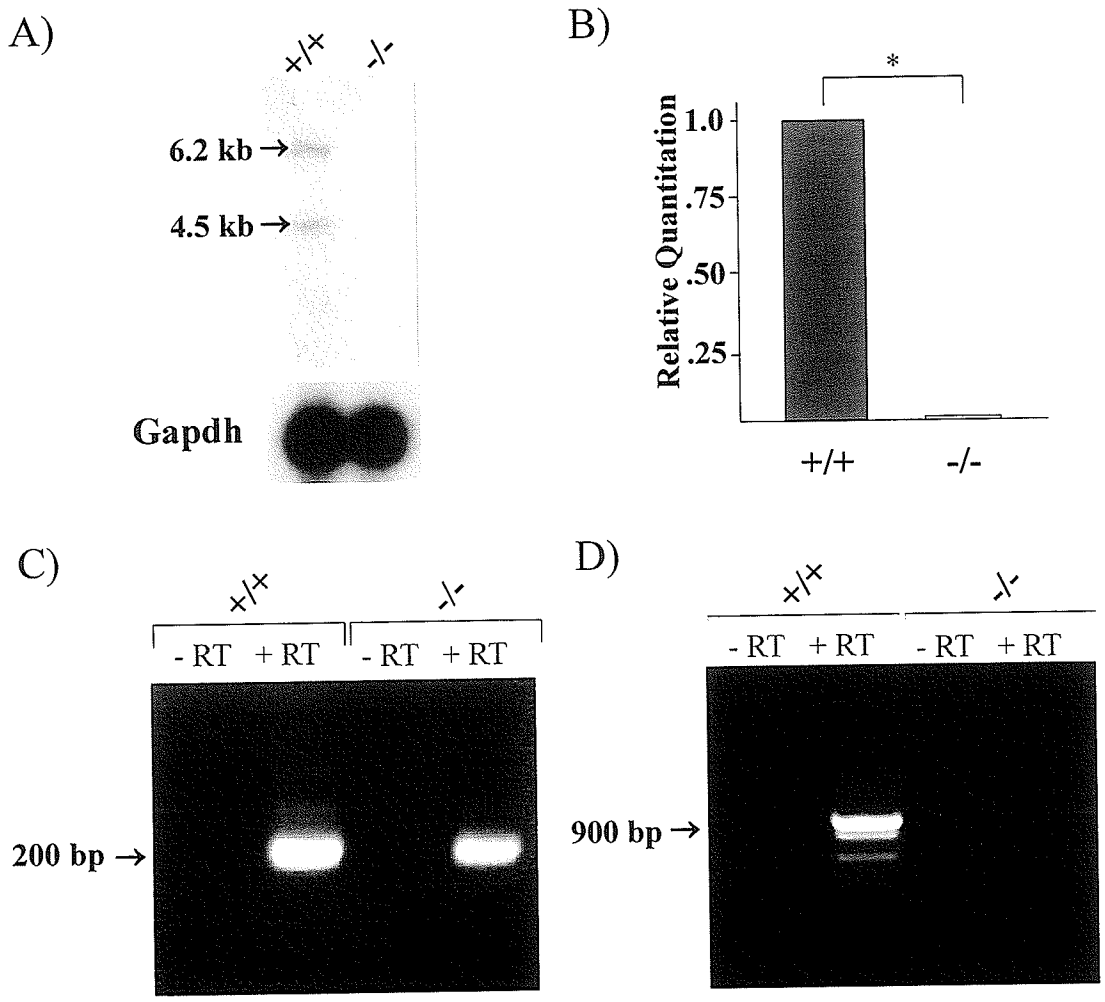

Figure 18: Northern, real-time and RT-PCR analysis of liver *Hyal1* transcripts in *Hyal1* +/+ and -/- mice.

Northern analysis (A), using a probe spanning the coding region, detected the most abundant *Hyal1* variant transcripts in +/+ mice that were not identified in -/- mice. Real-time PCR of *Hyal1* in liver mRNA found significantly reduced (P=0.001) transcripts in -/- mice compared to +/+ mice (B). The presence of *Hyal1* transcript in *Hyal1* -/- mice was verified by RT-PCR using primers that span exon 2 and 4 (C). RT-PCR analysis, using primers specific to exon 4 and the deleted region of exon 2 showed amplification in +/+, but not -/- mice (D) indicating that the remaining *Hyal1* transcripts were not wild-type.

-/- mice (Figure 18D, lanes 2 and 4). This suggests residual transcripts are not wild-type *Hyal1*.

To examine if the integration of Neo was affecting the expression of the two closest genes located upstream or downstream of *Hyal1*, northern analysis of *Hyal1* +/+ and -/- liver mRNA was performed for *Hyal2* and *Fus2*. Two *Hyal2* transcripts of 1.8 kb and 2.0 kb were identified in mouse liver of +/+ and -/- mice (Figure 19A; lanes 1 and 2). The abundance of these transcripts appeared equivalent between +/+ and -/- liver mRNA (Figure 19A, lanes 1 and 2). Northern analysis of *Fus2* identified the two most abundant *Hyal1/Fus2* co-transcripts of 4.5 kb and 6.2 kb in +/+ mice (Figure 19B, lane 1). However, the intensity and size of these transcripts was reduced in -/- mice (Figure 19B, lane 2). Despite this difference in the *Hyal1/Fus2* co-transcripts, *Hyal1* +/+ and -/- mice displayed equivalent expression of the most abundant 1.5 kb *Fus2* wild-type transcript (Figure 19B, lanes 1 and 2). These analyses suggest that the Neo integration does not alter expression of the *Hyal2* and *Fus2*, the closest genes either upstream or downstream of *Hyal1*.

4.2.2.3 Analysis of Hyal1 protein and enzymatic activity in *Hyal1* -/- mice

Western analysis of *Hyal1* +/+ and *Hyal1* -/- mouse liver lysates was performed to determine if residual transcripts encoded a protein product. A single 55 kDa protein band was identified in the liver lysate of a *Hyal1* +/+ mouse, but was not detected in the *Hyal1* -/- mouse (Figure 20A). *Hyal1* +/+, +/- and -/- mice were also examined for residual activity by zymography. Native zymography of serum samples using 5 µl (Figure 20B), and overloaded with 15 µl (Figure 20C), displayed areas of

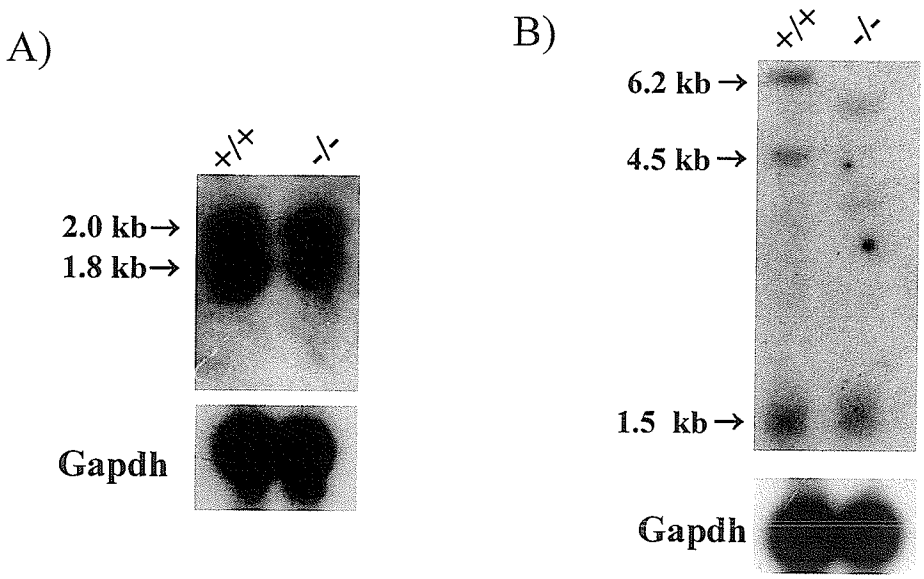

Figure 19: Northern analysis of the *Hyal2* and *Fus2* genes.
In A), no detectable differences were detected in the two liver *Hyal2* transcripts in *Hyal1* +/+ and -/- mice. The liver mRNA abundance of *Fus2* (1.5 kb), displayed in B), is similar in *Hyal1*+/+ and -/- mice. However the sizes of the *Hyal1*/*Fus2* (4.5 kb and 6.2 kb) co-transcripts were decreased in *Hyal1* -/- mice.

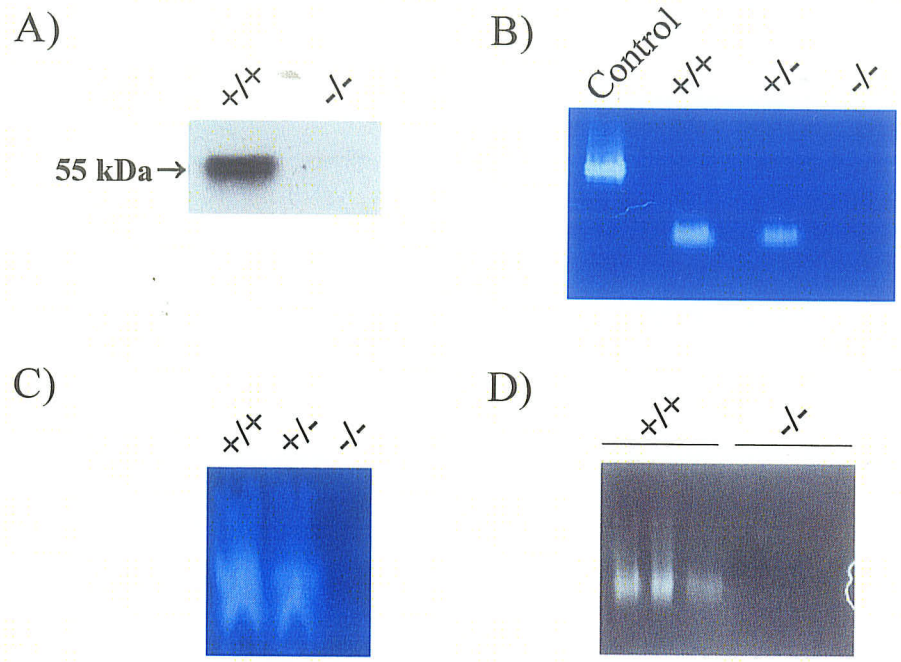

Figure 20: Protein and enzymatic activity of *Hyal1* in +/+ and -/- mice.
Western blot analysis of liver lysates (30µg protein/lane) using a anti-Hyal1 (1D10) monoclonal antibodydetected a 55 kDa protein representing Hyal1 in +/+, but was not detected in -/- mice (A). Zymography of serum (5 µl) from *Hyal1* +/+ and +/- mice identified areas of clearing representing hyaluronidase activity that were not detected in *Hyal1* -/- mice (B). The control lane consists of 1µl of human serum. Zymography of larger volumes of serum (15 µl) detected areas of clearing representing Hyal1 activity in +/+ and +/- mice that were not identified in -/- mice (C). HA substrate zymography of liver lysates (30µg protein/lane) from three +/+ mice displayed Hyal1 activity, represented by areas of clearings, however no detectable activity was seen in three -/- mice (D). The sizes of the protein bands responsible for activity could not be determined, since the samples were separated under non-denaturing conditions.

clearing representing hyaluronidase activity in +/+ and +/- mice (Figure 20B; Figure 20C). No clearings were found in serum from *Hyal1* -/- mice using either 5 µl or 15 µl (Figure 20B; Figure 20C). HA substrate zymography of liver lysates detected activity in all 3 *Hyal1* +/+ mice tested (Figure 20D), however no Hyal1 activity was identified in any of the *Hyal1* -/- mice examined (Figure 20D).

4.3 Discussion

The phenotype of the chimeric mice generated from the *Hyal1* +/- ES cell line identified in Chapter 3 was not expected. MPS IX is an autosomal recessive disorder and the presence of a phenotype in chimeric mice suggested a dominant inheritance from the ES cell line. Additionally, *Hyal1* +/- mice from the MMRRC did not display a similar phenotype. Therefore, we presumed the *Hyal1* +/- ES cell line that we had generated contained additional genetic alterations. Chromosomal or genetic alterations are common in cell culture due to a gradual selective pressure for cells with a higher proliferative capacity. A number of genetic alterations have been documented to occur by *in vitro* culture of mouse ES cell lines including aneuploidy, chromosome structure abnormalities and alterations in epigenetic modifications[145, 180, 181].

While the *Hyal1* targeted ES cell line was no longer of use to us in the continued process of generating a *Hyal1* null mouse, this cell line could be used for identifying novel genes important in cartilage and bone formation in the thoracic cavity, limbs and tail. Cytogenetic analysis of the chromosomal content of this ES cell line would be beneficial to investigate the possibility of aneuploidy or the

presence of chromosomal duplications, deletions or translocations. Microarray analysis of gene expression in the targeted ES cell line could be used to examine alterations due to epigenetic defects and/or the possibility of altering expression of closely linked genes within the *Hyal1* locus region. A complete phenotypic characterization of cartilage and bone in chimeras would be necessary to determine the importance of the identified gene (s) in the development of these structures.

Subsequently, a *Hyal1* +/- mouse line became available from the MMRRC. These mice contained an insertion of a Neomycin resistance cassette into exon 2 causing a deletion of a large proportion of the coding region. This mutation resulted in a decrease in *Hyal1* transcripts to 1-2% of normal expression levels. Our data suggests that the residual *Hyal1* transcripts identified in -/- mice were not wild-type *Hyal1* transcripts and contained the Neo cassette. The integrated Neo cassette resulted in an absence of detectable Hyal1 protein, serum and liver activity in -/- mice. These results show that the targeted mutation contained within this mouse line results in a functionally null allele.

Although resistance cassettes have been demonstrated previously to cause alterations in expression of genes in close proximity, it appears that the two genes closest to *Hyal1* either upstream (*Hyal2*) or downstream (*Fus2*), have no detectable difference in normal transcript expression between +/+ and -/- mice. Interestingly, during northern analysis of *Hyal2* in the liver, a 2.0 kb band was identified in addition to the expected 1.8 kb wild-type transcript. This transcript has been identified before in our lab, using the human coding sequence as a probe, and may represent an uncharacterized *Hyal2* transcript produced by alternative splicing and/or intron

retention. No detectable difference in *Hyal2* expression was identified in either transcript in -/- mice.

Northern analysis of *Fus2* expression identified that the full-length 1.5 kb transcript of *Fus2* displayed normal expression in -/- mice; however the two most abundant *Hyal1/Fus2* co-transcripts[100] appeared to have a reduced expression and size. This size decrease may reflect an alternative splicing or exon skipping event in these transcripts due to integration of the Neo cassette. The inability to detect these co-transcripts using the *Hyal1* probe in northern analysis suggests that the *Fus2* probe is more sensitive than the *Hyal1* cDNA probe used in these studies. In addition, the identification of residual *Hyal1* transcripts by more sensitive real-time and RT-PCR methods, suggest that these co-transcripts may represent the remaining *Hyal1* transcripts identified in -/- mice. These co-transcripts have been characterized previously and do not produce the Fus2 protein *in vitro*[100]. Therefore, the studies presented in this chapter confirm that Hyal1 is completely deficient in this mouse model and validate its use in examining the phenotypic or functional consequences of a Hyal1 deficiency.

Chapter 5: Phenotypic Characterization of *Hyal1* null mice

Acknowledgements:

Tissue GAG analysis of collected mouse tissues was performed in the laboratory of Dr. Sharon Byers (Women's and Children's Hospital, Adelaide, SA Australia). Determination of skin GAG content was performed in our laboratory by Rick Hemming. Safranin O and Toluidine blue staining of joints was performed in the laboratory of Dr. John Mort (Shriner's Hospital for Children, Montreal, QC). X-rays of mice skeletons was performed in the laboratory of Dr. Anna Plaas (Rush University Medical Center, Chicago, IL, USA) and electron microscopy sections were examined by Dr. Jim Thliveris (University of Manitoba, Winnipeg, MB). Dr. Robert Stern (University of California San Francisco, San Francisco, CA, USA) performed expert pathological slide review. Special thanks to Vasantha Atmuri, Nehal Patel and Rick Hemming for technical assistance with tissue collection and Dr. Sabine Hombach-Klonish for assistance in joint histology. A large proportion of these studies is presented in a manuscript accepted by the journal of Human Molecular Genetics and is currently in press.

5.1 Introduction

While the contribution of the individual hyaluronidase genes in HA turnover is unknown, the phenotype of the MPS IX patient indicates the importance of HYAL1 in HA turnover in the joint. Acetabular erosions, mild short stature, a nodular synovia and a popliteal cyst in the MPS IX patient all suggest that HYAL1 is essential to HA degradation in the cartilage, joint and surrounding fluids[19]. The HA storage identified in macrophages and fibroblasts of periarticular masses and the serum HA elevations (48-90 fold) indicates that HYAL1 may also be essential in HA degradation in non-skeletal tissues. However, given the broad expression profile of Hyal1 and the absence of detectable organomegaly in the one patient described, the specific contribution of Hyal1 to tissue HA turnover is unknown. Therefore, a thorough characterization of tissue GAG accumulation and the phenotype associated with a mouse model of deficiency could identify additional sites where Hyal1 is essential and validate this model for the study of pathogenesis and therapeutic treatments in MPS IX.

This chapter describes the characterization of *Hyal1* null mice by the investigation of the gross phenotype and the examination of tissues for GAG accumulation. Guided by the phenotype described in human MPS IX, the stature, joint dysfunction, skeletal structure and organ storage were examined in null mice. Since extensive joint abnormalities are found in human MPS IX, we chose to perform histological analysis of the knee joint in null mice for evidence of joint involvement. When evidence of osteoarthritic changes was identified, we determined sites of HA

storage. This chapter provides the initial description of the phenotype associated with murine MPS IX and its comparison to the human disease.

5.2 Results

5.2.1 Gross phenotype

Hyal1 -/- mice were observed up to 12 months in females (n=7) and 20 months in males (n=5). *Hyal1* -/- mice were viable and appeared normal until they were sacrificed. Although no statistical tests were performed, litter sizes appeared normal for the C57Bl/6J strain (6-8 pups/litter). The genotype distribution did not differ by chi-square analysis ($\chi^2 = 0.909$; P=0.63; n = 110) from the expected 1:2:1 Mendelian ratio of +/+ : +/- : -/- genotypes.

Age-matched *Hyal1* +/+ and -/- mice were sacrificed at 6, 9 and 12 months of age. No masses were identified over the joint and the movement of *Hyal1* -/- mice appeared normal in comparison to *Hyal1* +/+ mice. At the time of necropsy, there were no visible differences in the body size, tissue size or morphology. Body and organ weights were collected at the time of necropsy to be analyzed for evidence of short stature and/or organomegaly. No significant difference was found between the body size of *Hyal1* +/+ and -/- mice at 6 (male P=0.11 [n=6]; female P=0.50 [n=5]), 9 (male P=0.55 [n=6]; female P=0.13 [n=6]) or 12 (male P=0.06 [n=7]; female P=0.07 [n=7]) months of age (Figure 21). *Hyal1* +/+ and -/- mice at the oldest time-point of 12 months did not display evidence of organomegaly, as -/- mice did not have significantly increased brain, heart, liver, lungs, spleen or kidney weights (Figure 22).

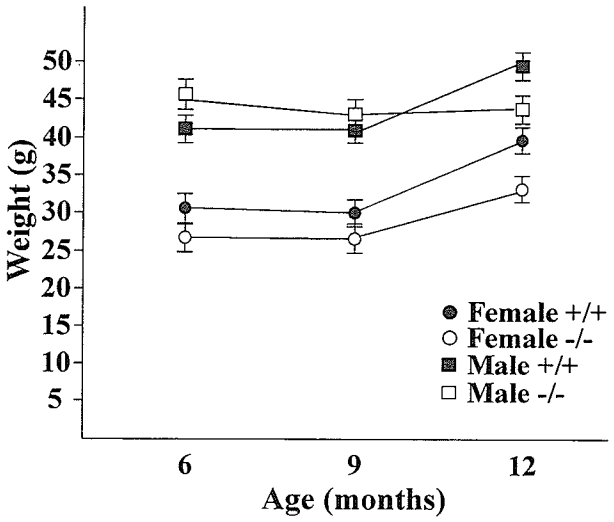

Figure 21: Body weights of *Hyal1* +/+ and -/- mice at 6, 9 and 12 months.
Mean body weights of *Hyal1* +/+ and -/- mice were calculated and compared in males (n=6) and females (n=6, except 6 months n=5) by ANOVA at 6, 9 and 12 months of age. Mean body weights (g) ± standard error mean (SEM) are plotted at each age. No statistically significant results were identified at 6 (P= 0.11 in males; P= 0.50 in females), 9 (P= 0.55 in males; P= 0.13 in females) or 12 months (P= 0.06 in males; P= 0.07 in females).

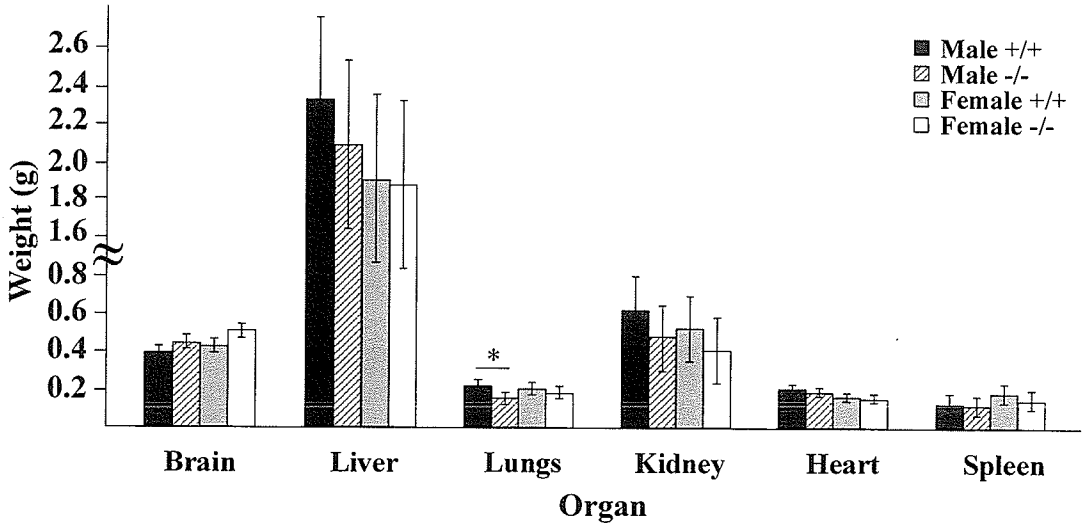

Figure 22: Organ weights of 12 month *Hyal1* +/+ and -/- mice.
The organ weight of 12 month male and female mice were compared between genotypes by analysis of covariance (3-way analysis of variance) with body weight defined as the covariant. Mean organ weights (g) ± standard deviation (SD) are plotted and the * denotes statistical significance at $P<0.003$.

The lung weights of *Hyal1* -/- male mice were significantly lower in comparison to age-matched +/+ mice (Figure 22). However, lung weights were not statistically different between genotypes of 6 (+/+ = 0.18 ± 0.01, -/- = 0.17 ± 0.01;[mean ± SD; P=0.11; n=6]) or 9 (+/+ = 0.17 ± 0.02, -/- = 0.16 ± 0.02; [mean ± SD; P= 0.09; n=6]) month old male mice. Due to the ability of HA to attract water that may mask small differences in size, the dry tissue weights of 12 month mice were examined and compared. No detectable differences in any tissue dry weights examined were observed between +/+ and -/- mice at 12 months (n=3) and the dry lung weights of male mice were also not found to significantly differ (Figure 23). In addition, no pathology has been identified in the lungs of male mice to date.

Upon the absence of visible MPS IX symptoms at necropsy, an additional group of 20 month old males were added to compare *Hyal1* +/- and -/- mice. Male 20 month *Hyal1* +/- and -/- mice did not significantly differ in body weights (P= 0.28; n=4) and no evidence of organomegaly was detected in *Hyal1* -/- mice in the brain, heart, liver, lung or kidney (Figure 24). The only gross abnormality observed in *Hyal1* -/- mice was a spotting of the liver that progressed with age in severity and the number of animals that were affected. This was observed in all genotypes and was especially evident in the male gender. Based on histological and biochemical analysis of these mice, the spotting of the liver appears to be due to liver disease in this strain of mice. See sections 5.2.3.2 and 5.2.4 for the full description of these findings.

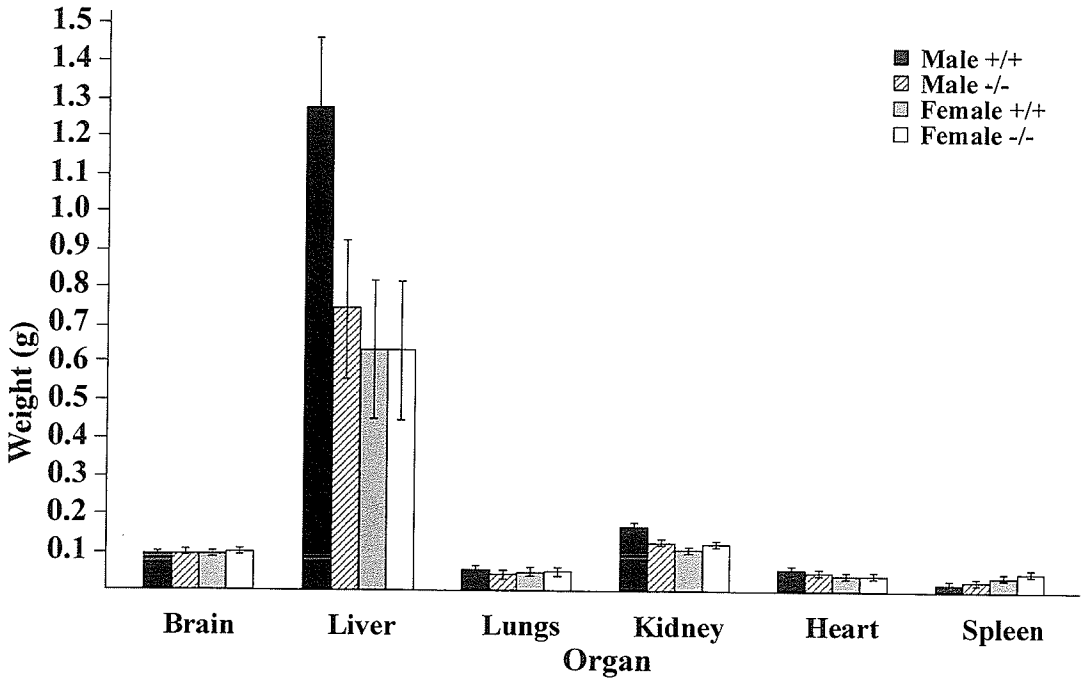

Figure 23: Dry organ weights of 12 month *Hyal1* +/+ and -/- mice.
The organ weights of 12 month male (n=3) and female (n=3) mice were compared between genotypes by analysis of covariance (3-way analysis of variance) with body weight defined as the covariant. Mean organ weights (g) ± standard deviation (SD) are plotted.

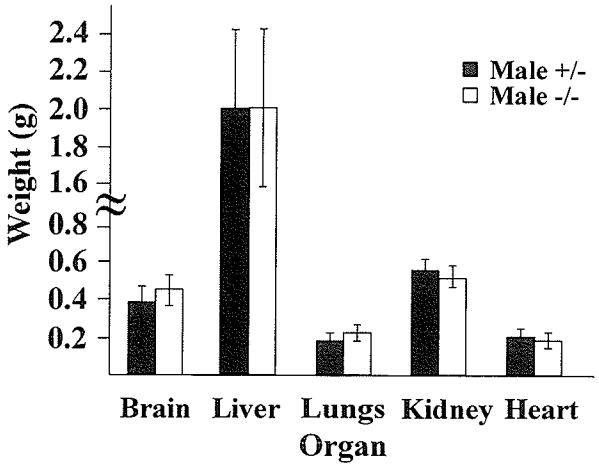

Figure 24: Organ weights of 20 month male *Hyal1* +/- and -/- mice.
The organ weights of 20 month male mice were compared between genotypes by analysis of covariance with body weight defined as the covariant. Mean organ weights (g) ± standard deviation (SD) are plotted. No statistically significant differences were detected.

5.2.2 Joint phenotyping

To look for preliminary evidence of joint involvement, one set of male *Hyal1* +/- and -/- mice were examined at 12 months using a basic form of gait analysis. The paws of mice were painted with water-soluble inks and mice walked freely in a narrow chamber lined with paper. The stride length and weight distribution on the imprint of the fore and hind limbs was examined (Figure 25). Fore and hind limb stride length were comparable in each mouse. The +/- mouse had average fore and hind limb stride lengths of 5.5 ± 0.5 cm and 5.6 ± 0.9 cm (mean ± SD) respectively, whereas the -/- mouse displayed average fore and hind limb stride lengths of 7.5 ± 0.1 cm and 7.5 ± 0.6 cm respectively. Therefore, fore and hind limb stride lengths were pooled and the mean stride length was compared between the +/- and -/- mice. The +/- male mouse had a mean stride length of 5.7 ± 0.8 cm , while the mean stride length of the -/- mouse was slightly larger at 7.5 ± 0.4 cm. Stride length is documented to vary with speed, but both +/- and -/- mice were in the normal range (5.5cm – 8.3cm) documented previously[182]. In addition, the fore and hind limb paw imprints appeared to have an even distribution of weight across the pad in both the +/- and -/- mouse (Figure 25).

X-ray analysis was performed on male (n=3) and female (n=3) 12 month +/+ and -/- mice. No major skeletal abnormalities were identified. A representative pair of 12 month female +/+ and -/- mice is shown in Figure 26. No major skeletal defects were seen in the thoracic vertebrae, lumbar vertebrae, pelvis structures or caudal tail vertebrae suggesting no evidence of skeletal dysplasias. In addition, the width, length

A) *Hyal1* +/-

B) *Hyal1* -/-

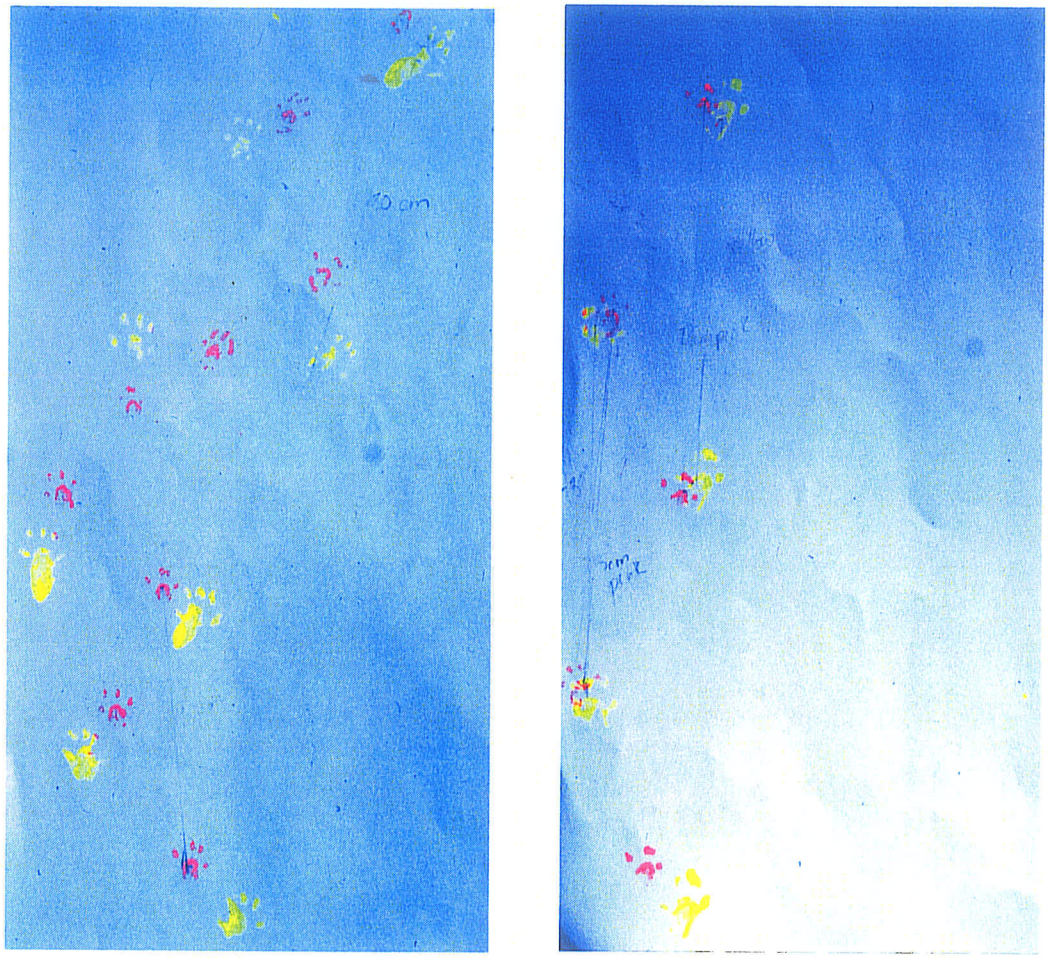

Figure 25: Gait analysis of *Hyal1* +/- and -/- mice.
Fore paws (pink) and hind paws (yellow) were captured on paper using water-soluble color paints prior to sacrifice. The weight distribution and stride length were not significantly different between genotypes by analysis of the color imprintations.

A) *Hyal1* +/+ 12 months female

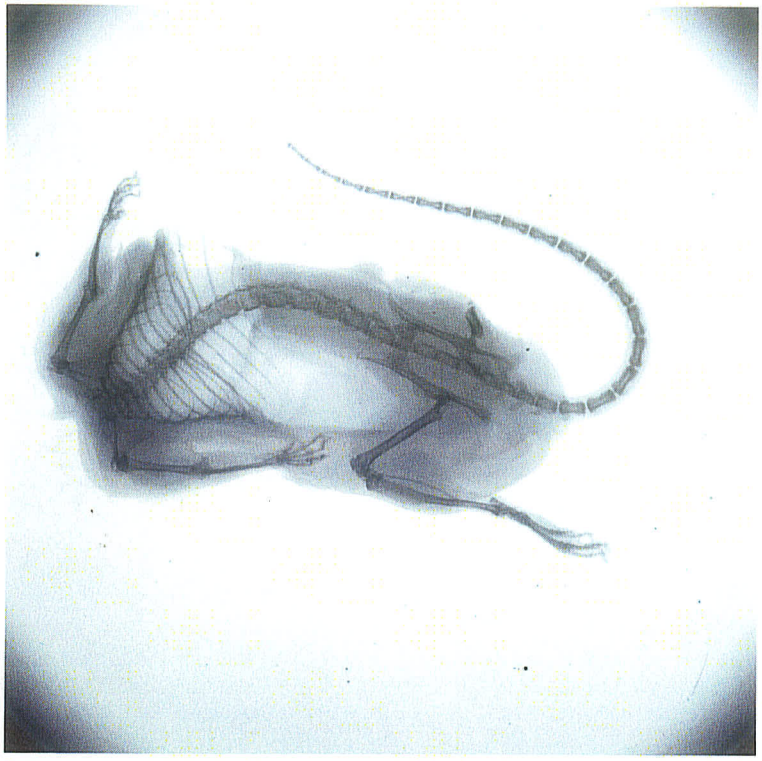

B) *Hyal1* -/- 12 months female

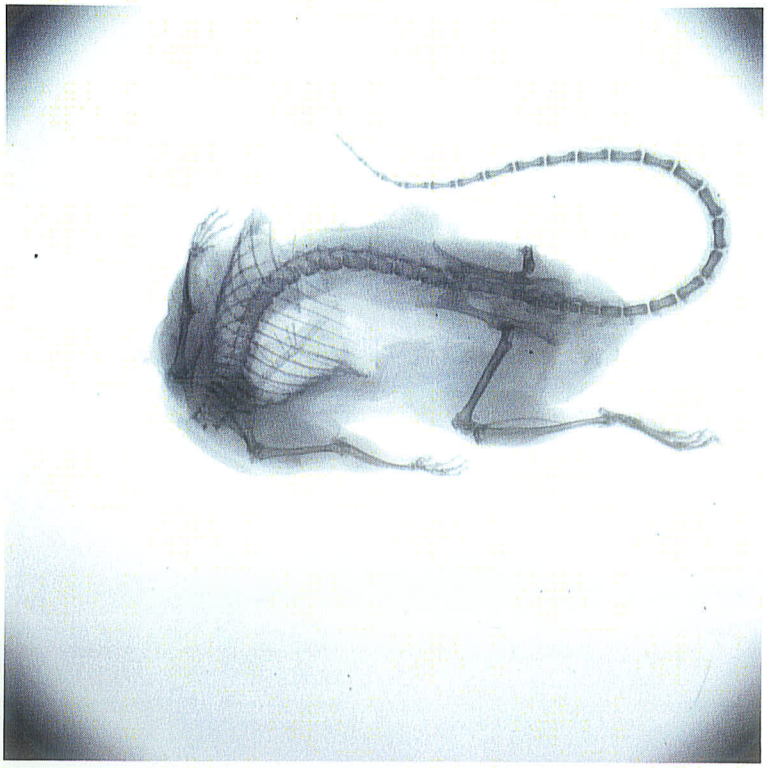

Figure 26: X-ray analysis of skeletal structure of *Hyal1* +/+ and -/- mice.

and symmetry of vertebrae appeared normal, as well as the appearance of the limb bones (Figure 26).

Due to the extensive joint involvement in the clinical description of the MPS IX patient, the knee joints of *Hyal1* +/+ and -/- mice were examined for histological pathology. Safranin O and Toluidine blue staining of the femur and tibia of *Hyal1* +/+ and -/- mice was used to assess the GAG / proteoglycan content, as well as the overall histological structure of the cartilage and bone. Safranin O staining displayed a decreased intensity in *Hyal1* -/- mice indicating proteoglycan loss in the articular cartilage, the cartilage responsible for bearing daily pressures on the joint (Figure 27A- F). Although the C57Bl/6J strain of mice appeared to undergo proteoglycan and cartilage loss with age, the premature loss of proteoglycans was evident in *Hyal1* -/- mice at 3 months (Figure 27A and 27D). Knee joints were examined in mice of 3 (n=1), 6 (n=1), 9 (n=2), 12 (n=6) and 20 (n=1) months. The loss of articular cartilage proteoglycans was found in -/- mice of all ages and progressed with age (Figure 27D, 27E, 27F). In addition, an osteophyte, a bony outgrowth common in osteoarthritis, was observed on the tibial plateau of 20 month -/- mice (Figure 27F; arrow).

Toluidine blue staining confirmed the loss of proteoglycans that was most evident within the superficial layer of the articular cartilage (Figure 28). Chondrocyte cell numbers appeared normal in -/- mice at younger ages suggesting chondrocytes were capable of undergoing normal division (Figure 28). This was evidenced by chondrocyte clusters present in -/- mice at 3 months of age (Figure 28D). Proteoglycan loss and bony outgrowths, such as an osteophyte, are common pathological occurrences in osteoarthritis[183, 184].

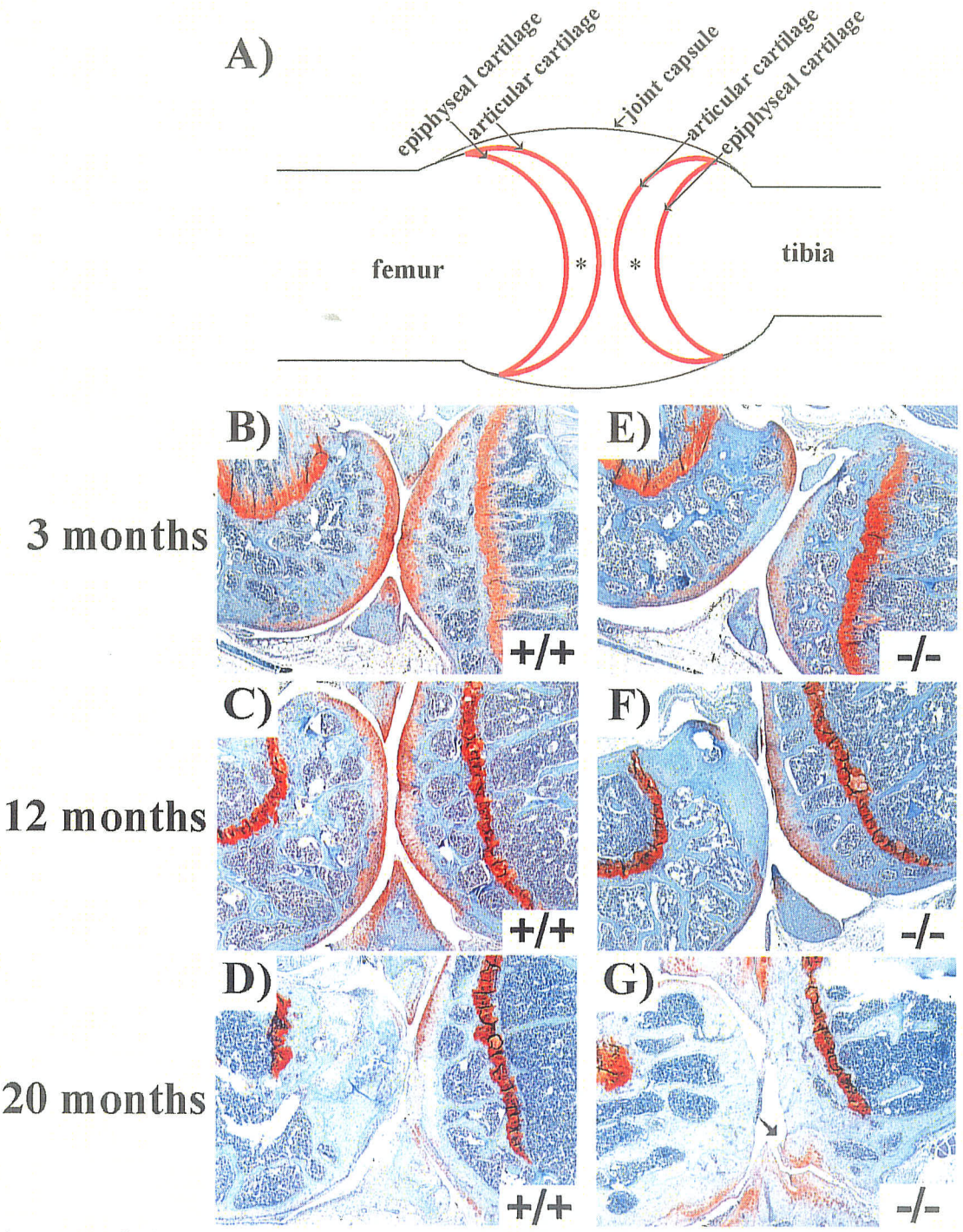

Figure 27: Safranin O staining of knee joints from *Hyal1* +/+ and -/- mice.
A schematic of the knee joint (A) indicates the two types of cartilage present in the joint, as well as the joint capsule and bone structures. The * denotes the epiphysis of the femur and/or tibia. The cartilage proteoglycan content was stained with Safranin O (red) and the joint was counterstained with hematoxylin (blue/purple) in age matched male 3, 12 and 20 month mice. *Hyal1* -/- mice displayed a loss of proteoglycans in the articular cartilage (E, F, G) in comparison to +/+ mice (B, C, D) at 3, 12 and 20 months. The arrow in G) indicates an osteophyte, a bony outgrowth typically found in osteoarthritis, that was identified in a 20 month *Hyal1* -/- mouse.

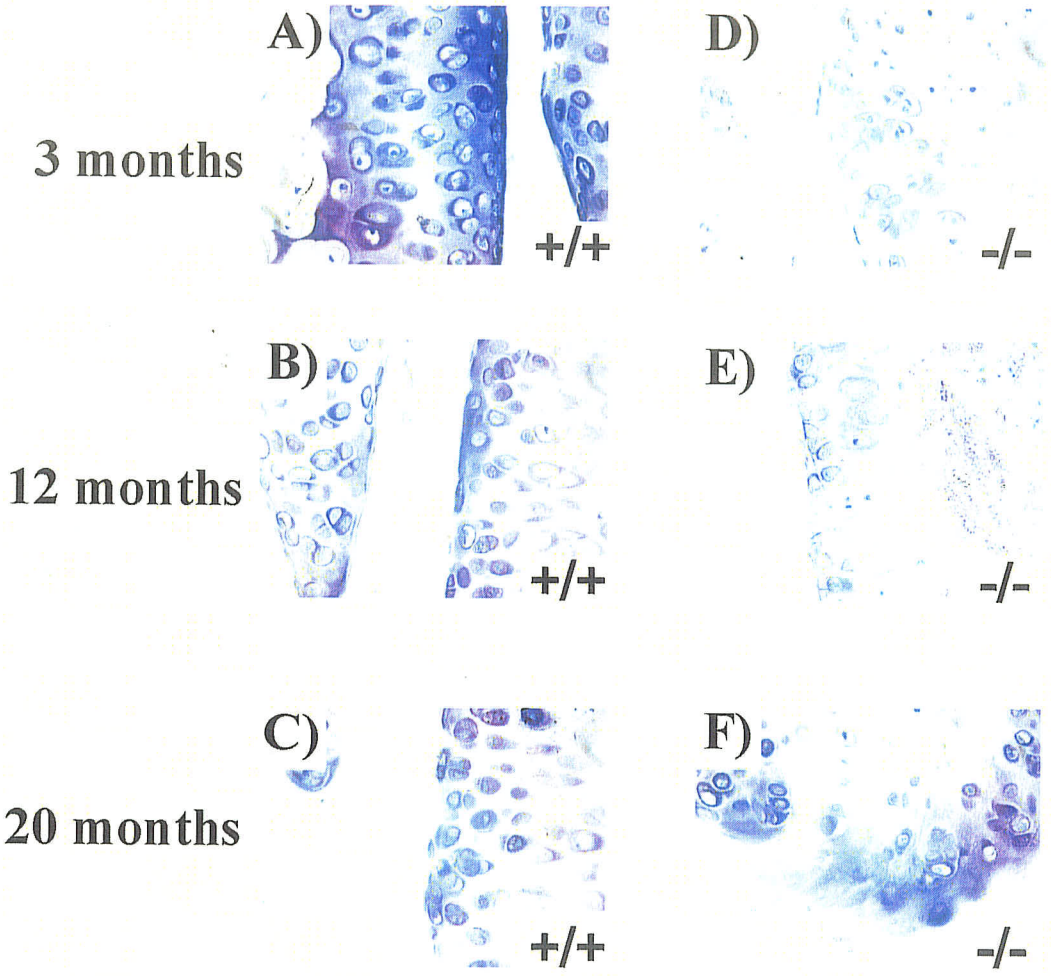

Figure 28: Toluidine blue staining of knee joints from *Hyal1* +/+ and -/- mice. Sulfated GAGs of the articular cartilage were stained with Toluidine blue (purple/blue) and the joint structure was counterstained with hematoxylin (blue) in age-matched male mice of 3, 12 and 20 months. *Hyal1* -/- mice displayed a loss of sulfated GAGs in the articular cartilage (D, E, F) compared to age-matched +/+ mice (A, B, C) at 3, 12 and 20 months.

No evidence of intracellular vacuolation was histologically visible in the chondrocytes of -/- mouse joints (Figure 28D, 28E, 28F), therefore HA was localized in joint sections of 3 and 12 month *Hyal1* +/+ and -/- mice using a HA binding protein (HABP). HA was found in the pericellular coat and/or intracellularly in articular chondrocytes of *Hyal1* +/+ and -/- mice (Figure 29A, 29B, 29D, 29E). However, in male and female *Hyal1* -/- mice a larger number of chondrocytes with intense HA staining were observed at 3 months (Figure 29B) and 12 months (Figure 29E) of age. This was most evident in mice at 12 months of age (Figure 29D, 29E), but was also observed in 3 month -/- mice (Figure 29B). In addition, at 12 months of age -/- mice displayed stronger cartilage surface HA (Figure 29E) than +/+ controls (Figure 29D).

HA was also localized in the epiphyseal cartilage, the cartilage responsible for bone elongation and growth. The epiphyseal chondrocytes of +/+ mice contained HA in the territorial matrix and to a lesser extent in the interterritorial matrix of the growth plate at 3 (Figure 29G) and 12 (Figure 29J) months of age. *Hyal1* -/- mice displayed an increased number of chondrocytes that stained intensely for pericellular and/or cytoplasmic HA (Figure 29H, 29K). Additionally, although a faint cytoplasmic stain could be detected in epiphyseal chondrocytes of +/+ mice (Figure 29G, 29J), the epiphyseal chondrocytes of *Hyal1* -/- mice displayed strong cytoplasmic staining (Figure 29H, 29K). This was most prominent at 12 months (Figure 29K), but was also found at 3 months (Figure 29H). No staining was observed in the epiphyseal or articular cartilage of control sections treated with hyaluronidase prior to HA staining (Figure 29C and 29F).

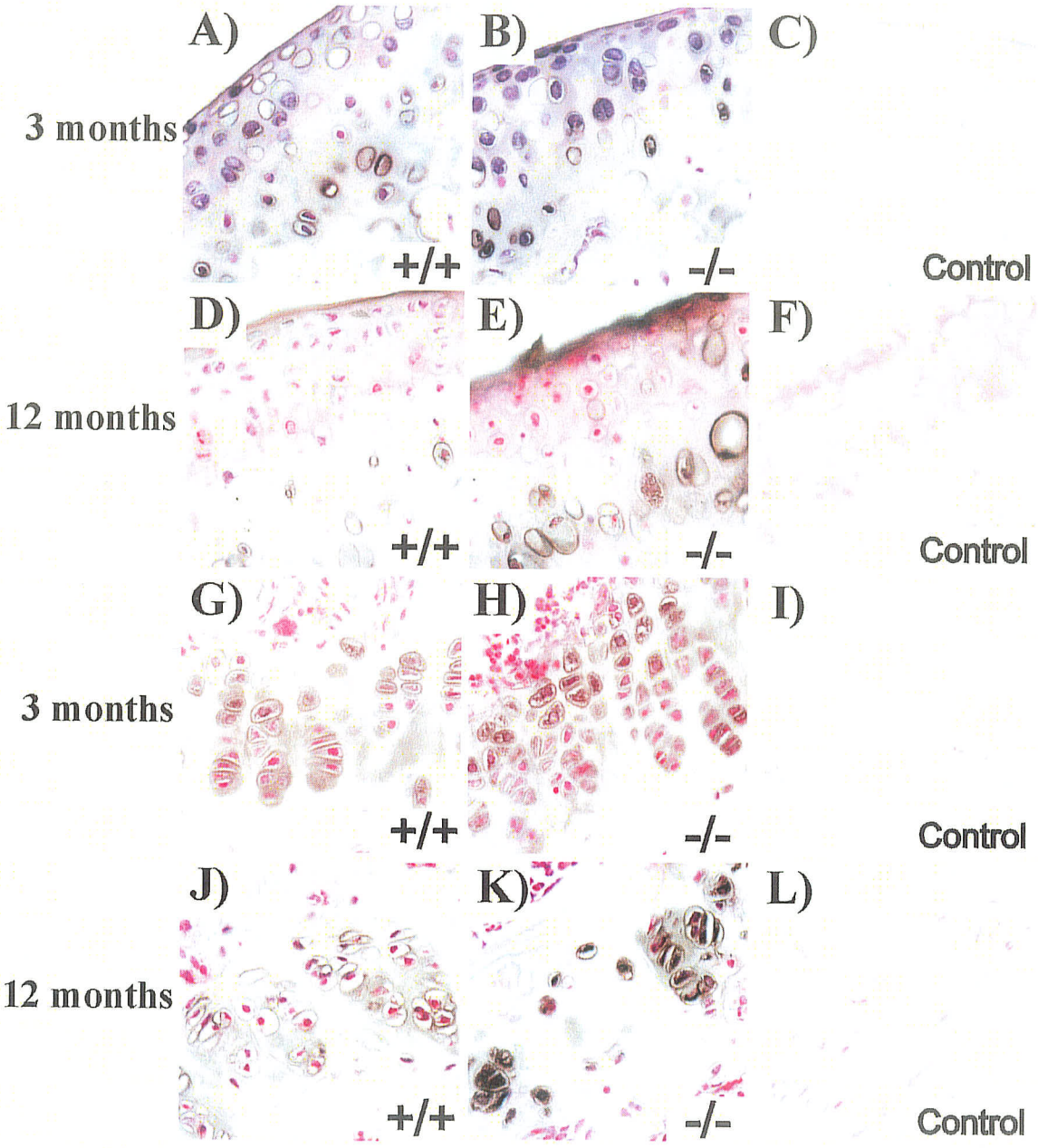

Figure 29: HA localization in the articular and epiphyseal cartilage of knee joints in *Hyal1* +/+ and -/- mice at 3 and 12 months of age.
HA (brown) was localized in the articular (A-F) and epiphyseal (G-L) cartilage of mice of 3 and 12 months. An increased number of articular chondrocytes displaying intense pericellular HA was found in -/- mice at 3 months (B) and 12 months (E) in comparison to +/+ controls (A, D). In addition, HA staining at the articular surface was more intense in *Hyal1* -/- mice at 12 months of age (E). In epiphyseal cartilage, intense pericellular and/or intracellular HA staining was detected in an increased number of epiphyseal c chondrocytes in *Hyal1* -/- mice at 3 months (H) and 12 months (K). No pericellular or intracellular HA staining was detected in the *Streptomyces* hyaluronidase treated control of articular cartilage (C, F) or epiphyseal cartilage (I, L).

5.2.3 Serum and peripheral HA accumulation

5.2.3.1 Serum HA quantitation

Serum HA concentrations were examined at each time point as an indicator of the earliest age that peripheral GAG storage may be seen in *Hyal1* -/- mice. The concentration of circulating HA did not significantly differ between ages (P=0.44, n=35), but was significantly different between sexes (P=0.0001, n=35). Males had an overall lower circulating HA concentration (408 ng/ml) than females (668 ng/ml). No significant difference in serum HA concentrations were found at any age examined (P=0.56) (Figure 30). Serum HA concentrations at the oldest age, 20 months, were not significantly different between male *Hyal1* +/- (499 ± 98 ng/ml) and -/- mice (343 ± 99 ng/ml) (Figure 31; P=0.30, n=4). Serum HA concentrations were generally highly variable between individual mice, ranging between 88 to 1136 ng/ml.

5.2.3.2 Tissue GAG and/or HA quantitation

GAG was quantitated in tissues with either high HA turnover or *Hyal1* expression in 12 month +/+ and -/- mice. The tissue GAG content ranged from 5.2 μg uronic acid/g to 161.0 μg uronic acid/g in the 6 tissues tested. Tissue GAGs were significantly different between male and female sexes (P=0.0002; n=6), which was especially evident in the lung where the female mean (111.0 uronic acid/g) was approximately 4-fold higher than the male mean (27.8 uronic acid/g). The GAG content of +/+ and -/- mice did not significantly differ in the brain, liver, lung, kidney, heart or spleen in either sex examined (Figure 32; n=3). Since the skin GAG content

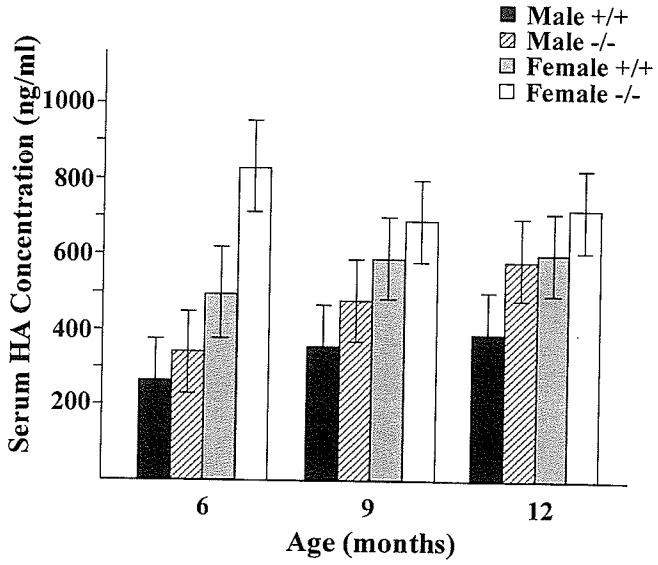

Figure 30: Serum HA concentrations of *Hyal1* +/+ and -/- mice at 6, 9 and 12 months.

The serum HA concentrations of *Hyal1* +/+ and -/- mice at 6, 9 and 12 months (n=6; except females of 6 months n=5) were determined by sandwich HA ELISA using a hyaluronic acid binding protein (HABP). Serum HA concentrations were determined by comparison to a HA standard curve. The mean HA serum concentrations (ng/ml) ± standard error mean (SEM) analyzed by MANOVA is plotted in bar graphs at each age. No statistically significant differences were identified between +/+ and -/- mice at any age examined.

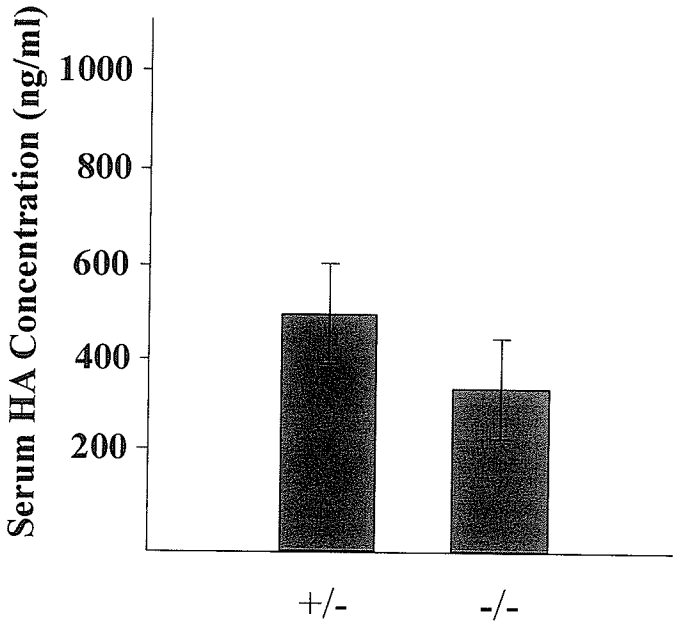

Figure 31: Serum HA concentrations of *Hyal1* +/- and -/- mice at 20 months. The serum HA concentrations of *Hyal1* +/- and -/- male mice at 20 months (n=4) were determined by sandwich HA ELISA using a hyaluronic acid binding protein (HABP). Serum HA concentrations were determined by comparison with a 4 parameter regression of a HA standard curve. The mean HA concentration (ng/ml) ± standard error mean (SEM) using ANOVA statistical analysis is plotted in bar graphs. No statistically significant differences were identified.

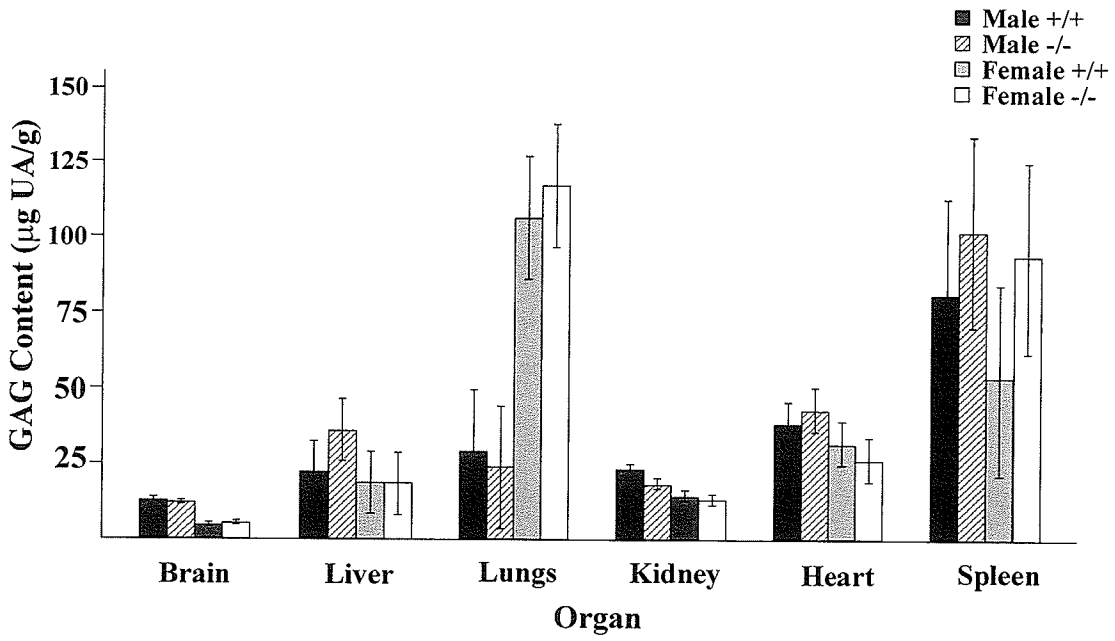

Figure 32: GAG content of high turnover or *Hyal1* expressing tissues from *Hyal1* +/+ and -/- mice.

The tissue GAG content was determined using a uronic acid assay and normalized to dry tissue weight in male and female +/+ and -/- mice of 12 months (n=3) of age. The mean GAG content (µg uronic acid (UA)/g of tissue dry weight) ± standard deviation (SD) is plotted in bar graphs. No statistically significant differences were identified between male or female -/- mice in comparison to age and sex matched +/+ mice.

could not be determined by the uronic acid assay and HA accumulation was identified in the fibroblasts and macrophages of skin biopsies from the human MPS IX patient, we examined the HA content of female null mice at 3 months of age (n=2) using fluorescence assisted carbohydrate electrophoresis (FACE). No significant difference in the skin HA content of *Hyal1* wild-type (347.8 μg/g) and null (485.2 μg/g) mice was detected (P=0.58). However, to ensure HA accumulation did not occur with age we examined the HA content of skin from 12 month male and female mice (n=3) by immunohistochemistry with HABP. HA was localized to the dermis and hypodermis in male and female +/+ and -/- mice (Figure 33A, 33B). However, no identifiable differences in the distribution or intensity of HA staining were detected in -/- mice (Figure 33B). In addition upon higher magnification (63x objective), no evidence of intracellular storage was observed (Figure 33E). However, to further investigate tissues for GAG accumulation the overall architecture and cellular appearance of tissues from *Hyal1* null mice was performed.

5.2.4 Histological examination of tissue architecture and cellular ultrastructure

Histological review of hematoxylin and eosin stained tissues was performed by light microscopy, examining overall tissue architecture, connective tissue thickness and looking for evidence of intracellular vacuolation. All major tissues were examined including the brain, heart, liver, lung, kidney, spleen, muscle, skin, testes, ovaries, uterus and seminal vesicles. Male and female age-matched +/+ and -/- mice were examined at 6 (n= 2), 9 (n= 2), 12 (n= 3) or 20 months of age (n= 4 males only). No major abnormalities in *Hyal1* null mice were found in either sex. Although the

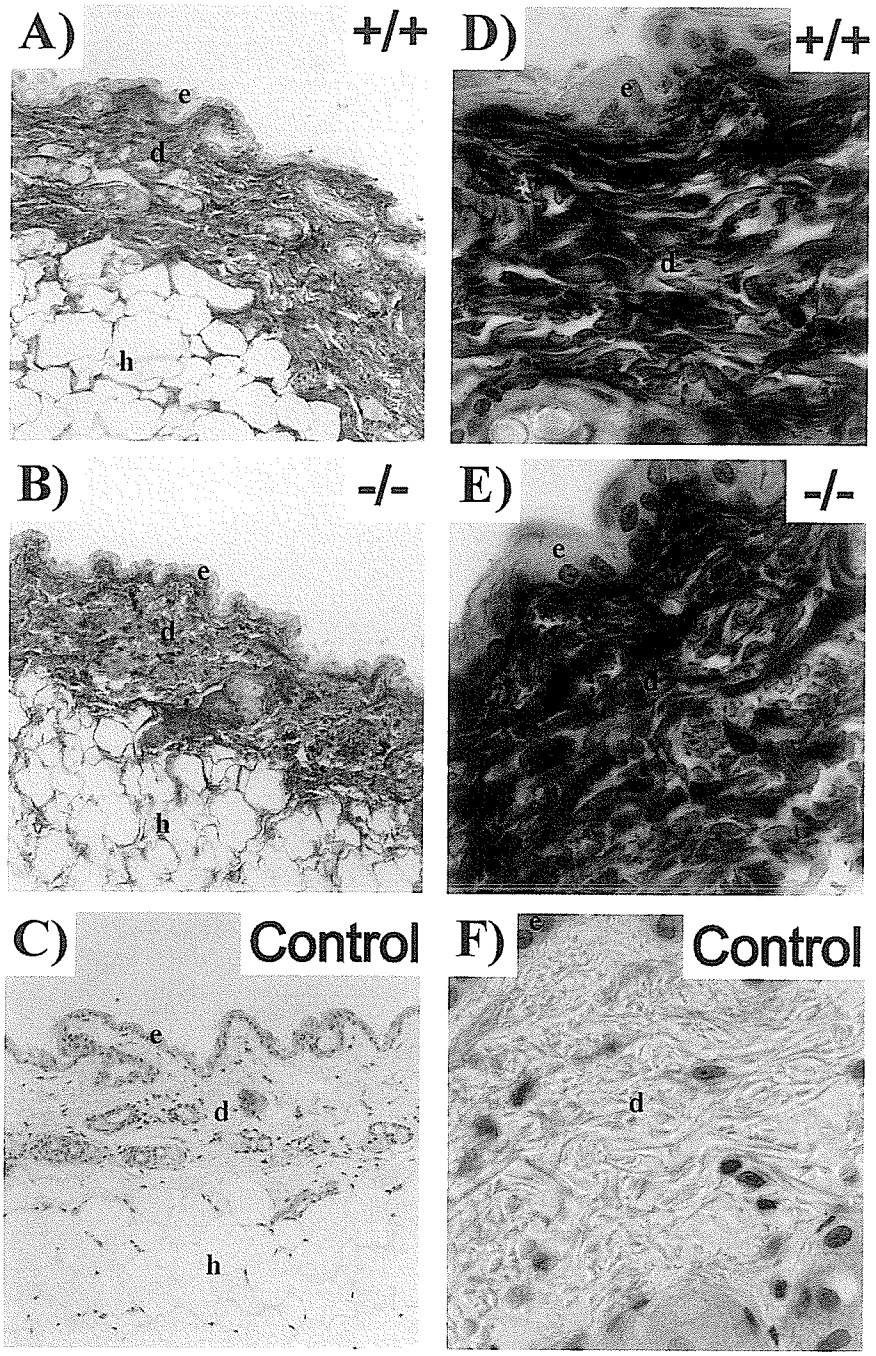

Figure 33: HA localization in the skin of 12 month *Hyal1* +/+ and -/- mice.
HA was found in the dermis and hypodermis of skin from +/+ and -/- mice (A, B). No differences in the intensity or distribution of HA (20x objective) was identified in -/- mice (B) in comparison to controls (A). Upon higher magnification (63x objective), no intracellular HA accumulation was detected in -/- mice (E). No staining in the dermis or hypodermis was detected in *Streptomyces* hyaluronidase treated controls (C, F). d shows the dermis, e shows the epidermis and h identified the hypodermis of the skin.

lung weights of male mice were significantly different between +/+ and -/- mice, no pathological abnormalities have been detected to date. A more intensive review of high expression and high turnover tissues, as well as the lungs, was performed by a pathologist who confirmed the results of the histological examination (n=1 for each gender at each age of analysis).

EM analysis of high expression and high turnover tissues, including the lungs, liver, kidney, skin and lymph node was performed on one set of animals of each gender at 12 months of age. Contrary to the MPS IX patient biopsies, no vacuolation was evident in the macrophages or fibroblasts of skin from -/- mice. The major functional cell types of tissues with high abundance or turnover of HA including the skin, intestinal lymph node, liver, kidney or lung tissues appeared normal. Liver samples from older animals were difficult to interpret as both wild-type and null animals displayed intracellular vacuolation that occasionally correlated with the infiltration of inflammatory cells. This pathological phenotype is similar to what occurs in steatohepatitis and GAG analysis in liver tissues detected no significant increase (Figure 32) suggesting liver vacuolation was not due to GAG storage.

5.3 Discussion

We have characterized a mouse model of Hyal1 deficiency and compared the mouse and human MPS IX phenotypes. The phenotype of the murine model of MPS IX is similar to that seen in the human disease. Typical of osteoarthritic changes, *Hyal1* null mice display bony outgrowths at older ages and a premature loss of the articular cartilage proteoglycans that increases in severity with age. The development

of progressive degenerative joint disease was also observed in the MPS IX patient as indicated by bi-lateral hip surgeries at age 18 and unilateral hip replacement at the age of 25 years (M. Natowicz, personal communication). In contrast to the human HYAL1 deficiency, *Hyal1* null mice display no joint masses, symptomatic evidence of joint involvement, serum HA elevations or evidence of non-skeletal tissue HA storage. Therefore, the joint involvement that results in disabling symptoms in human MPS IX appears to be the most prominent feature in both human and murine MPS IX.

This Hyal1 deficient model is one of seven murine MPS diseases described to date [185]. As is true for other murine models of lysosomal storage disorders, including Fabry disease, Tay-Sachs disease, MPS IIIB, MPS IV and others, this model is milder and does not completely recapitulate the entire human MPS IX phenotype[186-189]. However, only one MPS IX patient has been reported to date and it is therefore likely that the full range of clinical symptoms remains to be determined. The premature and degenerative joint disease seen in both human and mouse MPS IX may be used as a key pathological feature in identifying additional patients.

MPS IX mice display no apparent symptomatic evidence of joint involvement and are less severely affected than murine models of MPS I, MPS II, MPS VI and MPS VII which have significantly impaired joint function[123, 190-192]. These MPS models have a range of pathological features including a thickened joint capsule, synovial fibroblast proliferation, disorganization of the growth plate, ballooning of chondrocytes and/or synoviocytes and proteoglycan loss[123, 136, 137, 191, 192]. While most of these features are not reproducibly seen in the Hyal1 -/- mice, the proteoglycan loss within the cartilage of MPS VI models is observed consistently in murine MPS

IX. In the rat and cat MPS VI models, the accumulation of dermatan sulfate causes a loss of proteoglycan and collagen content due to an increased rate of chondrocyte apoptosis[137]. Chondrocyte cultures from these animal models show an increased ability to secrete nitric oxide and tumor necrosis factor-α[137]. The accumulation of HA within the articular cartilage of MPS IX mice at both 3 and 12 months suggests that the pericellular accumulation either causes a disruption in the ECM organization or may potentially increase the secretion of inflammatory cytokines similarly to MPS VI models. Further studies will be necessary to determine the effects of HA accumulation in the articular cartilage of MPS IX mice.

A mild alteration in the matrix components within the epiphyseal plate, similar to that seen in the articular cartilage, may also occur in MPS IX mice as a result of the increased number of chondrocytes that display pericellular HA staining. MPS I, MPS VI and MPS VII models that display more severe skeletal phenotypes, exhibit a thickened growth plate with an increased number of chondrocytes and/or a persisting epiphyseal plate[123, 136, 192]. However, evidence for short stature is not clearly identified in our investigations of MPS IX mice. The absence of thickened digits and broadened long bone structures by X-ray analysis also indicates that any effects due to HA accumulation in the growth plate of MPS IX mice is minimal. However, a complete characterization of the structure and closing of the epiphyseal plate in MPS IX mice may reveal subtle defects that do not result in a gross phenotype and may be useful in studying the early pathogenic events of MPS disorders.

Given the high turnover rate of HA in the joint, it is not surprising that the joint is the principal site of HA accumulation in the absence of Hyal1. HA

concentrations in human articular cartilage range from 0.5- 2.5 μg/mg of tissue wet weight and the synovial fluid contains one of the highest HA concentrations found in the body (1400-3600 μg/g)[20, 193]. In the rabbit, synovial fluid HA has been estimated to have a half-life of 0.5 – 1 day and the majority of degradation occurs locally in the cartilage and synovium[56, 194, 195]. Human and mouse articular chondrocytes express the three most broadly distributed hyaluronidases, *HYAL1/Hyal1*, *HYAL2/Hyal2* and *HYAL3/Hyal3*[196-199]. Yet only Hyal1 appears to be essential to HA turnover in the joint to date, as Hyal3 deficient mice do not display premature articular cartilage proteoglycan loss (Triggs-Raine et al., unpublished data). It will be interesting to examine Hyal2 deficient mice to determine the contribution of Hyal2 to the turnover of HA in the joint.

Increases in tissue GAG content correlate with storage in mouse models of MPS IIIA and MPS IIIB, yet we found no evidence of non-skeletal GAG accumulation in MPS IX mice[143, 186]. The cellular HA storage in human MPS IX, identifiable as vacuolation using light and electron microscopy, is not detected in murine MPS IX. Furthermore, no detectable differences in the HA content of skin from MPS IX mice was identified. Overall, this suggests that mice may differ in the production and/or turnover of HA. If such differences exist, this could explain the higher circulating serum HA concentrations in mice (88-1136 ng/ml) than in humans (25-75 ng/ml). Species-specific differences in GAG distribution and synthesis have been described previously in the mouse, therefore it is conceivable that species-specific differences in HA turnover may also exist[200]. Therefore, further investigations in the production and turnover of HA in the mouse system are essential

in determining the full use of the mouse as a model organism.

Chapter 6: Examining compensatory mechanisms

Acknowledgements:

Hexosaminidase assays of liver lysates were performed by Rick Hemming. A portion of the research presented in this chapter is in a manuscript accepted by the journal of Human Molecular Genetics and is currently in press.

6.1 Introduction

Given the biological importance and abundance of HA, the mild phenotype associated with both murine and human MPS IX suggested that other hyaluronidases may compensate for a Hyal1 deficiency. The absence of detectable HA accumulation in the serum and non-skeletal tissues of the *Hyal1* null mouse led us to re-examine the differences between mouse and human hyaluronidase genes. Although the tissue distribution is unique to each hyaluronidase gene, mouse *Hyal2* and *Hyal3* genes display expression patterns relatively similar to *Hyal1* and are the likely candidate genes to compensate in a Hyal1 deficiency. Additionally mouse *Hyal3* demonstrates a slightly broader expression than in humans, being found in the liver and kidney the main organs that degrade circulating HA[58, 100]. While tissue HA may be degraded locally, lymphatic uptake and removal constitutes the majority of HA degradation[54, 55]. Therefore, this broader *Hyal3* expression may explain the absence of elevated circulating HA levels in the mouse. However, additional differences in the hyaluronidase genes exist between mice and humans, as mouse *HyalP1* encodes a functional protein and the rodent system contains an additional *Hyal5* gene[101, 119].

The importance of related catabolic mechanisms in HA degradation are also not well established. Related degradative pathways have been shown previously to cause species-specific differences in degradative mechanisms as seen in the mouse model of Tay-Sachs disease. In the murine model of Tay-Sachs disease, *HexA* null mice displayed no gross neurological abnormalities due to compensation in GM2 ganglioside degradation by a sialidase enzyme in a related degradative pathway[189, 201].

The exoglycosidases are known to function on small fragments of HA produced by hyaluronidase digestion. However, *in vitro* activity assays have shown that the exoglycosidases are capable of degrading high molecular weight HA[124]. This is also suggested *in vivo* where mice deficient in all lysosomal β-hexosaminidase forms have demonstrated MPS-like phenotypes and HexB deficient mice have been reported to contain Alcian Blue positive material in brain and visceral organs suggestive of GAG accumulation[121, 122]. While it is plausible that the accumulating GAG products may be the accumulation of other GAG components, the exoglycosidases are found in high abundance within cells and their contribution to HA degradation remains to be determined.

Therefore, we sought to determine possible mechanisms of compensation by examining the transcript abunbance or activity of the hyaluronidases and exoglycosidases in *Hyal1* -/- mice. This chapter describes the quantitative analyses of the mRNA abundance of the hyaluronidases and an exoglycosidase, *HexB*, which encodes the β-subunit of the major hexosaminidase isoenzymes, HexA and HexB. Although Hyal2 and Hyal3 genes are the most likely to compensate in a Hyal1 deficiency, we examined the transcript abundance of all the mouse hyaluronidase genes due to their unknown functions, species specific differences and recent reports of low levels of *SPAM1* expression in fibroblasts[202]. These studies would identify genes that may compensate for mouse and/or human MPS IX. In addition, this chapter describes the examination of hyaluronidase transcript abundance in human MPS IX fibroblasts to identify possible compensatory enzymes in human MPS IX. These studies will facilitate the design of further investigations to determine the

compensatory hyaluronidase genes and would suggest the contribution the exoglycosidases may play in HA degradation.

6.2 Results

6.2.1 Hyaluronidase expression

6.2.1.1 Liver

The gene expression of *Hyal2*, *Hyal3*, *Hyal5*, *HyalP1* and *Spam1* were examined in liver mRNA from *Hyal1* +/+ mice. *Hyal2*, *Hyal3* and *HyalP1* were transcribed in the liver, yet the abundance of *HyalP1* transcript was not enough to reliably quantitate and compare between +/+ and -/- animals. Therefore, the levels of the *Hyal2* and *Hyal3* transcripts was examined in the liver mRNA of 3 or 6 month male +/+ and -/- mice (Figure 34A). The abundance of *Hyal2* transcript did not differ between +/+ and -/- mice, however the level of *Hyal3* showed an increase that ranged from 4.3 to 7.4 fold in the three separate male mice sets examined. This resulted in a statistically significant (P=0.001; n=3) elevation of *Hyal3* expression with an overall mean of 5-fold.

6.2.1.2 Testes, kidney and lung

Preliminary examination of the expression of the hyaluronidase genes in testes (n=2), kidney (n=1) and lung (n=1) tissues were performed on 6 month male age-matched pairs. *Hyal2*, *Hyal3*, *Hyal4*, *Hyal5*, *HyalP1* and *Spam1* were all found to be expressed in the testes of mice. The expression of these genes were compared

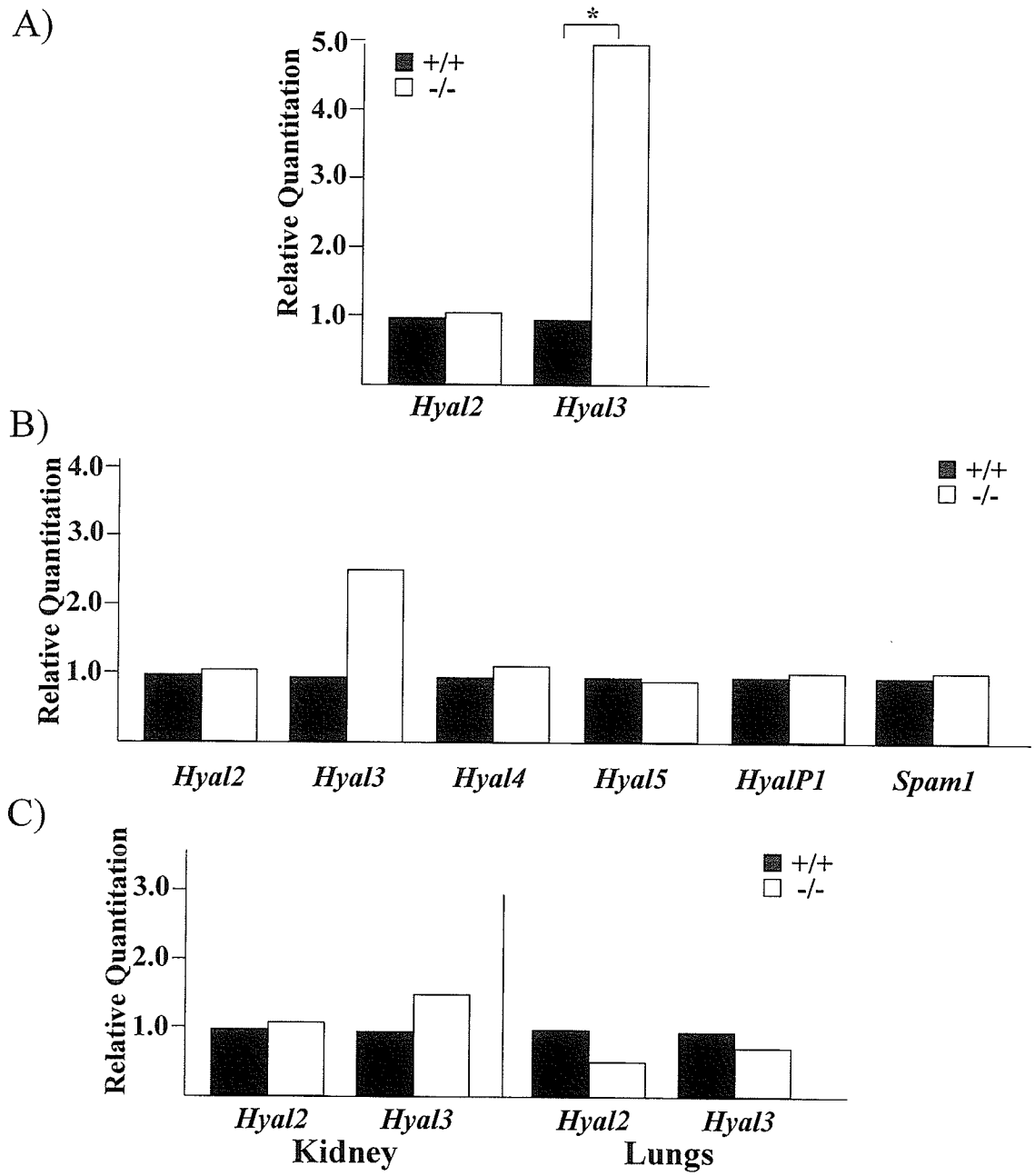

Figure 34: The mRNA abundance of the hyaluronidase genes in the liver, testes, kidney and lungs of *Hyal1* +/+ and -/- mice.

The mRNA abundance of the hyaluronidase genes of wild-type (+/+) and null (-/-) mice at 3-6 months of age in the liver (n=3; panel A) or testes (n=2; panel B) was quantitated by real-time PCR. RNA abundance is displayed as an average fold change of -/- mice when compared to +/+ levels. *Hyal3* mRNA levels were consistently elevated in -/- mice in comparison to +/+ age-matched controls in both the liver and the testes. The transcript abundance of *Hyal3* in the mRNA of kidney or total RNA of lung of -/- mice (n=1; panel C) detected a only milder elevation of *Hyal3* in the kidney. No differences in any other hyaluronidase genes were identified in any of the tissues examined. The * denotes statistically significant differences when examined using a Pair-Wise Fixed Reallocation Randomization Test.

between *Hyal1* +/+ and *Hyal1* -/- mice and no difference in the expression of *Hyal2*, *Hyal4*, *Hyal5*, *HyalP1* and *Spam1* were found (Figure 34B). The *Hyal3* transcript levels were elevated by 2.0-fold and 3.2-fold in the two sets of male mice examined, resulting in a mean 2.6-fold increase of the *Hyal3* transcript in the testes (Figure 34B).

The gene expression of *Hyal2*, *Hyal3*, *Hyal4*, *Hyal5*, *HyalP1* and *Spam1* were examined in kidney mRNA. *Hyal2*, *Hyal3*, *Hyal4*, *Hyal5* and *HyalP1* were expressed in the kidney, however only the levels of *Hyal2* and *Hyal3* were in sufficient quantities to compare their mRNA levels between *Hyal1* +/+ and -/- mice. Upon examination, no increase in the *Hyal2* transcript abundance was found, while the level of the *Hyal3* transcript was only mildly elevated by 1.5-fold (Figure 34C).

The abundance of the *Hyal2* and *Hyal3* transcripts were also examined in the lung total RNA of *Hyal1* +/+ and -/- mice. *Hyal2* and *Hyal3* transcripts were found at an abundance that could allow accurate quantitation and comparison between *Hyal1* +/+ and *Hyal1* -/- mice. No difference in the mRNA levels of *Hyal2* and *Hyal3* was found between +/+ and -/- mice in lung total RNA (n=1; Figure 34C).

6.2.2 Compensation by exoglycosidases

6.2.2.1 HexB expression

The transcript levels of *HexB* was examined in the liver and testes mRNA, the two tissues that displayed the greatest elevation in the abundance of the *Hyal3* transcript. Upon comparison of *HexB* mRNA levels in *Hyal1* +/+ and *Hyal1* -/- mice

at 3 or 6 months of age, no detectable difference was found in testes (n=2) or liver mRNA (n=3) (Figure 35A).

6.2.2.2 Hexosaminidase activity

The total hexosaminidase activity was examined in the livers of *Hyal1* +/+ and *Hyal1* -/- mice to verify quantitative expression results. Mice that were 12 months of age were used for these studies to ensure up-regulation of hexosaminidase was not seen at more advanced ages. The total liver hexosaminidase activity of male (60.2 ± 22.7 nM/hr/mg; n=8) and female animals (102.6 ± 22.7 nM/hr/mg; n=8) did not significantly differ (P=0.21). Therefore, analyses were performed between genotypes independently and by pooling male and female activities (Figure 35B). The hexosaminidase activity of +/+ (62.9 ± 22.7 nM/hr/mg; n=8) and -/- (99.8 ± 22.7 nM/hr/mg; n=8) mice did not differ (P=0.27) when the sexes were combined for analysis. Additionally, the hexosaminidase activity of male +/+ (26.5 ± 32.1 nM/hr/mg; n=4) and -/- (93.9 ± 32.1 nM/hr/mg; n=4) mice, as well as female +/+ (99.4 ± 32.1 nM/hr/mg; n=4) and -/- (105.7 ± 32.1 nM/hr/mg; n=4) mice, also did not significantly differ (P= 0.36).

6.2.3 Hyaluronidase expression in human MPS IX

The elevation in the abundance of the *Hyal3* transcript in the kidney, testes and liver RNA of -/- mice, prompted us to examine the expression of hyaluronidases in human MPS IX. The abundance of the *HYAL2* and *HYAL3* transcripts were examined in total RNA from human MPS IX patient fibroblasts and 4 unaffected

A)

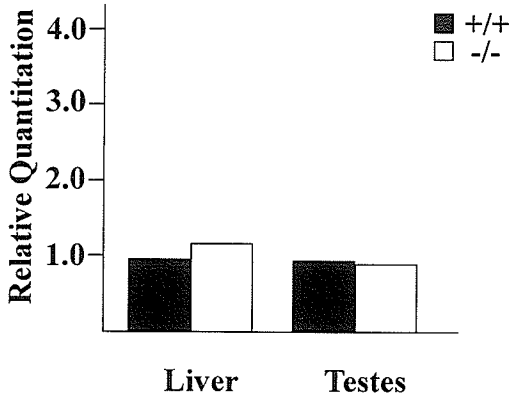

B)

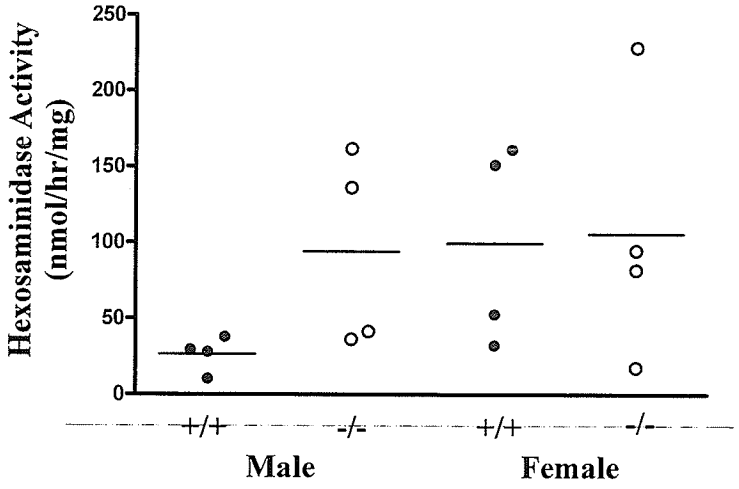

Figure 35: *HexB* transcript abundance in the liver or testes and the total hexosaminidase activity in the liver of *Hyal1* +/+ and -/- mice.
The abundance of the *HexB* transcripts was quantitated in the mRNA from the testes (n=2) and liver (n=3) of +/+ and -/- mice at 3-6 months of age by real-time PCR (A). The mRNA abundance is displayed as the fold change of -/- mice in comparison to age-matched +/+ mice. The total β-hexosaminidase activity of liver lysates from +/+ and -/- mice of 12 month old mice (n=4) was examined by activity assays normalized to lysate protein levels (B). No statistically significant differences in either the *HexB* transcript abundance or the total hexosaminidase activity in the liver was identified in -/- mice.

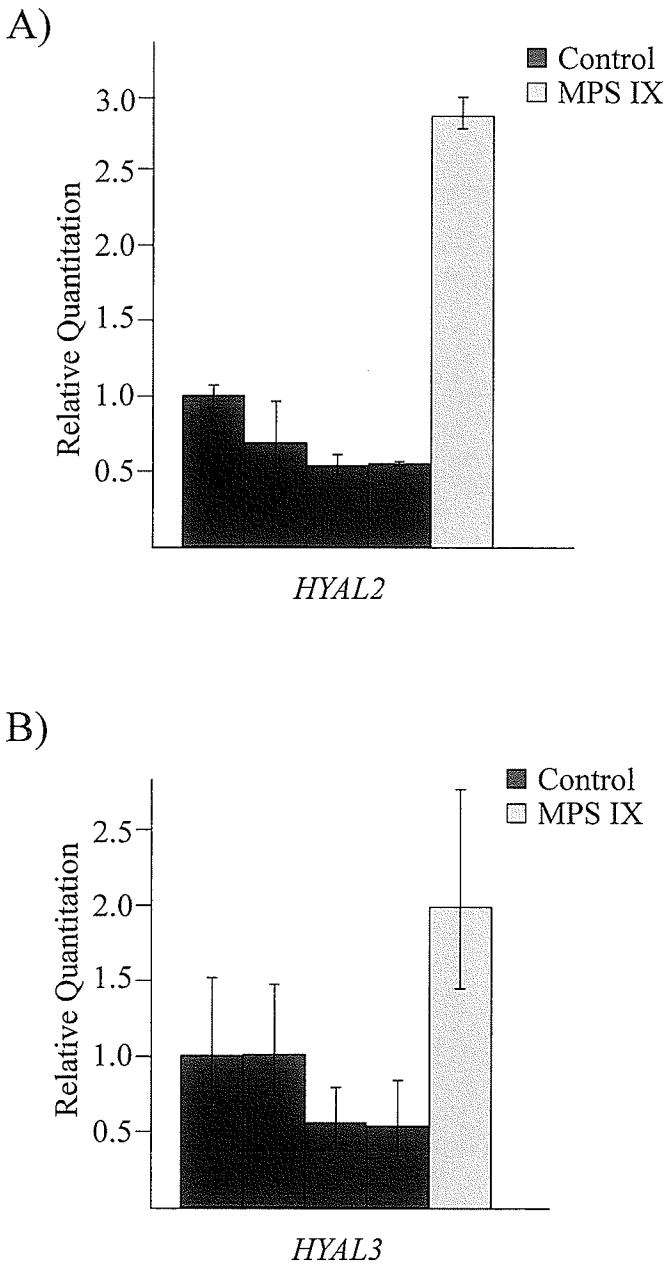

Figure 36: *HYAL2* and *HYAL3* transcript abundance in the fibroblasts from a MPS IX patient and unaffected controls.
The abundance of the *HYAL2* (A) and *HYAL3* (B) transcripts were quantitated by real-time PCR in the total RNA from fibroblasts of an MPS IX patient and unaffected controls. The transcript abundance is shown as the fold change of the MPS IX patient in in comparison to a randomly selected normal fibroblast cell line. Elevatios of both *HYAL2* and *HYAL3* transcripts were identified in the MPS IX patient fibroblast cell line in comparison to the unaffected controls.

controls. Upon comparison with controls, the level of *HYAL2* and *HYAL3* transcripts were elevated in the human MPS IX fibroblasts (Figure 36). The level of *HYAL3* mRNA displayed a relative 2-fold increase, whereas the *HYAL2* mRNA levels displayed a larger 2.8 fold relative increase in fibroblasts from the MPS IX patient.

6.3 Discussion

Upon examination of the major hyaluronidases in the liver, testes, kidney and lung, only the level of *Hyal3* transcript was elevated in the liver, testes and kidney of -/- mice suggesting it is the main gene to compensate in a Hyal1 deficiency. Preliminary analysis of *Hyal3* transcript abundance in the kidney suggested a relatively mild 1.5 fold elevation; however the testes and liver displayed larger 2.6- and 5.0-fold elevations respectively. The tissue specific differences in the fold increase may indicate where Hyal1 plays a more significant role in HA degradation. In addition, the absence of any detectable elevation of *Hyal3* mRNA in preliminary analysis of the lung hyaluronidase gene expression suggests that either HA turnover does not proceed at a high rate in the lungs or that Hyal1 has little function in lung HA degradation. No detectable differences in the mRNA levels of the other hyaluronidases examined were found in *Hyal1* -/- mice. *Hyal2* transcipt levels in the liver, testes, kidney or lung of *Hyal1* -/- male mice were normal. Additionally, the *HyalP1*, *Spam1*, *Hyal4* or *Hyal5* abundance in the testes were normal. Interestingly, *Hyal4*, *Hyal5*, *HyalP1* and *Spam1* gene expression was broader than originally anticipated, being found at extremely low levels in more visceral organs. However,

these levels were too low to reliably quantitate without the use of pre-amplification systems and the biological relevance to this expression remains to be determined.

While *Hyal3* was the only hyaluronidase gene identified to be up-regulated in mice, the mRNA abundance of *HYAL2* and *HYAL3* was elevated in human fibroblasts from an MPS IX patient. Interestingly, the increase in *HYAL2* transcripts was larger than that identified for *HYAL3*. Fibroblasts of biopsies of skin masses from the MPS IX patient displayed an accumulation of HA; however we could not detect an accumulation in the serum or non-skeletal tissues of the murine MPS IX model[19]. The elevated levels of both *HYAL2* and *HYAL3* transcripts may reflect a difference in the cellular response to increased HA accumulation. It is interesting to note the higher degree of *Hyal3* elevation in mouse liver compared to the human fibroblasts. It would be necessary to examine the *Hyal3* transcript abundance in a mouse fibroblast line to determine if the differences are due to tissue specific transcriptional control. These studies may elucidate if the transcriptional regulation of *HYAL3* in humans is different than in mice. Alternatively, the large increase in the *Hyal3* transcript seen in the mouse liver may also represent a preliminary response in the mouse due to smaller amounts of accumulation that is altered upon up-regulation of additional hyaluronidase genes.

The ability of the hexosaminidase enzymes, one of the major exoglycosidases, to compensate in a deficiency of Hyal1 was also examined. Analysis of the mRNA levels of a major hexosaminidase gene, HexB and the total hexosaminidase activity of *Hyal1* +/+ and -/- mice could detect no significant differences suggesting the exoglycosidases do not play a major compensating role in a Hyal1 deficiency.

However, *HexB* is found at higher levels in comparison to hyaluronidases and the hexosaminidase enzymes are abundant in degradative cells. Therefore, eliminating the function of the exoglycosidases in Hyal1 deficient mice or cell lines is necessary to determine their contribution to HA degradation.

Chapter 7: Discussion and Future Directions

As described in Chapter 1, most MPS disorders display severely impaired joint structures and/or mobility, speech difficulties, neurological impairment and large amounts of GAG storage in various organs and cells[9]. The phenotype of the MPS IX patient is relatively mild in comparison to other MPS disorders and the major clinical difficulties include painful periarticular masses and acetabular erosions[19]. Identification of the proteoglycan loss, as well as other degenerative abnormalities, in the joints of MPS IX mice support the previous description indicating that joint defects are the main phenotypic characteristics of MPS IX. However, the absence of non-skeletal HA elevations, described in Chapter 5, indicate that the mouse model is milder than the human disorder. A more careful comparison of the mouse and human disease phenotype is shown in Table 6.

Table 6: Comparison of the mouse and human MPS IX phenotypes and/or potential compensatory enzymes.

Tissue / potential compensatory enzymes	**Human MPS IX**	**Mouse MPS IX**
skeletal system and/or joint structure abnormalities	acetabular erosions, popliteal cysts	proteoglycan loss indicative of degenerative joint disease
	mild short stature	no stature differences
	nodular synovium	changes in synovium not determined
	undetermined	HA accumulation in articular cartilage
Serum	36-84 fold HA elevations	no HA elevations identified
Skin	HA storage in fibroblasts and macrophages	no HA storage identified
high turnover tissues – liver, kidney, lymph nodes	undetermined	no HA storage identified
potential compensatory enzymes	elevated HYAL2 and HYAL3 transcripts in fibroblasts	elevated levels of Hyal3 transcripts in the liver

The full range of human MPS IX disease symptoms has yet to be described, as only one patient has been clinically identified to date. However, the murine and human MPS IX phenotype has identified synovial joint involvement in the disease. The abnormalities identified in the murine model are relatively mild in comparison to other MPS disorders that affect joint function. X-ray analysis did not identify differences in the skeletal structures of *Hyal1* -/- mice and preliminary gait analysis detected no abnormalities in joint function. However, the use of other technologies, such as computed tomography or magnetic resonance imaging and a more extensive examination of gait differences would better determine how the degenerative changes impact joint function.

MPS disorder phenotypes have not been limited to synovial joints, but also include fibrous or cartilaginous joints of the cranio-facial and/or vertebral skeleton[14]. My studies in the mouse MPS IX model have only examined the synovial joint to date and whether other joint types are the involved types remains to be determined. The murine model described in this thesis is a tool to assess the presence of additional skeletal defects. Therefore, further studies, such as a closer examination of fibrous joints in the skull and cartilaginous joints in the vertebrae, might identify additional MPS IX symptoms.

While I cannot exclude that MPS IX is an extremely rare disorder, the phenotype described in the MPS IX patient may be on the more severe side of the disease spectrum. Given the total absence of activity in this patient, patients with mutations that only partially impair HYAL1 activity may display attenuated symptoms that present only as degenerative joint disease[19]. Genetic screening of

patients showing inherited degenerative joint disease at early ages, such as osteoarthritis, could identify additional MPS IX patients. This would be beneficial to determine the best treatment options for individuals, since the cross-linked forms of HA (Synvisc®, Hyalgan®) are commonly injected into the knees of osteoarthritis patients to alleviate pain[203]. The continued use of Synvisc® and/or Hyalgan® may worsen disease symptoms and studies using the mouse model of MPS IX would be useful for determining the effects of repeated HA injections in a Hyal1 deficiency.

My studies have determined that HA accumulation is associated with pathogenic changes that result in degenerative joint disease (Chapter 5). However, the next step is to identify the specific pathogenic changes as a result of this accumulation. The pathogenic changes resulting from GAG accumulation have largely been ignored to date. Yet the investigation of pathogenic abnormalities is of increasing importance to to be able to treat patients with available enzyme replacement therapies as early as possible. To identify changes for MPS IX, *Hyal1* -/- mice should be examined for changes in collagen content and ECM components of the cartilage, chondrocyte proliferation and/or differentiation rates, as well as the examination of synovial membranes and surrounding areas for enhanced cell infiltrations or synovial fibroblast proliferations occurring during inflammatory responses. All of these aspects have been previously associated with the pathogenesis of degenerative joint diseases such as osteoarthritis and would yield information about the mechanism of degeneration[184].

Information on the pathogenic changes that result from GAG accumulation in the joints of MPS VI animal models showed that articular chondrocytes underwent

higher rates of apoptosis[137]. Chondrocytes from MPS VI animals secrete increased levels of nitric oxide and tumor necrosis factor-α, signaling molecules that could be stimulated in control chondrocytes by dermatan sulfate and/or lipopolysaccharide [137]. This suggested that the chondrocyte apoptosis in MPS VI animals was mediated by dermatan sulfate induced signaling using similar mechanisms as lipopolysaccharide. Lipopolysaccharide signaling is known to occur by Toll-like receptors that stimulate inflammatory responses (for review of Toll-like receptor signaling [204]). Furthermore, HA has been shown to stimulate cytokine production, specifically tumor necrosis factor-α and macrophage inflammatory protein-2, by Toll-like receptors 2 and 4 in peritoneal macrophages[93]. The accumulation of HA may have similar pathogenic effects mediated by Toll-like receptors, which increase inflammatory changes within the cartilage. Future investigations could examine this possibility by determining the inflammatory cytokines present in the blood and cartilage, as well as differences in Toll-like receptor signaling in MPS IX mice. These studies would explore a mechanism for HA induced osteoarthritic changes shown in MPS IX mice.

The study of HA turnover and the role of the individual hyaluronidases in this process is not well understood. This has been an area of intense focus in the field since the identification of six related hyaluronidase genes, along with their unique expression profiles, that suggested they may have slightly differing tissue specific roles[99]. However, their activities and substrate specificities have been difficult to establish to date due to the low levels of gene expression and insensitive enzymatic assays. The use of overexpression systems demonstrated the activities of the two forms of HYAL2[106, 108, 109], but has yielded conflicting results with other genes such

as HYAL3/Hyal3 (See below)[109, 111]. Additionally, overexpression of HyalP1 resulted in no detectable activity, which contradicts endogenous studies where HyalP1 was suggested to have redundant functions to Ph-20 due to its activity in cumulus cell dispersal[118, 120]. The ability of the hyaluronidases to degrade HA is only established in Hyal1, Hyal2, Hyal5 and Ph-20 by the current methods and the individual contribution of the hyaluronidases to HA turnover in different tissues has not yet been determined.

Mouse models of deficiency, along with examination of tissue GAG content, was an essential first step to separate the tissue specific roles of the hyaluronidases in HA turnover. My studies detected no significant elevations in non-skeletal tissues in the mouse model of Hyal1 deficiency, although I cannot exclude the possibility of minor accumulations that may be evident with larger sample sizes. Therefore, it appears that Hyal1 plays a minor role at best in tissue HA turnover and that other enzymes are responsible for the majority of non-skeletal HA degradation. In the context of the proposed model of HA degradation presented in the introduction of this thesis (Chapter 1, Figure 5), this suggests that alternative enzymes such as other hyaluronidases and/or the exoglycosidases compensate in the degradation of intracellular HA fragments.

Attempting to identify genes that may play compensatory roles to Hyal1 or function as a major contributor in tissue HA degradation, I examined the abundance of hyaluronidases and an exoglycosidase in mouse MPS IX tissues (Chapter 6). The elevation of *Hyal3* transcripts detected in the liver of *Hyal1* -/- mice, and in preliminary analyses of the testes and kidney, is interesting given the controversy

regarding the activity of Hyal3. Overexpression studies have been unable to detect Hyal3 activity, however acidic activity has been described by *in vitro* transcription and translation studies[109, 111]. Thus it is plausible that post-translational modification of this enzyme may regulate its activity and as a result Hyal3 displays activity only in certain cell types. In addition, isolation methods or assays for hyaluronidase activity may not be optimal to display the sensitivity required to detect Hyal3 activity. Thus the relationship between Hyal1 and Hyal3 cannot be fully answered until a cell or animal model deficient in both Hyal1 and Hyal3 is produced. These future studies should define the extent of Hyal3 compensation to HA degradation in a Hyal1 deficiency.

The up-regulation of *HYAL2* identified in human MPS IX fibroblasts (Chapter 6) suggests HYAL2 as another compensatory enzyme. While this up-regulation of *Hyal2* was not identified in the liver or other organs of the murine model of MPS IX, the phenotype of the MPS IX mice was much milder than the human counterpart and may explain the absence of any differences in mouse *Hyal2* expression. Therefore, we cannot exclude that the Hyal1 and Hyal2 enzymes have similar roles in tissue HA degradation at this time. Given the relatively high expression of *HYAL2* in all tissues and the acidic activity of the soluble form of the enzyme, HYAL2 is a strong candidate to compensate in a HYAL1 deficiency[99]. Studies on the phenotype of Hyal2 deficient mice will provide definitive information regarding the enzyme's ability to function similarly to Hyal1. Therefore, future comparisons of the phenotype of Hyal1, Hyal2 and Hyal3 deficient mice and mice deficient in various combinations of these genes may determine enzymes with compensatory roles.

The mouse is a useful tool to determine potential compensatory enzymes in future studies, however the high circulating levels of HA identified in these and other studies[205, 206] may reflect differences present in the mouse either in the synthesis and/or degradation of HA. Such differences have been documented previously with synthesis of other GAGs, such as keratan sulfate, in the mouse system[207]. An alternative explanation is that the co-transcripts of *Hyal1*, generated by alternative splicing of polycistronic messages in the mouse system[100], would reduce the contribution of blood filtering organs to remove circulating HA. These transcripts result in the deletion of the C-terminal portion of the Hyal1 that may regulate the levels of activity by altering protein conformation or localization. Therefore, further comparisons are required to determine the differences between the mouse and human and our ability to extrapolate experimental conclusions between the two systems.

Overall, my research work has initiated future investigations to identify the tissue contributions of each of the hylauronidases. Similar studies in mice deficient in other hyaluronidases will identify tissues where each hyaluronidase is most important in constitutive HA turnover. However, this research has not begun to identify the redundancies between the genes or when Hyal1 is essential in disease processes, such as cancer or tissue injury, where the degradation of HA requires a more regulated mechanism. Much more work is needed to identify the contribution of the hyaluronidases to both regulated and constitutive HA degradation. The upcoming years in hyaluronidase research will be exciting and reveal great insights into the role of the hyaluronidases in HA metabolism and different disease processes.

References

1. Wraith,J.E. Lysosomal disorders. *Semin. Neonatol.* **7**, 75-83 (2002).

2. Vellodi,A. Lysosomal storage disorders. *Br. J. Haematol.* **128**, 413-431 (2005).

3. Futerman,A.H. & van,M.G. The cell biology of lysosomal storage disorders. *Nat. Rev. Mol. Cell Biol.* **5**, 554-565 (2004).

4. Brady,R.O., Kanfer,J.N., Bradley,R.M., & Shapiro,D. Demonstration of a deficiency of glucocerebroside-cleaving enzyme in Gaucher's disease. *J. Clin. Invest* **45**, 1112-1115 (1966).

5. Brady,R.O., Kanfer,J.N., & Shapiro,D. Metabolism of glucocerebrisidases. II. Evidence of an enzymatic deficiency in Gaucher's disease. *Biochem. Biophys. Res. Commun.* **18**, 221-225 (1965).

6. DeDuve,C., Pressman,B.C., Gianetto,R., Wattiaux,R., & Ppelmans,F. Tissue fractionation studies. 6. Intracellular distribution patterns of enzymes in rat-liver tissue. *Biochem. J.* **60**, 604-617 (1955).

7. Gieselmann,V. Lysosomal storage diseases. *Biochim. Biophys. Acta* **1270**, 103-136 (1995).

8. Conzelmann,E. & Sandhoff,K. Partial enzyme deficiencies: residual activities and the development of neurological disorders. *Dev. Neurosci.* **6**, 58-71 (1983).

9. Neufeld,E.F. & Muenzer,J. The Mucopolysaccaridoses in *The Metabolic and Molecular Mechanisms of Inherited Disease* (eds. Scriver,C., Beaudet A, Sly W & Valle D) 3421-3452 (McGraw-Hill, New York, 2001).

10. Meikle,P.J., Hopwood,J.J., Clague,A.E., & Carey,W.F. Prevalence of lysosomal storage disorders. *JAMA* **281**, 249-254 (1999).

11. Muenzer,J. The mucopolysaccharidoses: a heterogeneous group of disorders with variable pediatric presentations. *J. Pediatr.* **144**, S27-S34 (2004).

12. Roberts,S.H., Upadhyaya,M., Sarfarazi,M., & Harper,P.S. Further evidence localising the gene for Hunter's syndrome to the distal region of the X chromosome long arm. *J. Med. Genet.* **26**, 309-313 (1989).

13. Klein,U., Kresse,H., & Von Figura,K. Sanfilippo syndrome type C: deficiency of acetyl-CoA:alpha- glucosaminide N-acetyltransferase in skin fibroblasts. *Proc. Natl. Acad. Sci. U. S. A* **75**, 5185-5189 (1978).

14. Wraith,J.E. The mucopolysaccharidoses: a clinical review and guide to management. *Arch. Dis. Child* **72**, 263-267 (1995).

15. Wraith,J.E. *et al.* Enzyme replacement therapy for mucopolysaccharidosis I: a randomized, double-blinded, placebo-controlled, multinational study of recombinant human alpha-L-iduronidase (laronidase). *J. Pediatr.* **144**, 581-588 (2004).

16. Muenzer,J. *et al.* A phase II/III clinical study of enzyme replacement therapy with idursulfase in mucopolysaccharidosis II (Hunter syndrome). *Genet. Med.* **8**, 465-473 (2006).

17. Harmatz,P. *et al.* Enzyme replacement therapy for mucopolysaccharidosis VI: a phase 3, randomized, double-blind, placebo-controlled, multinational study of recombinant human N-acetylgalactosamine 4-sulfatase (recombinant human arylsulfatase B or rhASB) and follow-on, open-label extension study. *J. Pediatr.* **148**, 533-539 (2006).

18. Clarke,L.A. The mucopolysaccharidoses: a success of molecular medicine. *Expert. Rev. Mol. Med.* **10**, e1 (2008).

19. Natowicz,M.R. *et al.* Clinical and biochemical manifestations of hyaluronidase deficiency. *New Engl. J. Med.* **335**, 1029-1033 (1996).

20. Fraser,J.R.E., Laurent,T.C., & Laurent,U.B.G. Hyaluronan: its nature, distribution, functions and turnover. *J. Int. Med.* **242**, 27-33 (1997).

21. Prydz,K. & Dalen,K.T. Synthesis and sorting of proteoglycans. *J. Cell Sci.* **113 Pt 2**, 193-205 (2000).

22. Prabhakar,V. & Sasisekharan,R. The biosynthesis and catabolism of galactosaminoglycans. *Adv. Pharmacol.* **53**, 69-115 (2006).

23. Sundblad,G., Holojda,S., Roux,L., Varki,A., & Freeze,H.H. Sulfated N-linked oligosaccharides in mammalian cells. II. Identification of glycosaminoglycan-like chains attached to complex-type glycans. *J. Biol. Chem.* **263**, 8890-8896 (1988).

24. Triggs-Raine,B., Salo,T.J., Zhang,H., Wicklow,B.A., & Natowicz,M.R. Mutations in HYAL1, a member of a tandemly distributed multigene family encoding disparate hyaluronidase activities, cause a newly described lysosomal disorder, mucopolysaccharidosis IX. *Proc. Natl. Acad. Sci. U. S. A* **96**, 6296-6300 (1999).

25. Arming,S., Strobl,B., Wechselberger,C., & Kreil,G. In vitro mutagenesis of PH-20 hyaluronidase from human sperm. *Eur. J. Biochem.* **247**, 810-814 (1997).

26. Weissmann,B., Rapport,M.M., Linker,A., & Meyer,K. Isolation of the aldobionic acid of umbilical cord hyaluronic acid. *J. Biol. Chem.* **205**, 205-211 (1953).

27. Rapport,M.M., Weissmann,B., Linker,A., & Meyer,K. Isolation of a crystalline disaccharide, hyalobiuronic acid, from hyaluronic acid. *Nature* **168**, 996-997 (1951).

28. Scott,J.E. Secondary structures in hyaluronan solutions: chemical and biological implications. *Ciba Found. Symp.* **143**, 6-14 (1989).

29. Reed,R.K., Lilja,K., & Laurent,T.C. Hyaluronan in the rat with special reference to the skin. *Acta Physiol. Scand.* **134**, 405-411 (1989).

30. Day,A.J. & Prestwich,G.D. Hyaluronan-binding proteins: tying up the giant. *J. Biol. Chem.* **277**, 4585-4588 (2002).

31. Zhao,M. *et al.* Evidence for the covalent binding of SHAP, heavy chains of inter-alpha-trypsin inhibitor, to hyaluronan. *J. Biol. Chem.* **270**, 26657-26663 (1995).

32. Hess,K.A., Chen,L., & Larsen,W.J. Inter-alpha-inhibitor binding to hyaluronan in the cumulus extracellular matrix is required for optimal ovulation and development of mouse oocytes. *Biol. Reprod.* **61**, 436-443 (1999).

33. Knudson,C.B. & Knudson,W. Hyaluronan-binding proteins in development, tissue homeostasis, and disease. *FASEB J.* **7**, 1233-1241 (1993).

34. Day,A.J. & de la Motte,C.A. Hyaluronan cross-linking: a protective mechanism in inflammation? *Trends Immunol.* **26**, 637-643 (2005).

35. de la Motte,C.A., Hascall,V.C., Drazba,J., Bandyopadhyay,S.K., & Strong,S.A. Mononuclear leukocytes bind to specific hyaluronan structures on colon mucosal smooth muscle cells treated with polyinosinic acid:polycytidylic acid: inter-alpha-trypsin inhibitor is crucial to structure and function. *Am. J. Pathol.* **163**, 121-133 (2003).

36. Majors,A.K. *et al.* Endoplasmic reticulum stress induces hyaluronan deposition and leukocyte adhesion. *J. Biol. Chem.* **278**, 47223-47231 (2003).

37. Philipson,L.H., Westley,J., & Schwartz,N.B. Effect of hyaluronidase treatment of intact cells on hyaluronate synthetase activity. *Biochem.* **24**, 7899-7906 (1985).

38. Deangelis,P.L. Hyaluronan synthases: fascinating glycosyltransferases from vertebrates, bacterial pathogens, and algal viruses. *Cell Mol. Life Sci.* **56**, 670-682 (1999).

39. Kumari,K. & Weigel,P.H. Identification of a membrane-localized cysteine cluster near the substrate-binding sites of the Streptococcus equisimilis hyaluronan synthase. *Glycobiology* **15**, 529-539 (2005).

40. Jing,W. & Deangelis,P.L. Analysis of the two active sites of the hyaluronan synthase and the chondroitin synthase of Pasteurella multocida. *Glycobiology* **13**, 661-671 (2003).

41. Jing,W. & Deangelis,P.L. Dissection of the two transferase activities of the Pasteurella multocida hyaluronan synthase: two active sites exist in one polypeptide. *Glycobiology* **10**, 883-889 (2000).

42. Spicer,A.P. *et al.* Chromosomal localization of the human and mouse hyaluronan synthase genes. *Genomics* **41**, 493-497 (1997).

43. Itano,N. *et al.* Three isoforms of mammalian hyaluronan synthases have distinct enzymatic properties. *J. Biol. Chem.* **274**, 25085-25092 (1999).

44. Bai,K.J. *et al.* The role of hyaluronan synthase 3 in ventilator-induced lung injury. *Am. J. Respir. Crit Care Med.* **172**, 92-98 (2005).

45. Camenisch,T.D. *et al.* Disruption of hyaluronan synthase-2 abrogates normal cardiac morphogenesis and hyaluronan-mediated transformation of epithelium to mesenchyme. *J. Clin. Invest* **106**, 349-360 (2000).

46. Itano,N. & Kimata,K. Mammalian hyaluronan synthases. *IUBMB. Life* **54**, 195-199 (2002).

47. Heldermon,C., Deangelis,P.L., & Weigel,P.H. Topological organization of the hyaluronan synthase from Streptococcus pyogenes. *J. Biol. Chem.* **276**, 2037-2046 (2001).

48. Tlapak-Simmons,V.L., Baggenstoss,B.A., Clyne,T., & Weigel,P.H. Purification and lipid dependence of the recombinant hyaluronan synthases from Streptococcus pyogenes and Streptococcus equisimilis. *J. Biol. Chem.* **274**, 4239-4245 (1999).

49. Ouskova,G., Spellerberg,B., & Prehm,P. Hyaluronan release from Streptococcus pyogenes: export by an ABC transporter. *Glycobiology* **14**, 931-938 (2004).

50. Prehm,P. & Schumacher,U. Inhibition of hyaluronan export from human fibroblasts by inhibitors of multidrug resistance transporters. *Biochem. Pharmacol.* **68**, 1401-1410 (2004).

51. Schulz,T., Schumacher,U., & Prehm,P. Hyaluronan Export by the ABC Transporter MRP5 and Its Modulation by Intracellular cGMP. *J. Biol. Chem.* **282**, 20999-21004 (2007).

52. Fraser,J.R.E. & Laurent,T.C. Turnover and metabolism of hyaluronan. *Ciba Found. Symp.* **143**, 41-59 (1989).

53. Laurent,T.C. & Fraser,J.R. Hyaluronan. *FASEB J.* **6**, 2397-2404 (1992).

54. Fraser,J.R., Kimpton,W.G., Laurent,T.C., Cahill,R.N., & Vakakis,N. Uptake and degradation of hyaluronan in lymphatic tissue. *Biochem. J.* **256**, 153-158 (1988).

55. Laurent,U.B., Dahl,L.B., & Reed,R.K. Catabolism of hyaluronan in rabbit skin takes place locally, in lymph nodes and liver. *Exp. Physiol* **76**, 695-703 (1991).

56. Laurent,U.B. *et al.* Catabolism of hyaluronan in the knee joint of the rabbit. *Matrix* **12**, 130-136 (1992).

57. Fraser,J.R., Laurent,T.C., Pertoft,H., & Baxter,E. Plasma clearance, tissue distribution and metabolism of hyaluronic acid injected intravenously in the rabbit. *Biochem. J.* **200**, 415-424 (1981).

58. Fraser,J.R., Appelgren,L.E., & Laurent,T.C. Tissue uptake of circulating hyaluronic acid. A whole body autoradiographic study. *Cell Tissue Res.* **233**, 285-293 (1983).

59. Laurent,T.C. *et al.* Urinary excretion of hyaluronan in man. *Scand. J. Clin. Lab Invest* **47**, 793-799 (1987).

60. Prevo,R., Banerji,S., Ferguson,D.J., Clasper,S., & Jackson,D.G. Mouse LYVE-1 is an endocytic receptor for hyaluronan in lymphatic endothelium. *J. Biol. Chem.* **276**, 19420-19430 (2001).

61. Banerji,S. *et al.* LYVE-1, a new homologue of the CD44 glycoprotein, is a lymph-specific receptor for hyaluronan. *J. Cell Biol.* **144**, 789-801 (1999).

62. Zhou,B., Weigel,J.A., Fauss,L., & Weigel,P.H. Identification of the hyaluronan receptor for endocytosis (HARE). *J. Biol. Chem.* **275**, 37733-37741 (2000).

63. Schmits,R. *et al.* CD44 regulates hematopoietic progenitor distribution, granuloma formation, and tumorigenicity. *Blood* **90**, 2217-2233 (1997).

64. Tammi,R. *et al.* Hyaluronan enters keratinocytes by a novel endocytic route for catabolism. *J. Biol. Chem.* **276**, 35111-35122 (2001).

65. Thankamony,S.P. & Knudson,W. Acylation of CD44 and its association with lipid rafts are required for receptor and hyaluronan endocytosis. *J. Biol. Chem.* **281**, 34601-34609 (2006).

66. Teder,P. *et al.* Resolution of lung inflammation by CD44. *Science* **296**, 155-158 (2002).

67. Hayer,S. *et al.* CD44 is a determinant of inflammatory bone loss. *J. Exp. Med.* **201**, 903-914 (2005).

68. Nedvetzki,S. *et al.* RHAMM, a receptor for hyaluronan-mediated motility, compensates for CD44 in inflamed CD44-knockout mice: a different interpretation of redundancy. *Proc. Natl. Acad. Sci. U. S. A* **101**, 18081-18086 (2004).

69. Gale,N.W. *et al.* Normal lymphatic development and function in mice deficient for the lymphatic hyaluronan receptor LYVE-1. *Mol. Cell Biol.* **27**, 595-604 (2007).

70. Huang,S.S. *et al.* CRSBP-1/LYVE-l-null mice exhibit identifiable morphological and functional alterations of lymphatic capillary vessels. *FEBS Lett.* **580**, 6259-6268 (2006).

71. Johnson,L.A., Prevo,R., Clasper,S., & Jackson,D.G. Inflammation-induced uptake and degradation of the lymphatic endothelial hyaluronan receptor LYVE-1. *J. Biol. Chem.* **282**, 33671-33680 (2007).

72. Hansen,B. *et al.* Stabilin-1 and stabilin-2 are both directed into the early endocytic pathway in hepatic sinusoidal endothelium via interactions with clathrin/AP-2, independent of ligand binding. *Exp. Cell Res.* **303**, 160-173 (2005).

73. Harris,E.N., Kyosseva,S.V., Weigel,J.A., & Weigel,P.H. Expression, processing, and glycosaminoglycan binding activity of the recombinant human 315-kDa hyaluronic acid receptor for endocytosis (HARE). *J. Biol. Chem.* **282**, 2785-2797 (2007).

74. Ramsden,C.A. *et al.* A new disorder of hyaluronan metabolism associated with generalized folding and thickening of the skin. *J. Pediatr.* **136**, 62-68 (2000).

75. Toole,B.P. Hyaluronan in morphogenesis. *Semin. Cell Dev. Biol.* **12**, 79-87 (2001).

76. Camenisch,T.D., Schroeder,J.A., Bradley,J., Klewer,S.E., & McDonald,J.A. Heart-valve mesenchyme formation is dependent on hyaluronan-augmented activation of ErbB2-ErbB3 receptors. *Nat. Med.* **8**, 850-855 (2002).

77. Al'Qteishat,A. *et al.* Changes in hyaluronan production and metabolism following ischaemic stroke in man. *Brain* **129**, 2158-2176 (2006).

78. Toole,B.P. Hyaluronan: from extracellular glue to pericellular cue. *Nat. Rev. Cancer* **4**, 528-539 (2004).

79. Turino,G.M. & Cantor,J.O. Hyaluronan in respiratory injury and repair. *Am. J. Respir. Crit Care Med.* **167**, 1169-1175 (2003).

80. Toole,B.P., Wight,T.N., & Tammi,M.I. Hyaluronan-cell interactions in cancer and vascular disease. *J. Biol. Chem.* **277**, 4593-4596 (2002).

81. Wuthrich,R.P. The proinflammatory role of hyaluronan-CD44 interactions in renal injury. *Nephrol. Dial. Transplant.* **14**, 2554-2556 (1999).

82. Anttila,M.A. *et al.* High levels of stromal hyaluronan predict poor disease outcome in epithelial ovarian cancer. *Cancer Res.* **60**, 150-155 (2000).

83. Auvinen,P. *et al.* Hyaluronan in peritumoral stroma and malignant cells associates with breast cancer spreading and predicts survival. *Am. J. Pathol.* **156**, 529-536 (2000).

84. Pirinen,R. *et al.* Prognostic value of hyaluronan expression in non-small-cell lung cancer: Increased stromal expression indicates unfavorable outcome in patients with adenocarcinoma. *Int. J. Cancer* **95**, 12-17 (2001).

85. Lipponen,P. *et al.* High stromal hyaluronan level is associated with poor differentiation and metastasis in prostate cancer. *Eur. J. Cancer* **37**, 849-856 (2001).

86. Posey,J.T. *et al.* Evaluation of the prognostic potential of hyaluronic acid and hyaluronidase (HYAL1) for prostate cancer. *Cancer Res.* **63**, 2638-2644 (2003).

87. Ropponen,K. *et al.* Tumor cell-associated hyaluronan as an unfavorable prognostic factor in colorectal cancer. *Cancer Res.* **58**, 342-347 (1998).

88. Setala,L.P. *et al.* Hyaluronan expression in gastric cancer cells is associated with local and nodal spread and reduced survival rate. *Br. J. Cancer* **79**, 1133-1138 (1999).

89. Decleves,A.E. *et al.* Dynamics of hyaluronan, CD44, and inflammatory cells in the rat kidney after ischemia/reperfusion injury. *Int. J. Mol. Med.* **18**, 83-94 (2006).

90. Melin,J. *et al.* Ischemia-induced renal expression of hyaluronan and CD44 in diabetic rats. *Nephron Exp. Nephrol.* **103**, e86-e94 (2006).

91. George,J. & Stern,R. Serum hyaluronan and hyaluronidase: very early markers of toxic liver injury. *Clin. Chim. Acta* **348**, 189-197 (2004).

92. West,D.C., Hampson,I.N., Arnold,F., & Kumar,S. Angiogenesis induced by degradation products of hyaluronic acid. *Science* **228**, 1324-1326 (1985).

93. Jiang,D. *et al.* Regulation of lung injury and repair by Toll-like receptors and hyaluronan. *Nat. Med.* **11**, 1173-1179 (2005).

94. Sherman,L.S. *et al.* Hyaluronate-based extracellular matrix: keeping glia in their place. *Glia* **38**, 93-102 (2002).

95. Back,S.A. *et al.* Hyaluronan accumulates in demyelinated lesions and inhibits oligodendrocyte progenitor maturation. *Nat. Med.* **11**, 966-972 (2005).

96. Juni,P. *et al.* Efficacy and safety of intraarticular hylan or hyaluronic acids for osteoarthritis of the knee: a randomized controlled trial. *Arthritis Rheum.* **56**, 3610-3619 (2007).

97. Beer,K. A randomized, evaluator-blinded comparison of efficacy of hyaluronic acid gel and avian-sourced hylan B plus gel for correction of nasolabial folds. *Dermatol. Surg.* **33**, 928-936 (2007).

98. Hoffman,D.C. & Duran-Reynals,F. The mechanism of enhancement of infections by testicle extract. *Science* **72**, 508 (1930).

99. Csoka,A., Scherer,S.E., & Stern,R. Expression analysis of six paralogous human hyaluronidase genes clustered on chromosomes 3p21 and 7q31. *Genomics* **60**, 356-361 (1999).

100. Shuttleworth,T.L., Wilson,M.D., Wicklow,B.A., Wilkins,J.A., & Triggs-Raine,B.L. Characterization of the murine hyaluronidase gene region reveals complex organization and cotranscription of Hyal1 with downstream genes, Fus2 and Hyal3. *J. Biol. Chem.* **277**, 23008-23018 (2002).

101. Kim,E. *et al.* Identification of a hyaluronidase, Hyal5, involved in penetration of mouse sperm through cumulus mass. *Proc. Natl. Acad. Sci. U. S. A* **102**, 18028-18033 (2005).

102. Frost,G.I., Csoka,T.B., Wong,T., & Stern,R. Purification, cloning, and expression of human plasma hyaluronidase. *Biochem. Biophys. Res. Commun.* **236**, 10-15 (1997).

103. Chao,K.L., Muthukumar,L., & Herzberg,O. Structure of human hyaluronidase-1, a hyaluronan hydrolyzing enzyme involved in tumor growth and angiogenesis. *Biochem.* **46**, 6911-6920 (2007).

104. Markovic-Housley,Z. *et al.* Crystal structure of hyaluronidase, a major allergen of bee venom. *Structure* **8**, 1025-1035 (2000).

105. Mullegger,J. & Lepperdinger,G. Degradation of hyaluronan by a Hyal2-type hyaluronidase affects pattern formation of vitelline vessels during embryogenesis of Xenopus laevis. *Mech. Dev.* **111**, 25-35 (2002).

106. Lepperdinger,G., Strobl,B., & Kreil,G. *HYAL2*, a human gene expressed in many cells, encodes a lysosomal hyaluronidase with a novel type of specificity. *J. Biol. Chem* **273**, 22466-22470 (1998).

107. Rai,S.K. *et al.* Candidate tumor suppressor HYAL2 is a glycosylphosphatidylinositol (GPI)-anchored cell-surface receptor for jaagsiekte sheep retrovirus, the envelope protein of which mediates oncogenic transformation. *Proc. Natl. Acad. Sci. U. S. A* **98**, 4443-4448 (2001).

108. Bourguignon,L.Y., Singleton,P.A., Diedrich,F., Stern,R., & Gilad,E. CD44 Interaction with Na+-H+ Exchanger (NHE1) Creates Acidic Microenvironments Leading to Hyaluronidase-2 and Cathepsin B Activation and Breast Tumor Cell Invasion. *J. Biol. Chem.* **279**, 26991-27007 (2004).

109. Harada,H. & Takahashi,M. CD44-dependent intracellular and extracellular catabolism of hyaluronic acid by hyaluronidase-1 and -2. *J. Biol. Chem.* **282**, 5597-5607 (2007).

110. Csoka,A.B., Scherer,S.W., & Stern,R. Expression analysis of six paralogous human hyaluronidase genes clustered on chromosomes 3p21 and 7q31. *Genomics* **60**, 356-361 (1999).

111. Lokeshwar,V.B., Schroeder,G.L., Carey,R.I., Soloway,M.S., & Iida,N. Regulation of hyaluronidase activity by alternative mRNA splicing. *J. Biol. Chem.* **277**, 33654-33663 (2002).

112. Hemming,R. *et al.* Mouse Hyal3 encodes a 45-56 kDa glycoprotein whose overexpression increases hyaluronidase 1 activity in cultured cells. *Glycobiology,* in press. (2008).

113. Primakoff,P., Lathrop,W.F., Woolman,L., Cowan,A., & Myles,D. Fully effective contraception in male and female guinea pigs immunized with the sperm protein PH-20. *Nature* **335**, 543-546 (1988).

114. Cherr,G.N. *et al.* The PH-20 protein in cynomologus macaque spermatozoa: identification of two different forms exhibiting hyaluronidase activity. *Dev. Biol.* **175**, 142-153 (1996).

115. Thaler,C.D. & Cardullo,R.A. Biochemical characterization of a glycoslphosphatidylinositol-linked hyaluronidase on mouse sperm. *Biochem.* **34**, 7788-7795 (1995).

116. Cherr,G.N., Yudin,A.I., & Overstreet,J.W. The dual functions of GPI-anchored PH-20: hyaluronidase and intracellular signaling. *Matrix Biol.* **20**, 515-525 (2001).

117. Baba D *et al.* Mouse sperm lacking cell surface hyaluronidase PH-20 can pass through the layer of cumulus cells and fertilize the egg. *Journal of Biological Chemistry* **277**, 30310-30314 (2002).

118. Reitinger,S., Laschober,G.T., Fehrer,C., Greiderer,B., & Lepperdinger,G. Mouse testicular hyaluronidase-like proteins SPAM1 and HYAL5 but not HYALP1 degrade hyaluronan. *Biochem. J.* **401**, 79-85 (2007).

119. Csoka,A.B., Frost,G.I., & Stern,R. The six hyaluronidase-like genes in the human and mouse genomes. *Matrix Biol.* **20**, 499-508 (2001).

120. Miller,K.A., Shao,M., & Martin-DeLeon,P.A. Hyalp1 in murine sperm function: evidence for unique and overlapping functions with other reproductive hyaluronidases. *J. Androl* **28**, 67-76 (2007).

121. Sango,K. *et al.* Mice lacking both subunits of lysosomal beta-hexosaminidase display gangliosidosis and mucopolysaccharidosis. *Nat. Genet.* **14**, 348-352 (1996).

122. Suzuki,K., Sango,K., Proia,R.L., & Langaman,C. Mice deficient in all forms of lysosomal beta-hexosaminidase show mucopolysaccharidosis-like pathology. *J. Neuropathol. Exp. Neurol.* **56**, 693-703 (1997).

123. Vogler,C. *et al.* A murine model of mucopolysaccharidosis VII. Gross and microscopic findings in beta-glucuronidase-deficient mice. *Am. J. Pathol.* **136**, 207-217 (1990).

124. Longas,M.O. & Meyer,K. Sequential hydrolysis of hyaluronate by beta-glucuronidase and beta-N-acetylhexosaminidase. *Biochem. J.* **197**, 275-282 (1981).

125. Franzmann,E.J. *et al.* Expression of tumor markers hyaluronic acid and hyaluronidase (HYAL1) in head and neck tumors. *Int. J. Cancer* **106**, 438-445 (2003).

126. Lokeshwar,V.B. *et al.* Identification of bladder tumor-derived hyaluronidase: its similarity to HYAL1. *Cancer Res* **59**, 4464-4470 (1999).

127. Lokeshwar,V.B. *et al.* Stromal and epithelial expression of tumor markers hyaluronic acid and HYAL1 hyaluronidase in prostate cancer. *J. Biol. Chem.* **276**, 11922-11932 (2001).

128. Pham,H.T., Block,N.L., & Lokeshwar,V.B. Tumor-derived hyaluronidase: a diagnostic urine marker for high-grade bladder cancer. *Cancer Res.* **57**, 778-783 (1997).

129. Lokeshwar,V.B. & Block,N.L. HA-HAase urine test. A sensitive and specific method for detecting bladder cancer and evaluating its grade. *Urol. Clin. North Am.* **27**, 53-61 (2000).

130. Kovar,J.L., Johnson,M.A., Volcheck,W.M., Chen,J., & Simpson,M.A. Hyaluronidase expression induces prostate tumor metastasis in an orthotopic mouse model. *Am. J. Pathol.* **169**, 1415-1426 (2006).

131. Lokeshwar,V.B., Cerwinka,W.H., & Lokeshwar,B.L. HYAL1 hyaluronidase: a molecular determinant of bladder tumor growth and invasion. *Cancer Res.* **65**, 2243-2250 (2005).

132. Simpson,M.A. Concurrent expression of hyaluronan biosynthetic and processing enzymes promotes growth and vascularization of prostate tumors in mice. *Am. J. Pathol.* **169**, 247-257 (2006).

133. Bharadwaj,A.G., Rector,K., & Simpson,M.A. Inducible hyaluronan production reveals differential effects on prostate tumor cell growth and tumor angiogenesis. *J. Biol. Chem.* **282**, 20561-20572 (2007).

134. Lokeshwar,V.B., Cerwinka,W.H., Isoyama,T., & Lokeshwar,B.L. HYAL1 hyaluronidase in prostate cancer: a tumor promoter and suppressor. *Cancer Res.* **65**, 7782-7789 (2005).

135. Itano,N. *et al.* Selective expression and functional characteristics of three mammalian hyaluronan synthases in oncogenic malignant transformation. *J. Biol. Chem.* **279**, 18679-18687 (2004).

136. Russell,C. *et al.* Murine MPS I: insights into the pathogenesis of Hurler syndrome. *Clin. Genet.* **53**, 349-361 (1998).

137. Simonaro,C.M., Haskins,M.E., & Schuchman,E.H. Articular chondrocytes from animals with a dermatan sulfate storage disease undergo a high rate of apoptosis and release nitric oxide and inflammatory cytokines: a possible mechanism underlying degenerative joint disease in the mucopolysaccharidoses. *Lab Invest* **81**, 1319-1328 (2001).

138. Settembre,C. *et al.* A block of autophagy in lysosomal storage disorders. *Hum. Mol. Genet.* **17**, 119-129 (2008).

139. Lee,W.C. *et al.* Enzyme replacement therapy results in substantial improvements in early clinical phenotype in a mouse model of globoid cell leukodystrophy. *FASEB J.* **19**, 1549-1551 (2005).

140. Roces,D.P. *et al.* Efficacy of enzyme replacement therapy in alpha-mannosidosis mice: a preclinical animal study. *Hum. Mol. Genet.* **13**, 1979-1988 (2004).

141. Cachon-Gonzalez,M.B. *et al.* Effective gene therapy in an authentic model of Tay-Sachs-related diseases. *Proc. Natl. Acad. Sci. U. S. A* **103**, 10373-10378 (2006).

142. Enquist,I.B. *et al.* Effective cell and gene therapy in a murine model of Gaucher disease. *Proc. Natl. Acad. Sci. U. S. A* **103**, 13819-13824 (2006).

143. Roberts,A.L., Rees,M.H., Klebe,S., Fletcher,J.M., & Byers,S. Improvement in behaviour after substrate deprivation therapy with rhodamine B in a mouse model of MPS IIIA. *Mol. Genet. Metab* **92**, 115-121 (2007).

144. Nagy,A., Gertsenstein,M., Vintersten,K., & Behringer,R. *Manipulating the Mouse Embryo*(Cold Spring Harbor Laboratory Press, New York, 2003).

145. Nagy,A., Rossant,J., Nagy,R., bramow-Newerly,W., & Roder,J.C. Derivation of completely cell culture-derived mice from early-passage embryonic stem cells. *Proc. Natl. Acad. Sci. U. S. A* **90**, 8424-8428 (1993).

146. Birnboim,H.C. & Doly,J. A rapid alkaline extraction procedure for screening recombinant plasmid DNA. *Nucl. Acids. Res.* **7**, 1513-1517 (1979).

147. Birnboim,H.C. A rapid alkaline extraction method for the isolation of plasmid DNA. *Meth. Enzymol.* **100**, 243-255 (1983).

148. Doetschman,T.C., Eistetter,H., Katz,M., Schmidt,W., & Kemler,R. The in vitro development of blastocyst-derived embryonic stem cell lines: formation of visceral yolk sac, blood islands and myocardium. *J. Embryol. Exp. Morphol.* **87**, 27-45 (1985).

149. Ramirez-Solis,R. *et al.* Genomic DNA microextraction: a method to screen numerous samples. *Anal. Biochem.* **201**, 331-335 (1992).

150. Bradford,M.M. A rapid and sensitive method for the quantitation of microgram quantities of protein utilizing the principle of protein-dye binding. *Anal. Biochem.* **72**, 248-254 (1976).

151. Towbin,H., Staehelin,T., & Gordon,J. Electrophoretic transfer of proteins from polyacrylamide gels to nitrocellulose sheets: procedure and some applications. *Proc. Natl. Acad. Sci. USA* **76**, 4350-4354 (1979).

152. Chomczynski,P. & Mackey,K. One-hour downward capillary blotting of RNA at neutral pH. *Anal. Biochem.* **221**, 303-305 (1994).

153. Livak,K.J. & Schmittgen,T.D. Analysis of relative gene expression data using real-time quantitative PCR and the 2(-Delta Delta C(T)) Method. *Methods* **25**, 402-408 (2001).

154. Pfaffl,M.W., Horgan,G.W., & Dempfle,L. Relative expression software tool (REST) for group-wise comparison and statistical analysis of relative expression results in real-time PCR. *Nucleic Acids Res.* **30**, e36 (2002).

155. Blumenkrantz,N. & Asboe-Hansen,G. New method for quantitative determination of uronic acids. *Anal. Biochem.* **54**, 484-489 (1973).

156. Plaas,A.H., West,L., Midura,R.J., & Hascall,V.C. Disaccharide composition of hyaluronan and chondroitin/dermatan sulfate. Analysis with fluorophore-assisted carbohydrate electrophoresis. *Methods Mol. Biol.* **171**, 117-128 (2001).

157. Karousou,E.G., Porta,G., De,L.G., & Passi,A. Analysis of fluorophore-labelled hyaluronan and chondroitin sulfate disaccharides in biological samples. *J. Pharm. Biomed. Anal.* **34**, 791-795 (2004).

158. Muenzer,J. *et al.* Enzyme replacement therapy in mucopolysaccharidosis type II (Hunter syndrome): a preliminary report. *Acta Paediatr. Suppl* **91**, 98-99 (2002).

159. Cressant,A. *et al.* Improved behavior and neuropathology in the mouse model of Sanfilippo type IIIB disease after adeno-associated virus-mediated gene transfer in the striatum. *J. Neurosci.* **24**, 10229-10239 (2004).

160. Garcia,A.R., DaCosta,J.M., Pan,J., Muenzer,J., & Lamsa,J.C. Preclinical dose ranging studies for enzyme replacement therapy with idursulfase in a knock-out mouse model of MPS II. *Mol. Genet. Metab* **91**, 183-190 (2007).

161. Martin,G.R. Isolation of a pluripotent cell line from early mouse embryos cultured in medium conditioned by teratocarcinoma stem cells. *Proc. Natl. Acad. Sci. U. S. A* **78**, 7634-7638 (1981).

162. Evans,M.J. & Kaufman,M.H. Establishment in culture of pluripotential cells from mouse embryos. *Nature* **292**, 154-156 (1981).

163. Hasty,P., Abuin,A., & Bradley,A. *Gene Targeting*(Oxford University Press Inc., New York, 2000).

164. Thomas,K.R., Folger,K.R., & Capecchi,M.R. High frequency targeting of genes to specific sites in the mammalian genome. *Cell* **44**, 419-428 (1986).

165. Hasty,P., Rivera-Perez,J., Chang,C., & Bradley,A. Target frequency and integration pattern for insertion and replacement vectors in embryonic stem cells. *Mol. Cell Biol.* **11**, 4509-4517 (1991).

166. Gondo,Y. *et al.* Gene replacement of the p53 gene with the lacZ gene in mouse embryonic stem cells and mice by using two steps of homologous recombination. *Biochem. Biophys. Res. Commun.* **202**, 830-837 (1994).

167. Hanks,M., Wurst,W., Anson-Cartwright,L., Auerbach,A.B., & Joyner,A.L. Rescue of the En-1 mutant phenotype by replacement of En-1 with En-2. *Science* **269**, 679-682 (1995).

168. Friedrich,G. & Soriano,P. Promoter traps in embryonic stem cells: a genetic screen to identify and mutate developmental genes in mice. *Genes Dev.* **5**, 1513-1523 (1991).

169. Higuchi,R., Krummel,B., & Saiki,R.K. A general method of in vitro preparation and specific mutagenesis of DNA fragments: study of protein and DNA interactions. *Nucleic Acids Res.* **16**, 7351-7367 (1988).

170. Lefebvre,L., Dionne,N., Karaskova,J., Squire,J.A., & Nagy,A. Selection for transgene homozygosity in embryonic stem cells results in extensive loss of heterozygosity. *Nat. Genet.* **27**, 257-258 (2001).

171. Gardner,R.L. Mouse chimeras obtained by the injection of cells into the blastocyst. *Nature* **220**, 596-597 (1968).

172. Olson,E.N., Arnold,H.H., Rigby,P.W., & Wold,B.J. Know your neighbors: three phenotypes in null mutants of the myogenic bHLH gene MRF4. *Cell* **85**, 1-4 (1996).

173. Braun,T. & Arnold,H.H. Inactivation of Myf-6 and Myf-5 genes in mice leads to alterations in skeletal muscle development. *EMBO J.* **14**, 1176-1186 (1995).

174. Floss,T., Arnold,H.H., & Braun,T. Myf-5(m1)/Myf-6(m1) compound heterozygous mouse mutants down-regulate Myf-5 expression and exert rib defects: evidence for long-range cis effects on Myf-5 transcription. *Dev. Biol.* **174**, 140-147 (1996).

175. Fiering,S., Kim,C.G., Epner,E.M., & Groudine,M. An "in-out" strategy using gene targeting and FLP recombinase for the functional dissection of complex DNA regulatory elements: analysis of the beta-globin locus control region. *Proc. Natl. Acad. Sci. U. S. A* **90**, 8469-8473 (1993).

176. Dorin,J.R. *et al.* Long-term survival of the exon 10 insertional cystic fibrosis mutant mouse is a consequence of low level residual wild-type Cftr gene expression. *Mamm. Genome* **5**, 465-472 (1994).

177. O'Neal,W.K. *et al.* A severe phenotype in mice with a duplication of exon 3 in the cystic fibrosis locus. *Hum. Mol. Genet.* **2**, 1561-1569 (1993).

178. Ratcliff,R. *et al.* Production of a severe cystic fibrosis mutation in mice by gene targeting. *Nat. Genet.* **4**, 35-41 (1993).

179. Scott,H.S. *et al.* Identification of mutations in the alpha-L-iduronidase gene (IDUA) that cause Hurler and Scheie syndromes. *Am. J. Hum. Genet.* **53**, 973-986 (1993).

180. Guo,J. *et al.* Multicolor karyotype analyses of mouse embryonic stem cells. *In Vitro Cell Dev. Biol. Anim* **41**, 278-283 (2005).

181. Dean,W. *et al.* Altered imprinted gene methylation and expression in completely ES cell-derived mouse fetuses: association with aberrant phenotypes. *Dev.* **125**, 2273-2282 (1998).

182. Clarke,K.A. & Still,J. Gait analysis in the mouse. *Physiol Behav.* **66**, 723-729 (1999).

183. Dieppe,P.A. & Lohmander,L.S. Pathogenesis and management of pain in osteoarthritis. *Lancet* **365**, 965-973 (2005).

184. Aigner,T. & McKenna,L. Molecular pathology and pathobiology of osteoarthritic cartilage. *Cell Mol. Life Sci.* **59**, 5-18 (2002).

185. Haskins,M.E. Animal models for mucopolysaccharidosis disorders and their clinical relevance. *Acta Paediatr. Suppl* **96**, 56-62 (2007).

186. Li,H.H. *et al.* Mouse model of Sanfilippo syndrome type B produced by targeted disruption of the gene encoding alpha-N-acetylglucosaminidase. *Proc. Natl. Acad. Sci. U. S. A* **96**, 14505-14510 (1999).

187. Tomatsu,S. *et al.* Mouse model of N-acetylgalactosamine-6-sulfate sulfatase deficiency (Galns-/-) produced by targeted disruption of the gene defective in Morquio A disease. *Hum. Mol. Genet.* **12**, 3349-3358 (2003).

188. Ohshima,T. *et al.* alpha-Galactosidase A deficient mice: a model of Fabry disease. *Proc. Natl. Acad. Sci. U. S. A* **94**, 2540-2544 (1997).

189. Phaneuf,D. *et al.* Dramatically different phenotypes in mouse models of human Tay-Sachs and Sandhoff diseases. *Hum. Mol. Genet.* **5**, 1-14 (1996).

190. Clarke,L.A. *et al.* Murine mucopolysaccharidosis type I: targeted disruption of the murine alpha-L-iduronidase gene. *Hum. Mol. Genet.* **6**, 503-511 (1997).

191. Garcia,A.R., Pan,J., Lamsa,J.C., & Muenzer,J. The characterization of a murine model of mucopolysaccharidosis II (Hunter syndrome). *J. Inherit. Metab Dis.* **30**, 924-934 (2007).

192. Evers,M. *et al.* Targeted disruption of the arylsulfatase B gene results in mice resembling the phenotype of mucopolysaccharidosis VI. *Proc. Natl. Acad. Sci. U. S. A* **93**, 8214-8219 (1996).

193. Holmes,M.W., Bayliss,M.T., & Muir,H. Hyaluronic acid in human articular cartilage. Age-related changes in content and size. *Biochem. J.* **250**, 435-441 (1988).

194. Brown,T.J., Laurent,U.B., & Fraser,J.R. Turnover of hyaluronan in synovial joints: elimination of labelled hyaluronan from the knee joint of the rabbit. *Exp. Physiol* **76**, 125-134 (1991).

195. Antonas,K.N., Fraser,J.R., & Muirden,K.D. Distribution of biologically labelled radioactive hyaluronic acid injected into joints. *Ann. Rheum. Dis.* **32**, 103-111 (1973).

196. Tanimoto,K. *et al.* Hyaluronidase expression in cultured growth plate chondrocytes during differentiation. *Cell Tissue Res.* **318**, 335-342 (2004).

197. Nicoll,S.B., Barak,O., Csoka,A.B., Bhatnagar,R.S., & Stern,R. Hyaluronidases and CD44 undergo differential modulation during chondrogenesis. *Biochem. Biophys. Res. Commun.* **292**, 819-825 (2002).

198. Flannery,C.R., Little,C.B.H.C.E., & Caterson,B. Expression and activity of articular cartilage hyaluronidases. *Biochem. Biophys. Res. Commun.* **251**, 824-829 (1998).

199. Bastow,E.R. *et al.* Hyaluronan synthesis and degradation in cartilage and bone. *Cell Mol. Life Sci.* **65**, 395-413 (2008).

200. Roberts,G.P. & Harding,K.G. Stimulation of glycosaminoglycan synthesis in cultured fibroblasts by hyperbaric oxygen. *British J. Dermatol.* **131**, 630-633 (1994).

201. Sango,K. *et al.* Mouse models of Tay-Sachs and Sandhoff diseases differ in neurologic phenotype and ganglioside metabolism. *Nat. Genet.* **11**, 170-176 (1995).

202. El,H.H., Cole,A.A., & Manicourt,D.H. Chondrocytes, synoviocytes and dermal fibroblasts all express PH-20, a hyaluronidase active at neutral pH. *Arthritis Res. Ther.* **7**, R756-R768 (2005).

203. Petrella,R.J. & Petrella,M. A prospective, randomized, double-blind, placebo controlled study to evaluate the efficacy of intraarticular hyaluronic acid for osteoarthritis of the knee. *J. Rheumatol.* **33**, 951-956 (2006).

204. Beutler,B. The Toll-like receptors: analysis by forward genetic methods. *Immunogenetics* **57**, 385-392 (2005).

205. Lovvorn,H.N., III, Savani,R.C., Ruchelli,E., Cass,D.L., & Adzick,N.S. Serum hyaluronan and its association with unfavorable histology and aggressiveness of heterotransplanted Wilms' tumor. *J. Pediatr. Surg.* **35**, 1070-1078 (2000).

206. Stoop,R., Kotani,H., McNeish,J.D., Otterness,I.G., & Mikecz,K. Increased resistance to collagen-induced arthritis in CD44-deficient DBA/1 mice. *Arthritis Rheum.* **44**, 2922-2931 (2001).

207. Venn,G. & Mason,R.M. Absence of keratan sulphate from skeletal tissues of mouse and rat. *Biochem. J.* **228**, 443-450 (1985).

Appendix 1

Table 1: Transcript abundance of the hyaluronidase genes in human tissues.

Tissue	*HYAL1*	*HYAL2*	*HYAL3*	*HYAL4*	*SPAM1*	*Hyal5*
Adipose	0	380	76	0	0	0
Adrenal gland	180	150	0	0	0	0
Bone Marrow	0	0	61	0	0	0
Brain	12	34	45	0	3	0
Connective tissue	33	60	13	0	6	0
Heart	143	143	0	0	0	0
Intestine	33	50	8	0	0	0
Kidney	127	89	14	0	0	0
Liver	124	33	4	0	0	0
Lung	47	106	14	0	0	0
Lymph Node	0	141	0	0	0	0
Ovary	19	68	29	0	0	0
Pancreas	37	60	23	0	0	0
P.B. Leukocytes	8	16	24	0	0	0
Placenta	0	137	21	17	0	0
Prostate	20	52	10	0	0	0
Muscle	9	46	18	0	0	0
Spleen	462	332	18	0	0	0
Stomach	61	82	82	0	0	0
Testis	12	15	39	0	45	118
Thymus	24	12	36	0	0	0
Thyroid	0	20	104	0	0	0
Trachea	19	38	0	0	0	0

* The numbers shown are representative of the transcripts detected per million ESTs in the tissues based on the gene expression profiles found in the NCBI database.